Expanding the optogenetic toolkit with a photocleavable protein and a near infrared pH indicator

by

Wei Zhang

A thesis submitted in partial fulfillment of the requirements for the degree of

Doctor of Philosophy

Department of Chemistry

University of Alberta

Abstract

Optogenetics is an emerging biological technique that is causing a revolution in life science. It uses optical methods to control and visualize genetically targeted biological events in a relatively non-invasive and spatiotemporally precise manner. Optogenetics requires advanced optical instruments, but the most important requirement is genetically encodable molecular tools to serve as the interface between light and biology. Naturally occurring photoreceptor proteins are a great source of optogenetic tools, however, their range of utility is restricted. Most naturally occurring photoreceptor proteins have required some degree of protein engineering for improved optical and functional properties. Encouragingly, an expanded range of optogenetic tools with novel functions has been developed by coupling the natural photosensory mechanisms with certain proteins. Through such efforts, the optogenetic toolkit is rapidly growing, though it is still relatively limited.

In this thesis, we describe our efforts to expand the scope of photosensory mechanisms by engineering a photocleavable protein (PhoCl) that splits into two fragments upon violet light (~400 nm) illumination. PhoCl is a circularly permuted version of a green-to-red photoconvertible fluorescent protein (FP) in which the main chain break that accompanies photoconversion produces a short chromophore-containing peptide fragment that spontaneously dissociates from the large fragment. We have used PhoCl to manipulate protein localization and gene expression by genetically inserting it between a protein-of-interest (POI) and a subcellular localization tag. Upon illumination, the POI is released from the subcellular localization tag and is free to diffuse throughout the cell. We have also used PhoCl to "cage" an enzyme of interest by fusing a peptide-based

inhibitor to an enzyme via PhoCl. Light-dependent cleavage of PhoCl leads to release of the inhibitor and activation of the formerly caged enzyme. This strategy has been successfully applied to hepatitis C virus (HCV) protease, which was further used to activate the channel-forming glycoprotein, Pannexin-1.

We also report the development, optimization, and characterization of the first genetically encoded near infrared (NIR) fluorescent pH indicator, pH-mIFP. The pH dependent fluorescence was introduced to the NIR FP by rational design, which was followed by directed evolution for improved brightness and pH sensitivity. We have demonstrated pH-mIFP can report pH changes on the surface of cultured mammalian cells. Fluorescence imaging with long-wavelength excitation light has the advantages of low cytotoxicity, deeper tissues penetration, and spectral compatibility with existing optogenetic tools. Therefore, we expect pH-mIFP will find use for multicolour and deep-tissue fluorescence imaging of physiologically-relevant pH changes.

Preface

A version of chapter 2 of this thesis has been published as Zhang, W.; Lohman, A. W.; Zhuravlova, Y.; Lu, X.; Wiens, M. D.; Hoi, H.; Yaganoglu, S.; Mohr, M. A.; Kitova, E. N.; Klassen, J. S.; Pantazis, P.; Thompson, R. J.; Campbell, R. E. Optogenetic control with a photocleavable protein, PhoCl. *Nat. Methods* **2017**, *14*, 391–394. W.Z. and A.W.L. contributed equally to this work. W.Z., A.W.L., P.P., R.J.T., and R.E.C. conceived and designed experiments. W.Z. assembled all constructs and characterized protein *in vitro*. W.Z. and M.D.W. performed directed evolution. W.Z., X.L., and H.H. performed imaging of protein translocation. W.Z. and Y.Z. performed light-induced gene expression. A.W.L. characterized Opto-Panx1. S.Y., M.A.M., and P.P. performed primed conversion. E.N.K. and J.S.K. performed mass spectrometry analysis. All authors were involved in data analysis, and W.Z., A.W.L., R.J.T., and R.E.C. wrote the manuscript.

Acknowledgements

First, I would like to thank my research supervisor, Dr. Robert E. Campbell, for his support and guidance during my Ph.D. study. Before joining the Campbell lab, I knew nothing about optogenetics. He led me into such an exciting and colourful area that I feel more enthusiastic about it than ever despite all the difficulties and obstacles I met these years. I also express my gratitude to him for his help with the published manuscript and this thesis. The education and inspiration from him are invaluable.

I sincerely thank the professors in my thesis committee: Dr. Mark T. McDermott, Dr. Ratmir Derda, Dr. Christopher W. Cairo, and Dr. Chandra Tucker from the Department of Pharmacology at University of Colorado School of Medicine, to attend my final oral exam, and to provide me reviews and comments on my thesis.

I would also like to thank the other faculty members and staffs in the Department of Chemistry. Special thanks to Gareth Lambkin for technical assistance. The support from collaborators is also highly appreciated. Without their efforts, much of the work described in this thesis would not have been possible.

I highly value the friendship from our group members and other friends in the Department who support me in many aspects. I would also like to thank our senior group members. Because of their contributions to the lab and to my research, I could initiate my project without too much difficulty. I also thank the financial support from Alberta Innovates Technology Futures (AITF). Finally, I thank the support and understanding from my parents during all these years.

Table of Contents

List of Tables

List of Figures

List of Abbreviations

7-TM	seven-transmembrane
aCSF	artificial cerebrospinal fluid
ADP	adenosine diphosphate
AID	autoinhibitory domain
Arch	Archaerhodopsin
AsLOV2	*Avena sativa* phototropin 1 LOV2 domain
AtLOV2	*Arabidopsis thaliana* phototropin 2 LOV2 domain
ATP	adenosine triphosphate
avGFP	*Aequorea Victoria* green fluorescent protein
BiFC	bimolecular fluorescence complementation
BLINK	blue-light induced K^+ channel
BLUF	blue light sensor using flavin adenine dinucleotide
bPAC	bacterium *Beggiatoa* photoactivated adenylyl cyclase
BphP	bacterial phytochrome photoreceptor
BR	bacteriorhodopsin
BRET	bioluminescence resonance energy transfer
BSA	bovine serum albumin
BV	biliverdin
CaM	calmodulin
cAMP	cyclic adenosine monophosphate
Cas9	CRISPR-associated protein 9
CBX	carbenoxolone
CCD	charge-coupled device

cGMP	cyclic guanosine monophosphate
ChR	Channelrhodopsin
CIB1	cryptochrome-interacting basic-helix-loop-helix protein
COP1	constitutive photomorphogenesis 1
cp	circularly permuted (or circular permutation)
cpFP	circularly permutated fluorescent protein
CRAC	Ca^{2+} release-activated Ca^{2+}
CRISPR	clustered regularly interspaced short palindromic repeats
crRNA	CRISPR RNA
CRY2	*Arabidopsis* cryptochrome 2
Da	Dalton
DAG	diacylglycerol
dCas9	nuclease-deficient Cas9
ddFP	dimerization-dependent fluorescent protein
df	degrees-of-freedom
DHFR	dihydrofolate reductase
DMEM	Dulbecco's modified Eagle medium
E. coli	*Escherichia coli*
EDTA	ethylenediaminetetraacetic acid
EGFP	enhanced green fluorescent protein
EGTA	ethylene glycol tetraacetic acid
ESI	electrospray ionization
ESI-MS	electrospray ionization mass spectrometry
euPACα	*Euglena gracilis* photoactivated adenylyl cyclase

FAD	flavin adenine dinucleotide
FBS	fetal bovine serum
FLIP	fluorescent light-inducible protein
FMN	flavin mononucleotide
FP	fluorescent protein
FRAP	fluorescence recovery after photobleaching
FRET	Förster resonance energy transfer
GECO	genetically encoded Ca^{2+} indicator for optical imaging
GEF	guanine exchange factor
GFC	gel filtration chromatography
GFP	green fluorescent protein
GFR	growth factor receptor
G-GECO	green genetically encoded Ca^{2+} indicator for optical imaging
GPCR	G protein-coupled receptor
GTPase	guanosine triphosphatase
Gαq	α subunit of heterotrimeric Gq protein
HCV	hepatitis C virus
HCVp	hepatitis C virus NS3/4A protease
HDR	homology-directed repair
HEK	human embryonic kidney
HR	halorhodopsin
HS	slide helix
Hsp90	heat shock protein 90
HY5	elongated hypocotyl 5

IP3	inositol 1,4,5-trisphosphate
Jα	α-helix
Kcv	viral potassium (K^+) channel
K_d	dissociation constant
kDa	kilodalton
K_i	inhibitory constant
LB	Luria-Bertani
LED	light-emitting diode
LEXY	light-inducible nuclear export system
LINuS	light-inducible nuclear localization signal
LOV	light-oxygen-voltage sensing
LOVTRAP	LOV2 trap and release of protein
MBP	maltose binding protein
mFBphP1	monomeric NIR FP derived from *Rhodopseudomonas palustris* BphP1
miniSOG	mini Singlet Oxygen Generator
MP	multimeric protein domain of CaMKII
MS	mass spectrometry
MT	membrane tethered
MV	molecular weight
NES	nuclear exclusion sequence
n_H	Hill coefficient
NHEJ	non-homologous end joining
NIR	near-infrared

NLS	nuclear localization signal (or sequence)
nMag	negative Magnet
NMR	nuclear magnetic resonance
NpHR	*Natromonas pharaonis* halorhodopsin
Opto-Panx1	optogenetically-activated Pannexin-1
PAC	photoactivated adenylyl cyclase
paCas9	photoactivatable Cas9
PACR	photoactivatable Ca^{2+} releaser
PA-Cre	photoactivatable Cre recombinase
PALM	photoactivated localization microscopy
PAM	protospacer-adjacent motif
$Panx1^{HCV}$	hepatitis C virus NS3/4A protease-activatable Panx1
PA-Rac1	photoactivatable Rac1
PAS	Per-Arnt-Sim
PAT	photoacoustic tomography
PBS	phosphate-buffered saline
pCA	*p*-coumaric acid
PCA	protein-fragment complementation assay
PCB	phycocyanobilin
pcFP	circularly permutated fluorescent protein
PCFP	photoconvertible fluorescent protein
PCR	polymerase chain reaction
PhoCl	photocleavable protein
PhyB	Phytochrome B

PI3K	phosphatidylinositol 3-kinase
PIF	phytochrome interaction factor
PLC	phospholipase C
pMag	positive Magnet
POI	protein-of-interest
PPI	protein-protein interaction
PSB	protonated Schiff base
PYP	photoactive yellow protein
PΦB	phytochromobilin
RCF	relative centrifugal force
RFP	red fluorescent protein
RNAP	RNA polymerase
RNP	RNA/protein
RTK	receptor tyrosine kinase
SDS-PAGE	sodium dodecyl sulfate polyacrylamide gel electrophoresis
SEP	superecliptic pHluorin
sgRNA	single-guide RNA
SR	steroid receptor
$t_{1/2}$	half-life
$T_{1/2}$	half-maximal time value
TALEN	transcription activator-like effector
TBS	Tris-buffered saline
TBST	Tris-buffered saline with 0.05% Tween-20
TEV	tobacco etch virus

tracrRNA	trans-activating CRISPR RNA
TRP	transient receptor potential
TrpR	tryptophan repressor
TULIPs	tunable and light-controlled interacting protein tags
UAS	upstream activator sequence
UV	ultraviolet
UVR8	UV-B resistance 8
VVD	fungal circadian clock photoreceptor Vivid
β2-AR	β2-adrenergic receptor
ε	extinction coefficient
λ_{emi}	emission maxima
λ_{exi}	excitation maxima
Φ	quantum yield

Chapter 1: Introduction

1.1 Overview and premise

Optogenetic techniques have been widespread throughout the life-science community since they first rose to prominence about one decade ago. These techniques combine optical and genetic strategies to control and visualize defined biological processes [1–3]. Compared with conventional chemical and electrophysiological techniques, optical methods are relatively non-invasive and provide high spatiotemporal resolution. Furthermore, genetic modification, though being time-consuming, enables precise targeting of biological events at molecular level. The combination of optical and genetic methods, for the first time in history, allows us to interrogate specific biological processes under close to native conditions.

The key reagents required for optogenetics are proteins that are both light excitable and genetically encodable. Most organisms on earth use light, in one way or another, to favor their survival. Natural photoreceptor proteins serve as the light transducers that mediate either energy transfer (photosynthesis) or signal transfer through processes that include visual perception, photoperiodism, phototropism, and phototaxis [4]. The well-known photoreceptor proteins include opsins, phototropins, cryptochromes, ultraviolet (UV) -B receptor, green fluorescent protein (GFP) (and its homologs), and phytochromes.

Originally, the term “optogenetics” only referred to the optical control of electrical activity in neurons with microbial opsins expressed heterologously [1]. The repertoire of optogenetics has since been expanded with the development and use of optogenetic tools that enable control and imaging of a variety of

biological activities. Most optogenetic tools are generated from natural photoreceptor proteins through the process of protein engineering [3,5–7]. According to their different responses upon the absorption of light, the tools are subdivided into two groups: **optogenetic actuators** to transduce light into biological stimuli (control), and **optogenetic indicators** to transduce light into readouts (imaging). Moreover, the combined use of both indicators and actuators enables all-optical assays in which a biological activity is being simultaneously visualized and controlled [8–10].

An optogenetic tool typically consists of a photosensory moiety that interacts with light and a second moiety that interacts with the biological system. For actuators, the photosensory moiety absorbs light and initiates protein conformational changes through photoreactions such as photoisomerization and photoreduction. As a result, the activity of its interactive moiety is modified. For indicators, the photosensory moiety absorbs light and emits energy as photons (exhibits fluorescence). Its interactive moiety reacts with small biomolecules or other biochemical changes and alters the fluorescence intensity or profile.

The photosensory moiety must contain a chromophore to enable light absorption. The common chromophores include endogenous small molecules, like retinals in opsins, flavins in cryptochromes and phototropins, and bilins in phytochromes. GFP is unique in that its chromophore is generated from autogenically modified amino acid residues that are part of its own sequence. The chemical characters of a chromophore and the microenvironment around it determine the optical properties of an optogenetic tool, such as absorbance wavelength, extinction coefficient (ability to absorb light), quantum yield

(ability to convert absorbed photons into fluorescence or photoreactions), and kinetics of the photocycle. The optical properties often can be optimized using the strategies of protein engineering including rational design and directed evolution [6,7,11–13].

In order to interact with the biological system, the photosensory moiety is coupled with an interacting moiety in one optogenetic tool. Based on the different modes of incorporation, optogenetic tools can be categorized into two types (**Figure 1.1**). For type I tools, the two moieties both originated from one family of natural photoreceptor proteins, and are naturally incorporated. These tools, like Channelrhodopsin (ChR) -2 (a light-gated ion channel) [14] and pHluorin (a pH-sensitive GFP) [15], inherit the functions from their protein progenitors. For type II tools, the interacting moiety (e.g., a functional motif from a protein-of-interest (POI)) has been genetically fused with a photosensory domain. For example, photoactivatable Rac1 (PA-Rac1), is composed of the photoreactive light-oxygen-voltage sensing (LOV) domain from phototropin fused to a small GTPase (guanosine triphosphatase), Rac 1 [16]. Similarly, genetically encoded Ca^{2+} indicators for optical imaging (GECOs) are composed of a calcium sensing domain (a vertebrate calmodulin (CaM) and the CaM-binding region of chicken myosin light chain kinase (M13)) fused to a circularly permuted (cp) fluorescent protein (FP) [17]. This general type II strategy holds the promises of practically unlimited possibilities in terms of the scope of biological processes that can be optogenetically controlled and imaged, as the interactive moiety could be derived from any POI in principle. However, in practice, the arsenal of optogenetic tools remains relatively limited.

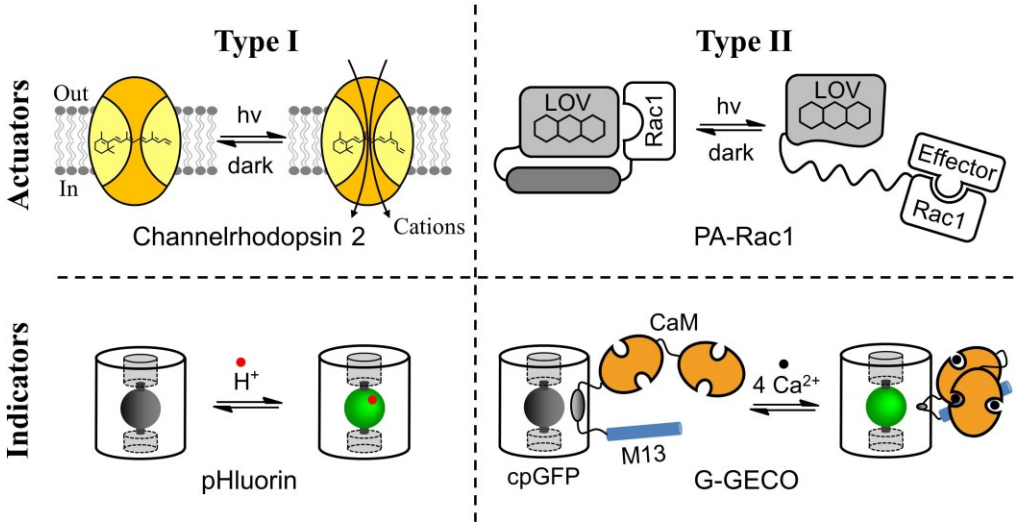

Figure 1.1. Schematic representations of optogenetic tools. The examples shown are: ChR-2 for type I actuators; pHluorin for type I indicators; PA-Rac1 for type II actuators; and green GECO (G-GECO) for type II indicators. The type II optogenetic tools are typically a hybrid of a photosensory domain and the functional motifs from a POI.

Now, optogenetics is no longer considered quite revolutionary as it once was, as its concept and advantages have already been widely recognized and exploited by biologists. However, as more biologists have grown accustomed to using optogenetic tools, there is a growing demand for tools with new capabilities [18,19]. However, the range of optogenetic tools remains disappointingly small, primarily due to the limited capabilities of natural photosensory domains. For the research described in this thesis, we attempted to address the limitation by using protein engineering to generate new optogenetic tools. One set of tools are optogenetic actuators that were enabled by a photocleavable protein (PhoCl) derived from a green-to-red photoconvertible FP. Another type of tool is an optogenetic fluorescent pH indicator based on a near-infrared (NIR) FP derived from bacterial phytochrome. In this introductory chapter, we present an overview covering the strategies of

tool development using natural photosensory domains. Topics to be reviewed include: opsins, photosensitive flavoproteins, UV-B receptor, photoactive yellow proteins (PYPs), GFP-like proteins, and phytochromes.

1.2 Opsins

Opsins are a group of photosensitive proteins found in a broad range of species including animals and microbes. Their most familiar function is as photoreceptors required for vision [20]. Opsins contain a seven-transmembrane (7-TM) domain that binds to a retinal chromophore covalently through a protonated Schiff base (PSB) linkage with the side chain amine of a conserved lysine residue [21,22]. Upon light absorption the retinal isomerizes and thereby triggers conformational changes that initiate diverse subsequent events, such as signal transductions [20].

Though they share high structural similarity, animal and microbial opsins differ in two fundamental respects: photocycle and function [23,24]. First, animal opsins utilize the 11-*cis* isomer of retinal (or derivatives), which isomerizes to the all-*trans* configuration when illuminated. For the next round of photocycle, the opsin must be regenerated through recruitment of a new 11-*cis* retinal (in vertebrates) [25], or direct re-isomerization induced by absorption of photon with longer wavelength (in invertebrates) [26]. In vertebrates, the released all-*trans* chromophore will eventually revert to the 11-*cis* configuration through a time-consuming (~30 min) enzymatic pathway in retina [25]. Microbial opsins, in contrast, use all-*trans* retinal, which isomerizes to the 13-*cis* configuration upon illumination and spontaneously reverts to the ground state in the dark on a timescale of milliseconds, while remaining conjugated

with the protein as a PSB (**Figure 1.2a**) [27]. Second, animal opsins, belonging to the family of G protein-coupled receptors (GPCRs), modulate internal signal transduction pathways through the interaction with the cognate G proteins [23]. In contrast, microbial opsins are typically light-activated ion pumps or channels that directly generate ion currents across the cellular membrane [24]. Both groups of opsins have been extensively characterized, engineered and expressed heterologously to control and image cell activities optogenetically by researchers, primarily neuroscientists [23,28].

1.2.1 Animal opsins

In 2002, Zemelman and Miesenböck reported the concept of optogenetic control: selective photostimulation of genetically designated cells [29]. However, the popular term "optogenetics" was first mentioned in the literature by Deisseroth in 2006 [1]. Zemelman and Miesenböck demonstrated the concept by expressing a combination of proteins, called "ChARGe", which included the *Drosophila* NinaE opsin, arrestin-2, and the cognate G protein α subunit, in cultured mammalian neurons. White light was used to induce action potentials in the neurons expressing ChARGe. White light was used because, in addition to the higher energy blue light required for photoactivation, NinaE requires lower energy photons to regenerate the ground-state chromophore with the assistance of arrestin-2. However, this approach was hindered from widespread application due to its poor temporal accuracy. The neuron firings induced by ChARGe were not tightly temporally coupled to the light stimuli due to the lengthy multi-junction signalling pathway downstream of opsin activation. Specifically, neuron firing involves the activation of G protein α subunit, phospholipase C (PLC), and possibly a biochemical cascade to open

endogenous transient receptor potential (TRP) cation channels [26,30].

Although animal opsins do not provide an ideal temporal resolution for the control of neuronal electrical activity, they are particularly well suited to induce G protein related biochemical events optically. For example, in 2005 Kim et al. engineered a chimeric opsin to activate β2-adrenergic receptor (β2-AR) - mediated signaling optically, by replacing the intracellular loops of bovine opsin with those of β2-AR that form the interface between β2-AR and its cognate G protein [31]. This work inspired the development of an expanding family of synthetic opsins that combine optical control with the function of chemical sensing GPCRs including adrenergic receptors [32], serotonin (5-HT) receptors [33,34] and μ-opioid receptor [35]. In all these experiments, exogenous 11-*cis* retinal must be supplied when vertebrate opsins were used, due to the lack of enzymatic pathway for chromophore regeneration outside of the retina [25].

1.2.2 Microbial opsins

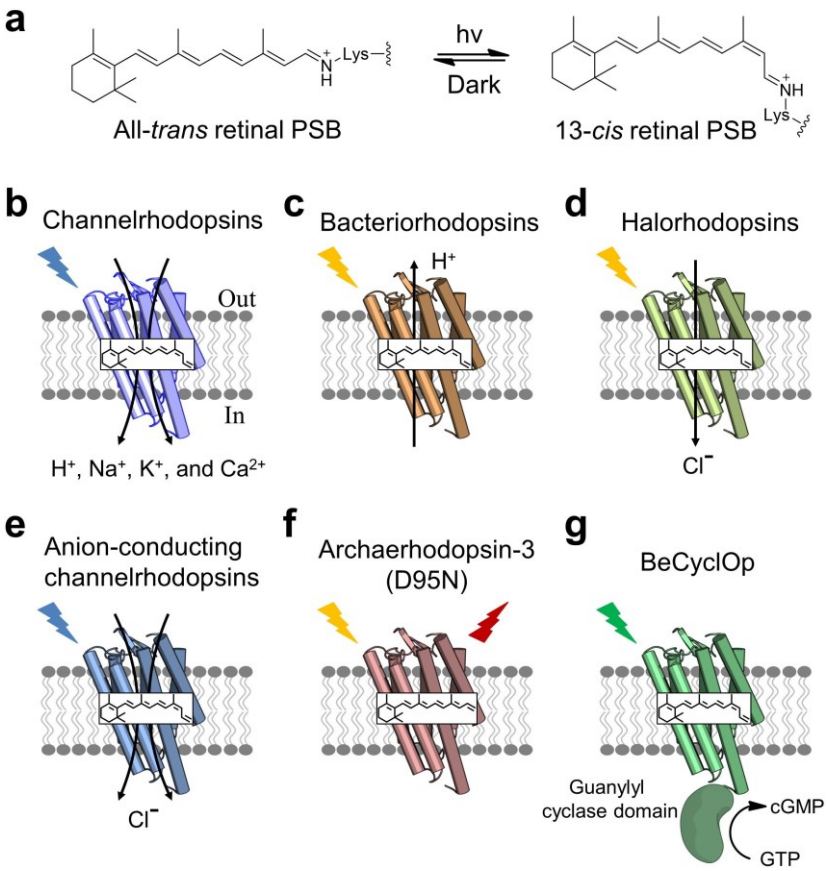

Figure 1.2. Microbial opsins. (**a**) Light-induced isomerization of the retinal chromophore in microbial opsins. (**b-g**) Schematic representations of microbial opsin-based optogenetic tools including ChRs (**b**), bacteriorhodopsins (**c**), halorhodopsins (**d**), anion-conducting ChRs (**e**), Arch-3-based voltage indicators (**f**), and a fungal opsin-based guanylyl cyclase BeCycOp (**g**). The three-dimensional structures are rendered based on 7-TM domain of a C1C2 chimaera between ChR-1 and ChR-2 (PDB ID 3UG9 [36]).

In 2005, Boyden et al. first demonstrated the power of microbial opsins to control neuronal electrical activity by using the 7-TM fragment of Channelrhodopsin (ChR) -2 which is a light-gated cation channel from a green unicellular alga [14]. When expressed in mammalian neurons, ChR-2 inserts into the plasma membrane and induces cation (H^+, Na^+, K^+, and Ca^{2+}) influx in response to blue light (**Figure 1.2b**) [37]. It shows no dark current, and exhibits rapid on and off kinetics with time constants of ~1 and ~10 ms, respectively.

On account of its robust expression and high photosensitivity, ChR-2 allows the membrane potential to reach the threshold for depolarization within 5–15 milliseconds of illumination at a modest light intensity (~10 mW/mm^2). Accordingly, ChR-2 can be used to drive neuronal firing at physiologically relevant frequencies without too much concern for phototoxicity. Additionally, ChR-2 can be easily delivered, as it is encoded in a modestly-sized single gene of ~900 base pairs (bps) and is self-sufficient to incorporate the endogenous all-*trans* retinal efficiently in mammalian tissues. Because of these features, ChR-2 enables precise control of action potential firing in many types of preparations including freely behaving mammals [38,39], and has been applied widely in life-science laboratories. In addition to ChR-2, a variety of channelrhodopsin variants have been discovered from other species or designed using protein engineering for one or multiple desired characters, such as tuned kinetics [40–42], increased photocurrent [43–45], red-shifted excitation wavelength [42,46–48], improved protein expression [44,45], and ion selectivity [49].

While channelrhodopsins are indeed a channel that passes ions down the concentration gradient, the bacteriorhodopsins (BRs) and halorhodopsins (HRs), were identified as light-driven ion pumps [50,51]. BRs can transport one H^+ out the cell each photocycle and HRs pump Cl^- into the cell (**Figure 1.2c,d**). Both of these microbial opsins can, in principle, be used to generate outward photo-currents and cause neuronal inhibition (hyperpolarization) by increasing the threshold of stimulus required to initiate action potentials. In 2007, Zhang et al. reported that *Natromonas pharaonis* halorhodopsin (NpHR) could be used to hyperpolarize neurons in free-behaving animals on timescales ranging from milliseconds to minutes in response to yellow-light illumination [52]. Since then,

various BRs, HRs, and their derivatives have been exploited to induce neuronal inhibition [53]. However none of these opsins has yet proven to be the optimal tool to silence neurons optogenetically, mainly due to their limited photocurrents compared with ChR-2. Activation of ChR-2 leads to opening of a pore (≥ 6 Å) that allows many ions to flow through [37]. In 2014, two groups of scientists, Wietek et al. and Berndt et al., simultaneously reported the conversion of channelrhodopsins into light-gated chloride channels by introducing point mutations to remove negative charges and add positive charges in the channel pore (**Figure 1.2e**) [54,55]. Upon illumination, these anion-conducting channels can inhibit action potentials by creating counter photocurrents only when stimulus occurs. Recently, naturally occurring chloride conducting channels have been identified and applied as optogenetic tools [56–58]. Given their capability to drive specific ions against electrochemical gradients, ion-conducting pumps are the only optogenetic tool option for transporting ions against the concentration gradient. For example, a BR-type proton pump called Archaerhodopsin (Arch) -3 was targeted to synaptic vesicles and lysosomes to induce their light-dependent acidification [59].

In 2011, Kralj et al. first described the potential of using microbial opsins to image voltage transients in neurons [60]. The authors discovered that Arch-3 exhibited voltage-dependent fluorescence changes (excitation maximum (λ_{exi}) at 560 nm and emission maximum (λ_{emi}) at 690 nm), in addition to its long-known function as an outward proton pump. By mutating one key residue required for proton transfer, they generated Arch (D95N) a fluorescent opsin-based voltage indicator (**Figure 1.2f**). However, the utility of Arch (D95N) was

limited due to its relatively low fluorescent brightness (15 $M^{-1}cm^{-1}$, calculated by extinction coefficient × quantum yield) and slow response (off-time constant, 41 ms). Hochbaum, Zhao and colleagues used directed evolution to improve the photophysical characteristics of Arch (D95N), leading to two variants named QuasAr1 and QuasAr2, which showed increased brightness and voltage sensitivity, and responded to membrane potential changes on sub-millisecond timescale [61]. They combined the QuasAr reporters with a blue-shifted channelrhodopsin (λ_{exi} at 460 nm) to enable all-optical control and detection of membrane voltage with minimal cross-talk. The combination was named 'Optopatch', because of its functional similarity with patch clamp electrophysiological techniques.

With the ongoing discovery of additional microbial opsins with functions other than ion transfer, the opsin-based optogenetic toolkit is expanding. For example, a microbial opsin with a guanylyl-cyclase intracellular domain, named as BeCyclOp, was recently identified in the fungus *Blastocladiella emersonii* [62]. BeCyclOp was demonstrated to be useful as a light-regulated guanylyl cyclase to trigger cyclic guanosine monophosphate (cGMP) increase in a variety cell types and in a freely behaving animal, *Caenorhabditis elegans* (**Figure 1.2g**) [63]. Over one decade since they were first reported, microbial opsins are arguably the single most useful class of optogenetic actuator because of their robust expression, high specificity, fast kinetics and great sensitivity. However, their functions as tools are generally limited to the functionality of their natural progenitors, which only represent a small corner of biology. More general photosensory modules are needed for future tool development in optogenetics.

1.3 Photosensitive flavoproteins

Flavoproteins are a family of proteins containing either flavin adenine dinucleotide (FAD) or flavin mononucleotide (FMN) as a redox cofactor, and mediate a wide array of biological processes that involve reduction–oxidation reactions [64]. Some examples of photosensitive flavoproteins include: phototropins involved in the phototropism of plants; cryptochromes involved in the circadian rhythms of plants and animals; and transcriptional antirepressor AppA involved in the regulation of bacterial photosynthesis [65,66]. These photosensitive flavoproteins react with light through photoreduction of the flavin chromophore in their photosensory domains [67]. Some of the photosensory domains, such as light-oxygen-voltage sensing (LOV) domains in phototropins and cryptochromes, have been widely used to engineer optogenetic tools for biological processes that are unrelated to the natural roles of these proteins.

1.3.1 LOV domains

LOV domains were first identified as the photosensory domains in *Arabidopsis* phototropin 1 [68]. However, they were subsequently found in a variety of bacterial, fungal, algal, and higher plant species [69]. Structurally, LOV domains are small (~15 kilodalton (kDa)) and are considered a subset of the Per-Arnt-Sim (PAS) domain family. Proteins in this family have a helical face and a 5-stranded antiparallel β-sheet that form a binding pocket for the FMN or FAD chromophore [70]. In the dark-state, a LOV domain contains an oxidized flavin chromophore that absorbs blue light (wavelength, ~400–480 nm). Upon illumination, the flavin chromophore is reduced through formation of a thioether bond between its C4a position and the thiol moiety of the active

site cysteine residue (**Figure 1.3**) [71]. This formation of a new covalent bond leads to conformational changes in the highly variable N- or C-terminal regions [72]. This process is thermally reversible on a timescale of seconds to days in the dark [73].

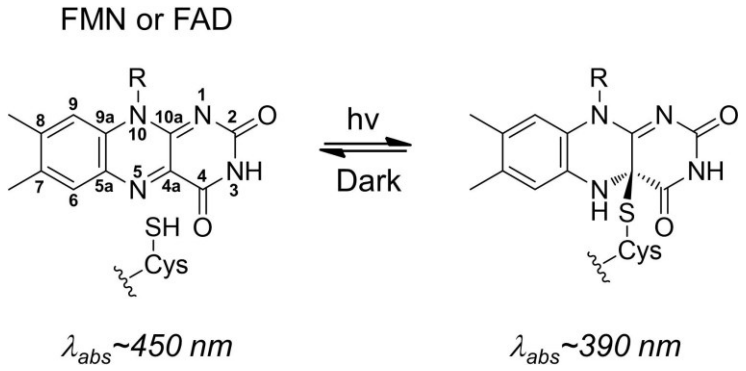

Figure 1.3. The photochemistry of LOV domains.

When expressed heterologously, LOV domains generally are able to incorporate endogenous flavins efficiently in various cell types. Some LOV domains exhibit fluorescence and have been engineered for improved brightness so they could be used as optogenetic tools for live cell imaging [74]. The resulting variants are particular useful in low-oxygen or anaerobic conditions where the chromophore formation of GFP-like proteins is impaired due to the lack of molecular oxygen (as described in section 1.6.1) [75,76]. One fluorescent variant of *Arabidopsis thaliana* phototropin 2 LOV2 domain (AtLOV2) also produces singlet oxygen upon blue-light illumination [77]. This variant, designated as mini Singlet Oxygen Generator (miniSOG), can be used as a genetically encoded photosensitizer, rather than a fluorescent reporter, to ablate surrounding proteins or even whole cells [78,79]. MiniSOG can also be used to catalyze the polymerization of diaminobenzidine into an osmiophilic reaction product to provide contrast for electron microscopy [79].

The photosensitive proteins that contain LOV domains have also been exploited as optogenetic actuators. As one example, a light-regulated DNA-binding protein, EL222, was used to control gene expression [80]. In another example, the FKF1-GIGANTEA (GI) heterodimerization pair from *Arabidopsis thaliana* was used for illumination-induced protein relocation [81]. Among all characterised LOV domains, the *Avena sativa* phototropin 1 LOV2 domain (AsLOV2) and a fungal circadian clock photoreceptor Vivid (VVD) have been most extensively used as "building blocks" for engineering optogenetic actuators.

1.3.1.1 AsLOV2

In AsLOV2, the photoreduction of its FMN chromophore destabilizes the β-sheet, leading to partial unfolding of the C-terminal α-helix (Jα) [72,82]. For optogenetic tools using AsLOV2 as the photosensory domain, the interacting moiety is typically genetically fused to the LOV domain such that the function of the interacting moiety is inhibited by steric or allosteric constraint in the dark state of the protein due Jα being in the stabilized state. Upon illumination, the inhibition can be relieved by the light-driven unfolding of Jα.

As a prototypical example of this strategy, a photoactivatable small GTPase Rac1, PA-Rac1 (**Figure 1.4a**), was constructed by fusing AsLOV2 to the N-terminus of Rac1 via an optimized peptide linkage [16]. When expressed in living cells, PA-Rac1 could be activated precisely in space and time, enabling researchers to investigate the roles of Rac1 in polarized cell movement. Structural studies of the dark-state PA-Rac1 indicated that AsLOV2 blocked the binding of Rac1 with its effectors. Coupling a steric blocking effect from AsLOV2 to POIs was believed to be a versatile route to control protein activities

optically. However, up to now, photoactivatable GTPases remain the only successes for this design strategy [16]. One other related design are the light-inhibited neurotoxins (lumitoxins) (**Figure 1.4b**), which exploit steric separation instead of hindrance [83]. Briefly, a lumitoxin is an ion channel-specific peptide toxin fused to AsLOV2 and tethered to the outer surface of cell membrane. In the dark, the toxin peptide is able to block an adjacent voltage-gated potassium channel that is expressed separately. Upon light-induced unfolding of Jα, the increased distance between the toxins and the channels reduces the possibility of blocking, and thus enables the channels to respond to membrane depolarization.

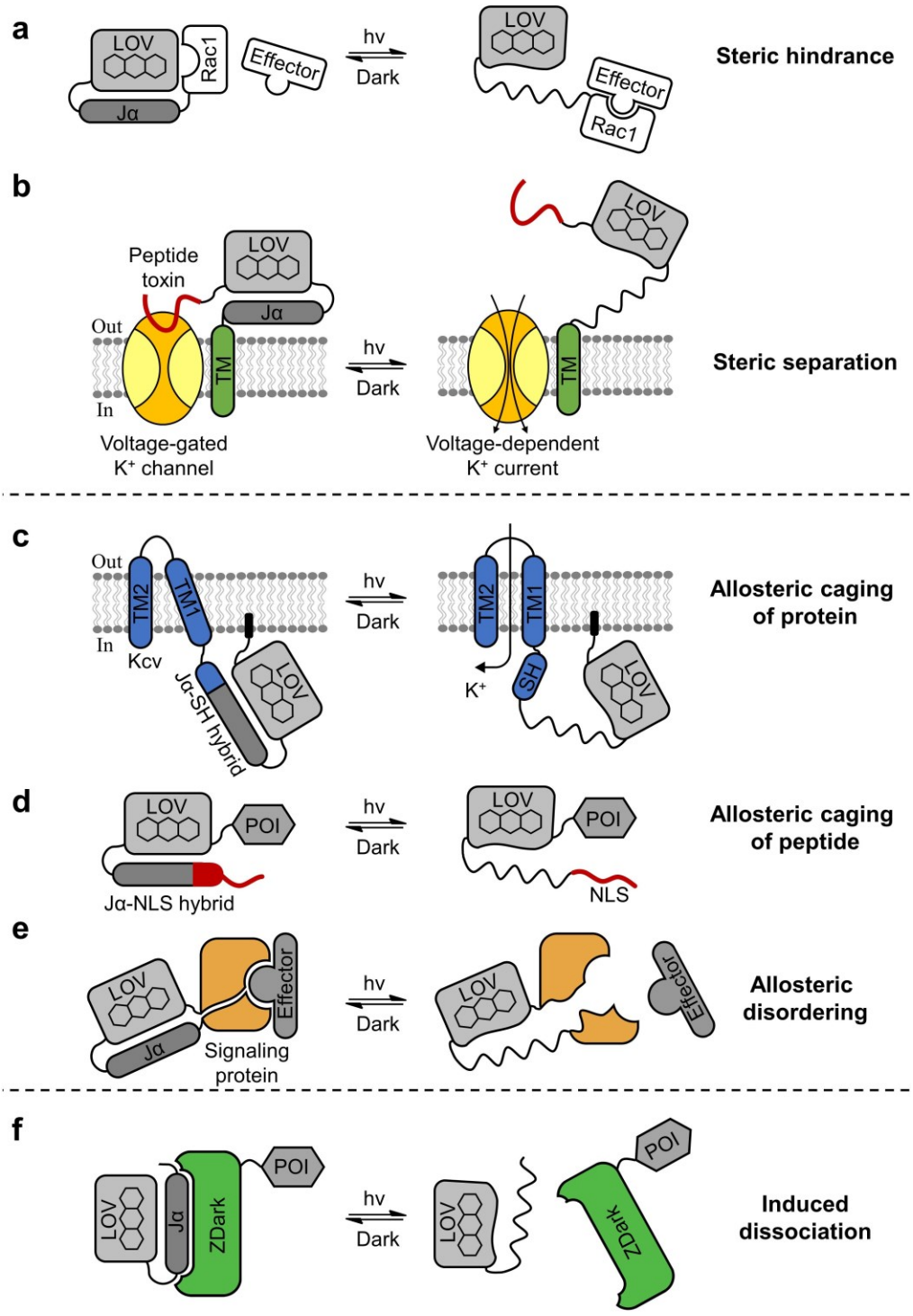

Figure 1.4. Schematic representations of AsLOV2-based actuator design strategies. The examples shown are PA-Rac1 for steric hindrance (**a**), lumitoxin for steric separation (**b**), BLINK for allosteric caging of protein (**c**), LINuS for allosteric caging of peptide (**d**), photo-controllable motility signaling proteins for allosteric disordering (**e**), and LOVTRAP for induced dissociation (**f**).

AsLOV2 has also been used for light-dependent control via allosteric mechanisms. Examples of target POIs include *Escherichia coli* (*E. coli*) dihydrofolate reductase (DHFR) [84], *E. coli* tryptophan repressor (TrpR) [85], and viral potassium (K^+) channel (Kcv) [86]. For allosteric control, AsLOV2 is genetically coupled with a protein via fusion of the C-terminal truncated Jα and a structurally important element of the POI. The fusion results in a hybrid C-terminal α-helix which, when docked in the dark-state LOV domain, effectively "cages" the element and thus disrupts the structure and function of the fused protein. Illumination causes the hybrid helix to become unstructured and release the "caged" element, leading to a restoration of protein function. As an example, a blue-light induced K^+ channel (BLINK) (**Figure 1.4c**) was engineered by fusing LOV domain to Kcv at various regions which were known to be crucial to the channel gating [86]. One insertion variant with a LOV domain fused at the N-terminal slide helix (SH) of Kcv was found to be light controllable through functional complementation screening in a potassium transport–deficient yeast strain. Variants with truncated linkages between AsLOV2 and Kcv were constructed by deleting amino acid residues from the C-terminus of Jα and the N-terminus of SH, and were screened for lower dark currents. This effort led to the discovery of a variant that exhibited the same light sensitivity, but greatly reduced background activity in the dark.

Allosteric regulation by AsLOV2 has also been harnessed to control the accessibility of small peptides to their effector proteins. These systems include, but are not limited to, TULIPs (tunable and light-controlled interacting protein tags) [87], LINuS (light-inducible nuclear localization signal) [88], and LEXY (light-inducible nuclear export system) [89]. To build these systems, the

functional peptide and Jα are typically incorporated by rational redesign of the C-terminal tail of Jα, followed with screening for variants with low resting (dark state) activity and high dynamic range. For example, to develop LINuS (**Figure 1.4d**), the tail of Jα was redesigned based on the consensus sequences of nuclear localization signals (NLSs) and over 30 variants were screened by comparing protein nuclear localization before and after light illumination in mammalian cells [88]. The resulting LINuS variant could effectively induce light-dependent relocation of its fused cargo protein to the nucleus.

A second class of LOV-mediated allosteric regulations involves the introduction of extrinsic disorder resulting from the light-induced unfolding of Jα. This approach is able to perturb the active protein conformation and thus cause protein inhibition or altered protein function. This strategy was used to engineer photoactivatable Ca^{2+} releaser (PACR) [90], optical gearshifting cytoskeletal motors (myosins and kinesins) [91], and photo-controllable motility signaling proteins including kinases, GTPases, and guanine exchange factors (GEFs) (**Figure 1.4e**) [92]. As an example, to create PACR, AsLOV2 was inserted between two EF-hands of a Ca^{2+} binding protein (CaM fused with M13) [90]. In the dark, PACR bound to Ca^{2+} with high affinity, but in the illuminated-state PACR exhibited an open conformation and bound Ca^{2+} with a tremendously increased dissociation constant (K_d). The photoexcitation and its dark reverse enabled a reversible control of Ca^{2+} level in genetically targeted cells and subcellular compartments. Recently, Dagliyan et al. reported their further efforts to explore the principle and methodology of this strategy [92]. They used computational methods to identify possible allosteric sites for LOV2 insertion, with the goal of creating a photo-inhibitable variant. They generalized

this approach and engineered 7 signaling proteins that belong to 3 different families. Furthermore, they demonstrated the potential of LOV2-insertion for the photo-activation of POI by inhibiting the action of the autoinhibitory domain (AID) of a protein.

In 2016, Wang et al. described a light-inducible protein dissociation strategy named LOV2 trap and release of protein, LOVTRAP (**Figure 1.4f**) [93]. To create LOVTRAP, they first screened an mRNA display library of the Z subunits of protein A for selective binding to the dark-state AsLOV2. This effort resulted in the identification of a synthetic protein, Zdark, which had a K_d = 26.2 nM for the dark-state LOV2 and an >150-fold decreased affinity in response to light-induced conformational change of LOV2. When co-expressed with LOV2 that was anchored away from the subcellular region where the POI acted, Zdark-POI was trapped by LOVTRAP in the dark state. Upon blue-light illumination, Zdark-POI dissociated from LOV2 and moved to its normal site of action. By introducing mutations that were reported to tune LOV2 kinetics, the time constant of LOVTRAP dark recovery could be varied from seconds to hundreds of seconds, enabling precise control of signaling in different time frames. LOVTRAP-mediated control of a group of signalling proteins including GTPases Rac1 and RhoA and GEF Vav2, was demonstrated by the visualization of light-induced cell-edge protrusion and retraction.

Despite the many successful examples of using AsLOV2 for the development of optogenetic actuators, the AsLOV2-based photoswitches generally suffer from leakiness (high background activity) and low dynamic range. Protein nuclear magnetic resonance (NMR) spectroscopy data has revealed that photoexcitation of AsLOV2 shifts the docked-undocked Jα ratio

from 98.4:1.6 (dark state) to 9:91 (illuminated state) [94], indicating that ~2% of the protein is in the undesirable active state in the dark. In attempts to address the issue, mutations have been introduced into AsLOV2 through rational design and function-based screening [12,87,95]. To further minimize the leakiness in dark, the sites and linkages of genetic fusion between functional group and Jα were often carefully chosen and screened during tool development (as described in the examples provided earlier in this section). However, the improvements are generally limited and varied in different cases. As an result, AsLOV2-based optogenetic tools require substantial optimization and even in the best-case scenarios, there will be residual activity in the dark state. In many cases this background is acceptable, given the goals of a particular experiment. However, for many types of experiments where it is critical to have negligible dark state activity, AsLOV2-based tools may not be appropriate.

1.3.1.2 VVD

The fungal photoreceptor VVD uses FAD instead of FMN as a cofactor, and undergoes a photocycle similar to that of the AsLOV2 upon blue-light illumination. The photoreduction leads to partial disorder of the N-terminal region, which causes VVD to homodimerize (**Figure 1.5a**) [96]. Wang et al. built a light-switchable transgene system, LightOn, by replacing the dimerization motif of Gal4-based synthetic transcriptional activator with VVD [97]. The fusion protein was only able to bind to its consensus cognate DNA sequence and initiate transcription upon light induced dimerization of VVD. Recently, VVD has also been inserted into T7 RNA polymerase (RNAP) and fused with one fragment of split T7 RNAP, to control its activity through allosteric effects and steric hindrance, respectively [98]. These examples

demonstrate the potential of VVD as an alternative to AsLOV2 for allosteric and steric regulation.

To extend the utility of VVD, Kawano et al. engineered pairs of VVD photoswitches (Magnets) that only exhibited light-inducible heterodimerization by rational redesign of the dimerization interface [99]. Each pair of Magnets consists of one positive Magnet (pMag) and one negative Magnet (nMag), with positively charged and negatively charged mutations, respectively (**Figure 1.5b**). Compared with natural VVD, Magnets are more suitable to control heteromeric protein-protein interaction (PPI), as their light-induced heterodimerization eliminates the possibility of forming noneffective homodimers (**Figure 1.5a,b**). Moreover, the variants with improved dimerization efficiency (MagHigh), fast switch-off kinetics (MagFast), or a combination of both (pMagFast–nMagHigh), were characterized in live cells. Magnets have enabled optogenetic control of a broad range of biological processes including phosphatidylinositol 3-kinase (PI3K) signalling [99], G protein activation [100], T7 RNAP-driven gene expression [98], CRISPR-Cas9 genome editing, and Cre-Lox recombination [101,102].

Regulating PPIs is a particularly important application for optogenetic control, as proteins rarely act alone in biological system [103]. In addition to the binding affinity which is determined by the complementarity between protein structures, the local protein concentration is another parameter that determines if a PPI will occur or not. Optical control of oligomerization states can enable researchers to exert control over PPIs by increasing or reducing the local protein concentration via light-induced relocation of fused POIs. As an example, Magnets were applied to optically activate the α subunit of

heterotrimeric Gq protein (Gαq) by fusing pMagFast with Gαq, and tethering nMagFast to plasma membrane via a C-term fused CAAX motif of K-Ras [100]. Upon blue-light illumination, the heterologously expressed pMagFast-Gαq was recruited to plasma membrane via light-induced pMagFast–nMagHigh dimerization. The increased local concentration of Gαq triggers effective Gaq-PLC interaction, which activates PLC to produce inositol 1,4,5-trisphosphate (IP3) and diacylglycerol (DAG), leading to the activation of downstream signaling pathways.

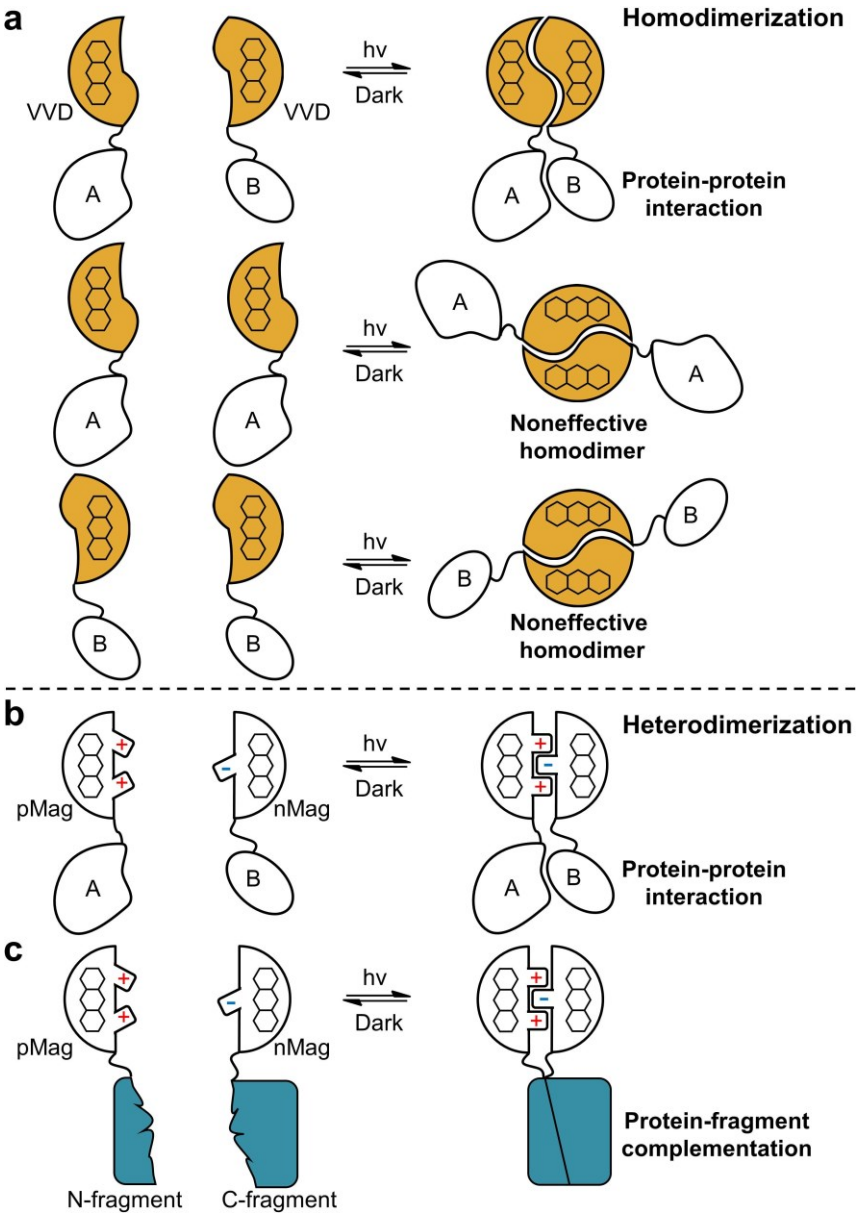

Figure 1.5. Schematic representations of VVD-based actuator design strategies. (**a**) PPI mediated by VVD homodimerization. (**b,c**) PPI (**b**) and protein-fragment complementation (**c**) mediated by Magnet heterodimerization.

In addition to conventional protein complexes, optogenetic induction of a PPI can also be used to bring together two engineered fragments of a protein. This strategy, referred to as protein-fragment complementation, involves a protein that has been genetically split into two non-functional parts. The protein is reconstituted non-covalently when the two fragments are brought in close enough proximity by the genetically fused partner proteins (**Figure 1.5c**). This approach has been widely applied to identify PPIs by using split protein reporters that could produce PPI-dependent readouts (as described in section 1.6.5) [104]. When a pair of optogenetic dimerization proteins are fused with the fragments of a split POI such that illumination results in restoration of the POI activity, the bimolecular system becomes an optogenetic actuator.

Researchers have combined protein-fragment complementation strategy with the Magnet system to engineer photoactivatable Cre recombinase (PA-Cre). Cre recombinase is an enzyme that catalyzes site-specific recombination between two DNA recognition sites (LoxP sites) to induce targeted gene deletion, insertion, translocation, or inversion in cells [105]. The Cre–loxP recombination system, as a genetic tool, has been extensively used *in vitro* and *in vivo*, to study gene function in defined cell types [106]. To engineer PA-Cre, a N-term fragment (CreN, residues 19–59) and a C-term fragment (CreC, residues 60–343) of Cre recombinase were fused to the N-terminus of nMag and the C-terminus of pMag, respectively [102]. The PA-Cre enabled precise spatiotemporal control of Cre-mediated recombination events in cell cultures.

Although the authors demonstrated activation of gene expression of luciferase using PA-Cre in mice, it remains to be seen whether the PA-Cre, along with chemically inducible and other light-inducible Cre–loxP systems [13,107–111], will be of widespread utility in the context of interrogating endogenous gene functions *in vivo*. The main concern is background recombinase activity, which has been observed in all of these inducible Cre–loxP systems.

Similarly, the type II clustered regularly interspaced short palindromic repeats (CRISPR) and CRISPR-associated protein 9 (Cas9) system, known as CRISPR-Cas9, has been engineered to be photoactivatable [101]. Cas9 is an endonuclease that associates with two RNA molecules including CRISPR RNA (crRNA) and trans-activating CRISPR RNA (tracrRNA), or one synthetic single-guide RNA (sgRNA) which is a fusion of crRNA and tracrRNA. The Cas9/RNA complex cuts a targeted DNA sequence that is complementary to tracrRNA and is upstream of a protospacer-adjacent motif (PAM) [112]. When Cas9 and sgRNAs are expressed in mammalian cells, the endonuclease activity can be "programmed" to target any genome position that is adjacent to a PAM sequence, via coding the nucleotide sequence of sgRNA [113,114]. The Cas9-mediated DNA cleavage results in a double strand break that can be repaired by non-homologous end joining (NHEJ) to induce random nucleotide insertions or deletions, or homology-directed repair (HDR) to allow template-based genome modification [115]. To engineer photoactivatable Cas9 (paCas9), Nihongaki et al. first built a series of split Cas9 candidates with 18 distinct split sites at the loop regions as revealed by the Cas9 crystal structure. This series of candidates was screened for high differences in activity before and after chemically induced dimerization. The most promising candidate Cas9 fragments were then

genetically fused to pMag and nMagHigh [101] to create the paCas9 system. Upon illumination, paCas9 reconstituted and performed sgRNA-guided genome editing in mammalian cell cultures. Similar spilt Cas9 systems were reported nearly simultaneously [116,117]. However, all of these systems appear to have background activity of Cas9, mainly due to the inherent association tendency between two split fragments. The background activity may limit their utility for *in vivo* applications. One approach for overcoming this limitation could be to use a protein complementation system including the nuclease-deficient Cas9 (dCas9) and the catalytic domain of FokI restriction endonuclease [118], as they have no potential to associate.

1.3.2 Cryptochromes

Another flavoprotein that is commonly used for tool development is *Arabidopsis* cryptochrome 2 (CRY2). In CRY2, the conformational changes induced by the photoreduction of its FAD chromophore (**Figure 1.6a**) lead to two coexistent protein interactions: binding with the cryptochrome-interacting basic-helix-loop-helix protein (CIB1) and formation of a homo-oligomer (clustering) (**Figure 1.6b**) [119–121].

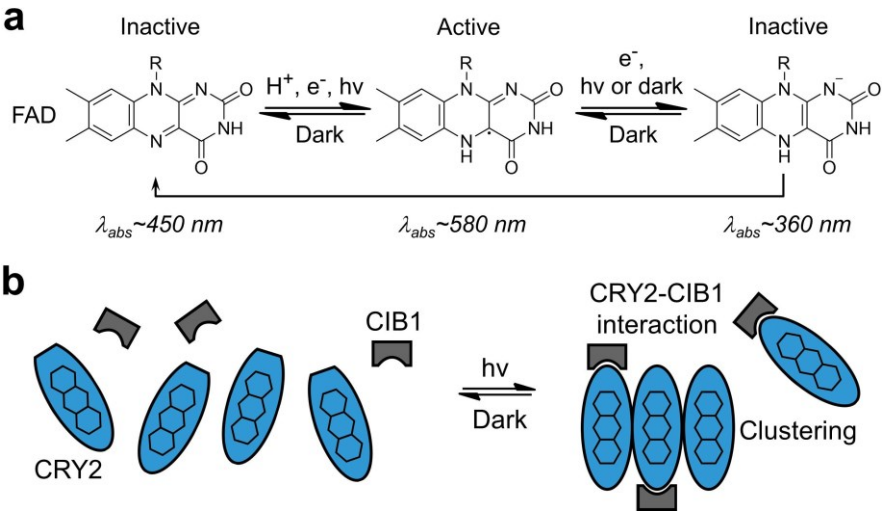

Figure 1.6. Cryptochrome 2. (**a**) The photochemistry of CRY2. (**b**) Schematic representation of the light-induced CRY2-CIB1 interaction and CRY2 clustering.

In 2010, Kennedy et al. demonstrated the utility of the light-induced CRY2-CIB1 interaction to control protein translocation, gene transcription, and Cre recombinase-mediated DNA recombination in mammalian cells [122]. In this work, the fragments of split Gal4 transcription factor and Cre recombinase were coupled with CRY2 and CIB1 genetically to enable optogenetic restoration of Gal4 and Cre protein activities (**Figure 1.7a**). Since then, the CRY2-CIB1 has become one of the most widely used photoswitchable proteins and has been adapted for manipulation of many different biological processes via light-induced PPI. These processes include, but not limited to, RhoA GTPase-mediated regulation of cellular forces and mechanotransduction [123]; activation of the Raf/MEK/ERK cascade [124]; Akt (protein kinase B) signaling [125,126]; inhibition of G protein activation [127]; control of contractile forces [128]; control of actin dynamics [129]; and control of organelle distribution [130] (**Figure 1.7b**). In addition, CRY2-CIB1 interaction has also been used to optically target POIs to subcellular locations (**Figure 1.7c**). For example, endogenous transcription and epigenetic states were controlled optically using CIB1-tagged transcription activator (VP16) and histone effectors. These activator and effectors were targeted to chromosomes via site-specific genomic anchors consisting of a CRY2 fused customizable DNA-binding domain derived from transcription activator-like effectors (TALEs) [131]. Similar systems have also been generated by using dCas9 and sgRNA as the genomic anchors [132,133]. This strategy was also exploited to control phosphoinositide

metabolism using the CRY2-fused catalytic subunits of inositol 5-phosphatase and PI3K which were recruited to membrane-tethered CIB1 [126,134–136]. Similarly, this strategy has been used to optically load exosomes with CRY2-fused POI via the targeted CIB1 for light-dependent intracellular protein delivery [137]. Recently, Taslimi et al. engineered second-generation CRY2-CIB1 photodimerizers [13]. Through systematic testing of CRY2 and CIB1 truncations and the directed evolution of CRY2, they identified new CRY2-CIB variants with enhanced dynamic range, reduced dark interaction, and tuned (longer or shorter) photocycles.

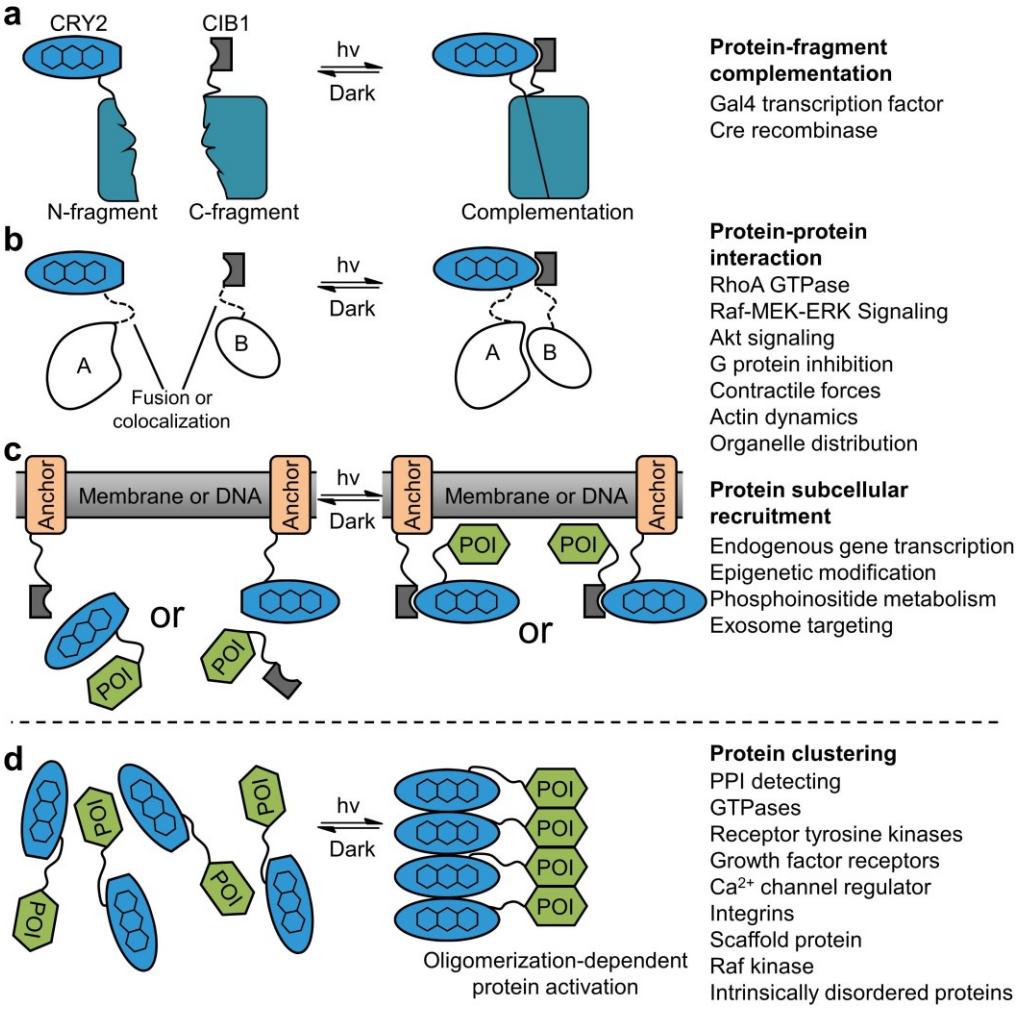

Figure 1.7. Schematic representations of CRY2-based actuator design strategies. (**a,b,c**) Protein-fragment complementation (**a**), PPI (**b**), and protein subcellular recruitment (**c**), mediated by CRY2-CIB1 interaction. (**d**)

Oligomerization-dependent protein activation mediated by CRY2 clustering. The examples for each strategy are listed in the right column.

The light-induced clustering of CRY2 was first reported in 2000 [120]. Bugaj et al. demonstrated that optically induced clustering could be adapted to control cell signalling in mammalian cells [138]. However, the clustering of wild-type CRY2 is moderate. In 2014, Taslimi et al. discovered a CRY2 mutant with enhanced clustering and used it to probe and control PPIs [139]. Though the applications of light-induced homo-oligomerization have been relatively limited compared with that of CRY2-CIB1 interaction (as explained in section 1.3.1.2), it is particularly suitable to control the function of proteins that intrinsically participate in oligomerization-dependent processes (**Figure 1.7d**). Some demonstrated examples include: RhoA and Rab GTPases [138,140]; receptor tyrosine kinases (RTKs) [141]; growth factor receptors (GFRs) [134,142,143]; integrins [142]; scaffold protein [144]; the regulator protein of Ca^{2+} release-activated Ca^{2+} (CRAC) channel, STIM1 [145]; Raf kinase [146], and the intrinsically disordered protein regions of RNA/protein (RNP) body proteins which can modulate intracellular phase transitions [147].

To further improve protein clustering, Taslimi et al. also combined light-induced CRY2-CIB1 interaction and CRY2 oligomerization by fusing CRY2 and CIB1 to a POI and a multimeric protein domain of CaMKII (MP), respectively (**Figure 1.8**) [139]. Upon illumination, the interaction between the POI and its partner (tagged with a fluorescence protein), could be visualized via the formation of the fluorescent clusters in live cells. The same strategy has also been used to develop a versatile approach for reversibly inactivating proteins [148]. CRY2-POI, coexpressed with CIB1-MP, is functional in the dark, but

upon blue-light illumination, the CRY2-POI becomes trapped in the light-triggered protein complexes and isolated from its effectors, leading to the spatiotemporal reduction of the protein activity (**Figure 1.8**).

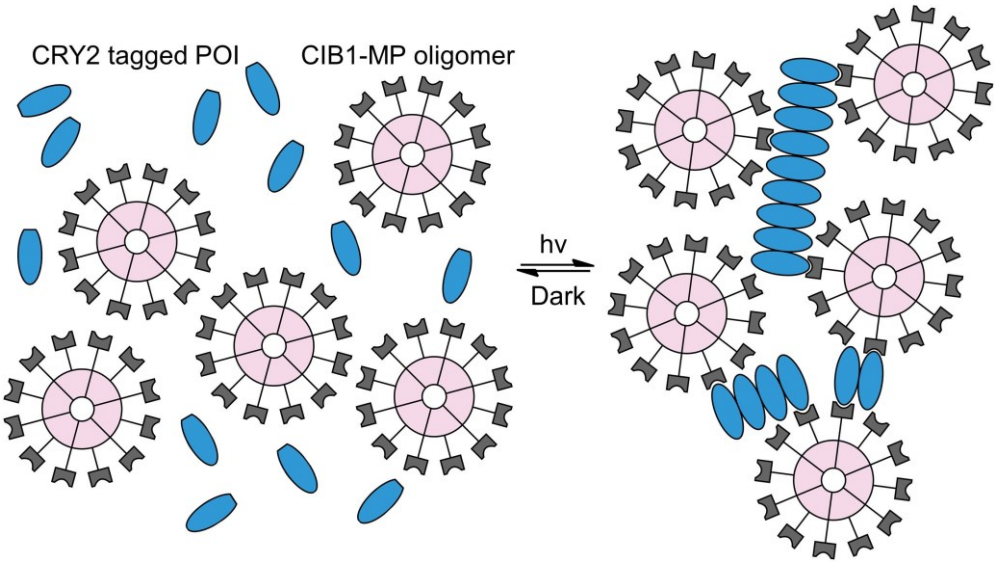

Figure 1.8. Schematic representation of improved protein clustering mediated by CRY2 and CIB1-MP oligomer.

1.3.3 BLUF domain

In addition to the commonly used photosensory domains discussed in the preceding sections (AsLOV2, VVD and CRY2), other photosensitive flavoproteins, including the blue light sensor using FAD (BLUF) domain, have been used to control cells optogenetically. In terms of structure, a BLUF domain simply consists of an FAD chromophore, an FAD-binding pocket formed by two α-helices, a β-sheet, and a variable C-terminal α-helix [149]. Photoreduction of the flavin results in a rearrangement of its hydrogen bonds with residues projecting from the β-sheet (**Figure 1.9**) [150,151]. This rearrangement induces a conformational change in the BLUF domain that propagates through the β-sheet or C-terminal α-helix and allosterically modulates the structure of the fused responsive domain [152]. The

photoexcitation is thermally reversible within seconds to minutes in the dark [153]. The BLUF domain was first identified in transcriptional antirepressor AppA. It was later found to be the photosensory moiety of a variety of proteins including photoactivated adenylyl cyclases (PACs), phosphodiesterase, and other signaling proteins [154]. Among these, *Euglena gracilis* PAC (euPACα) and bacterium *Beggiatoa* PAC (bPAC) have been adapted to manipulate of cellular cyclic adenosine monophosphate (cAMP) level in various cell types and behaving animals [155–159]. Moreover, the bPAC was converted into a guanylyl cyclase by the introduction of rationally designed mutations. The resulting variant exhibited a reduced dynamic range for photoactivation, but a 10:1 selectivity for cGMP production over cAMP production [160]. This system has been expressed in rats and used for inducing increases in intracellular cGMP concentration optogenetically [161]. While there have been a number of impressive applications of BLUF domains, overall, their optogenetic applications remain limited. Most of the optogenetic applications of BLUF domains have used naturally occurring transducer/enzyme combinations and there have been few efforts to engineer the system to create non-natural optogenetic tools.

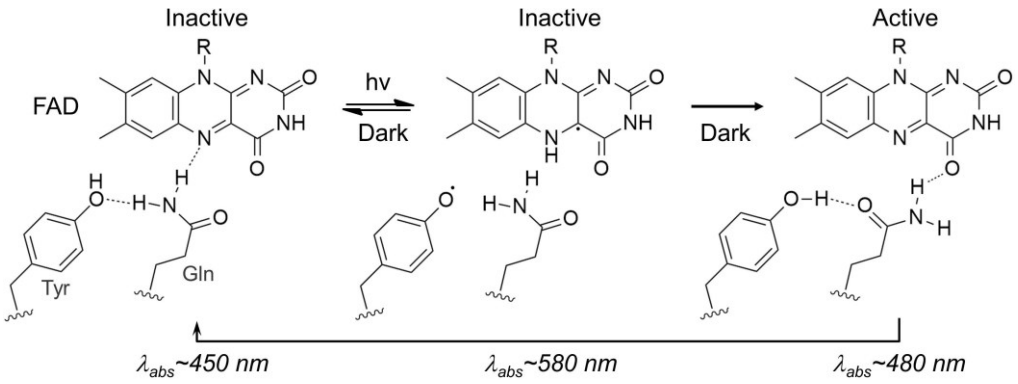

Figure 1.9. The photocycle of BLUF domains.

1.4 UVR8

Unlike visible light (wavelength ~390 – 700 nm) that is typically harmless or even beneficial to the growth of species, the high-energy UV (wavelength ~10 – 390 nm) component of sunlight can potentially damage key biomolecules such as proteins, lipids, and DNA, to the detriment of normal cellular processes. Fortunately, exposure to sunlight rarely causes UV-induced damage to animals such as ourselves, because most highly damaging UV wavelengths (< 295 nm) are absorbed by the ozone (O_3) layer. Species that live on sunlight, like plants, have also evolved efficient defenses against other damaging UV wavelengths known as UV-B (wavelength ~280 – 320 nm) [162]. In plants, the UV-B perception and response pathway involves UV-B receptor protein UVR8 (UV-B resistance 8), E3 ubiquitin ligase COP1 (constitutive photomorphogenesis 1), and transcription factor HY5 (elongated hypocotyl 5) [163]. Structurally, UVR8 contains 7 blade-shaped β-sheets and exists as a homodimer in the absence of UV-B [164]. Upon low-level UV-B illumination, UVR8 monomerizes and interacts with COP1 (**Figure 1.10**), leading to silencing of its E3 ubiquitin ligase activity against HY5. The elevated HY5 level will, in turn, induce the expression of several UV-B responsive genes [163]. Light-induced monomerization is reversible on a timescale of hours in plant, and irreversible in non-plant cells [165]. Unlike other known photosensitive proteins that use a bound or post-translationally formed chromophore, the chromophore of UVR8 is its intrinsic tryptophan residues. Tryptophan absorbs UV-B light and transfers the excited electrons to adjacent arginine residues, leading to dimer dissociation via the disruption of hydrogen-bonded salt bridges between the arginine

residues and acidic amino acid residues (Asp and Glu) across the dimer interface [164,166].

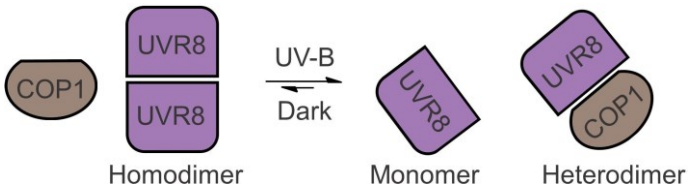

Figure 1.10. Schematic representation of UVR8 monomerization and interaction with COP1 in response to UV-B illumination.

Inspired by mechanistic studies of UV-B perception, Crefcoeur et al. utilized light-induced UVR8-COP1 heterodimerization to activate protein translocation and gene transcription [167]. Despite the phototoxicity of UV-B, which was present even at low illumination levels, UV-B remains an attractive element for optogenetic tool development. Notably, its excitation wavelength is spectrally orthogonal to those of most other photosensitive proteins, possibly enabling multicolour optogenetics. For example, Muller et al. used UVR8 in combination with VVD and Phytochrome B (PhyB) to control the expression of three genes with three colours of light (UV-B, blue, and red) in mammalian cells [168]. Moreover, the photoinduced dissociation of the UVR8 homodimer has been applied to engineer light-triggered protein secretion system in neurons, by fusing protein cargo to tandemly linked UVR8 domains [169]. The fusion proteins formed clusters via intermolecular cross-dimerization, and were retained in the endoplasmic reticulum. Upon UV-B illumination, the clusters dissociated and trafficked through the secretory pathway to cell membrane.

1.5 Photoactive yellow protein

Photoactive yellow proteins (PYPs) are bacterial photoreceptor domains [170]. Like LOV domains, they belong to the PAS domain family and consist of a 6-stranded β-sheet packed by six α-helices [171]. PYP senses light with a *trans-p*-coumaric acid (pCA) chromophore, which is covalently attached to the protein via a thioester bond to a Cys side chain. Blue light triggers the *trans*-to-*cis* isomerization of pCA (**Figure 1.11**), leading to partial unfolding of the N-terminal α-helices and the exposure of a hydrophobic surface [172–174]. The lifetime of the bright state can range from 1 ms to 1 h [175,176]. PYPs have been engineered to serve as components of optogenetic actuators, including photo-switchable DNA-binding proteins [177–179], and a photo-inhibitable dominant negative (DN) inhibitor for CREB [180]. These actuators were constructed by creating a hybrid between the N-terminal region of PYP and the C-terminal region of the POI. The hybrid regions of PYP and POI were either destabilized or un-masked allosterically by the PYP core in response to blue light. Accordingly, light-induced inhibition and activation have both been accomplished by using PYP. Though PYP-mediated allosteric control has not been intensively exploited, variants with millisecond photocycles [181–183] are particular attractive candidates for high-frequency regulation which cannot be accomplished with photosensitive domains other than microbial opsins.

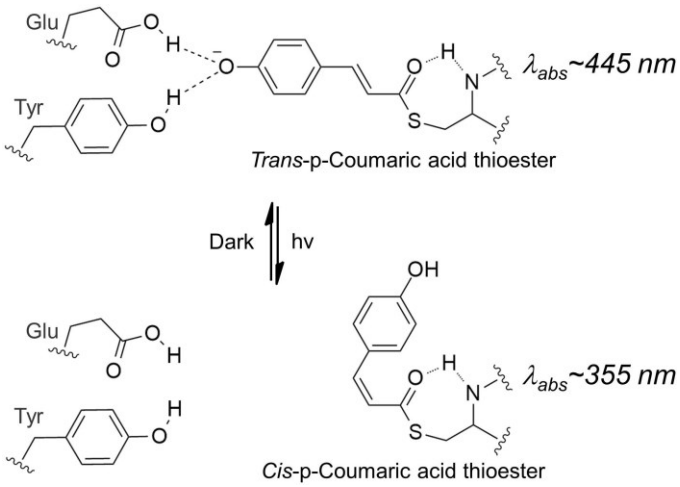

Figure 1.11. The photochemistry of PYP domains.

1.6 Fluorescent proteins

1.6.1 Green fluorescent protein

In 1962, Osamu Shimomura discovered a green fluorescent protein (GFP) in the purified bioluminescent extract of *Aequorea victoria* jellyfish [184]. Its spectral properties were later characterized [185] and the structure of the conjugated system of the light emitting chromophore determined by Shimomura [186]. The complete chromophore structure was revised and corrected after the complete GFP sequence was determined [187]. In 1992, Prasher et al. cloned the GFP gene and determined that the protein is a 238 amino acid polypeptide of molecular weight (MW) ~27 kDa [188]. The chromophore is covalently bound and forms from a tripeptide (serine-65-tryrosine-66-glycine-67) in the native protein. The precise mechanism of chromophore maturation remains controversial [189–193]. **Figure 1.12** shows the generally accepted mechanism: (1) pre-folding into a nearly native conformation, (2) cyclization, (3) oxidation, and (4) dehydration [193]. This process is completely self-sufficient.

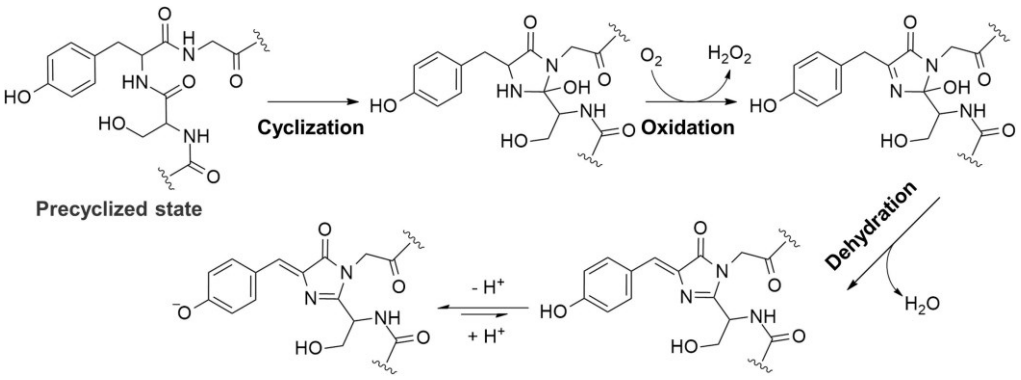

Figure 1.12. Mechanism of GFP chromophore formation.

In 1992, Martin Chalfie et al. used GFP as a marker for gene expression in selectively targeted worm cells [194]. In 1994, Roger Tsien and coworkers experimentally demonstrated that the polypeptide chain of GFP inherently contains all the requirements to form the chromophore, provided that molecular oxygen is present [195]. This property distinguishes GFP from most other protein photoreceptors that incorporate a chromophore present in the cellular environment. This feature enables the robust heterologous expression of GFP as biotechnological tags and probes in almost all subcellular organelles, tissues, and organisms. The only exception are some rare low-oxygen or anaerobic conditions, such as in the solid tumor tissues and biofilm-forming microbes [196,197]. Fluorescent reporters that can be used in the absence of oxygen have been developed using LOV domains (as described in section 1.3.1).

The wild-type *Aequorea Victoria* GFP (avGFP) quickly became a very popular biomolecular reagent for fluorescence microscopy. However, initially it was only available as a single-colour (green), and had relatively low brightness, poor photo-stability, slow maturation at 37 °C, and a double-peaked excitation spectra [185,198,199]. Over the years, many different mutants of GFP have been engineered through rational design and, more predominantly,

directed evolution. Some of the key mutants include GFP (S65T) with increased brightness and photo-stability, and a single-peaked excitation spectrum [198]; and enhanced GFP (EGFP) containing F64L point mutation which speeds up protein folding at 37 °C [200]. Protein engineering efforts have greatly expanded the applications of GFP. One of the most important is to study localization and quantity of POIs in live cells, which is achieved by simple genetic fusion of the gene encoding GFP and the gene encoding the POI to create a chimeric protein product.

1.6.2 Colour variants

With only one colour of FP, i.e., avGFP, multiple biological events could not be visualized simultaneously in live cells. Fortunately, the initial efforts to engineer avGFP in the lab of Roger Tsien also resulted in blue, cyan and yellow colour variants, named as BFP, CFP, and YFP, respectively [195,201,202]. To create BFP and CFP, the GFP chromophore-forming tyrosine was replaced with a histidine and tryptophan, respectively. The resulting chromophores had less extended conjugation and higher energy than the ionized tyrosine-derived chromophore, leading to blue-shifted spectra [201]. For YFP, the red-shifted spectrum resulted from introduction of a tyrosine residue that stacks with the chromophore through a π-π interaction, and thereby decreases the energy of the excited state [202]. This small palette of colour variants allowed multicolour imaging, and the detection of biological processes by Förster resonance energy transfer (FRET) between FPs with two different colours (as described in section 1.6.5).

Further expansion of the palette of the genetically encoded fluorophores occurred with the discovery of homologues of GFP in corals. These coral-

derived FPs exhibit hues ranging from cyan to red [203]. The structures of coral FPs are similar to that of avGFP, sharing the characteristic 11-stranded β-barrel with a central helix that contains the chromophore (**Figure 1.13a**) [202,204]. However, the coral FPs generally form obligate tetramers [203], unlike avGFP which is only weakly dimeric with an estimated K_d of ~100 μM [205]. As the tetrameric structure may perturb the function of the fused proteins [206,207], the wild-type coral FPs were not generally useful as fluorescent tags. To overcome this limitation, a general FP-monomerization strategy was developed in the lab of Roger Tsien [208]. It includes two key steps: (1) rationally designed point mutations to break the interfaces for oligomerization; and (2) directed evolution to rescue the original fluorescent properties. This strategy was first applied to convert the tetrameric *Discosoma* red FP (RFP) [209] to a monomeric RFP known as mRFP1 [208]. Since then, many oligomeric GFP-homologues have been monomerized to expand the scope of optogenetic reporters [210–212]. **Figure 1.13b** shows chromophore structures for some of the FP colour variants.

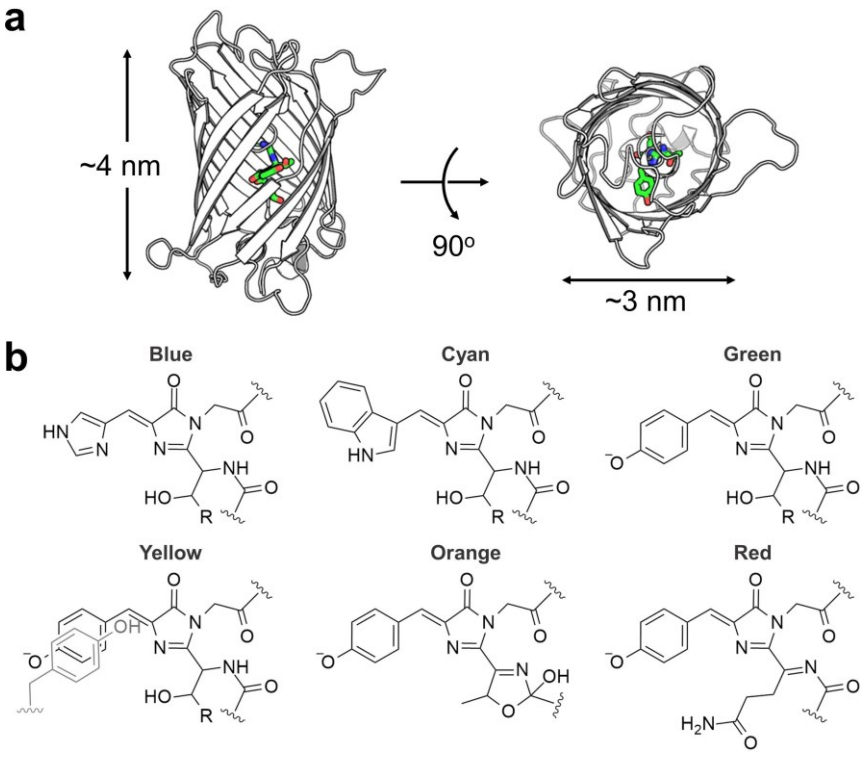

Figure 1.13. GFP-like fluorescent proteins. (**a**) Three-dimensional structure of a FP monomer. Shown is a rendering of the avGFP structure (PDB ID 1EMA [202]). (**b**) Chromophores of various FP colour variants.

1.6.3 Phototransformable FPs

In addition to photon emission (fluorescence), photoexcitation of GFP-like proteins can also trigger chemical reactions at the chromophore, leading to changes in the optical properties. This phenomenon is called phototransformation and FPs that undergo pronounced phototransformation are generally referred to as phototransformable FPs [213]. Based on the different outcomes of phototransformation, phototransformable FPs can be subdivided into three main classes: photoactivatable FPs, photoconvertible FPs, and photoswitchable FPs. **Figure 1.14** shows example photochemical mechanisms for the three classes: (1) photoactivation is the result of chromophore conversion from a neutral to anionic state, induced by the decarboxylation of a Glu residue adjacent to the chromophore [214,215]; (2) photoconversion refers to a green-to-red spectra shift caused by the extension of chromophore conjugation system involving a breakage of the polypeptide backbone [216,217]; and (3) photoswitching is a process of reversible photo-induced *cis-trans* isomerization of the chromophore [218,219]. In contrast to conventional FPs which, ideally, exhibit constant and unchanging fluorescence during imaging, phototransformable FPs change their fluorescence intensity or wavelength upon illumination. The change of fluorescent properties enables the tracking of objects with enhanced temporal-special resolution [220–223]. One of the high-profile applications of phototransformable FPs is in super-resolution imaging with photoactivated localization microscopy (PALM) [223,224].

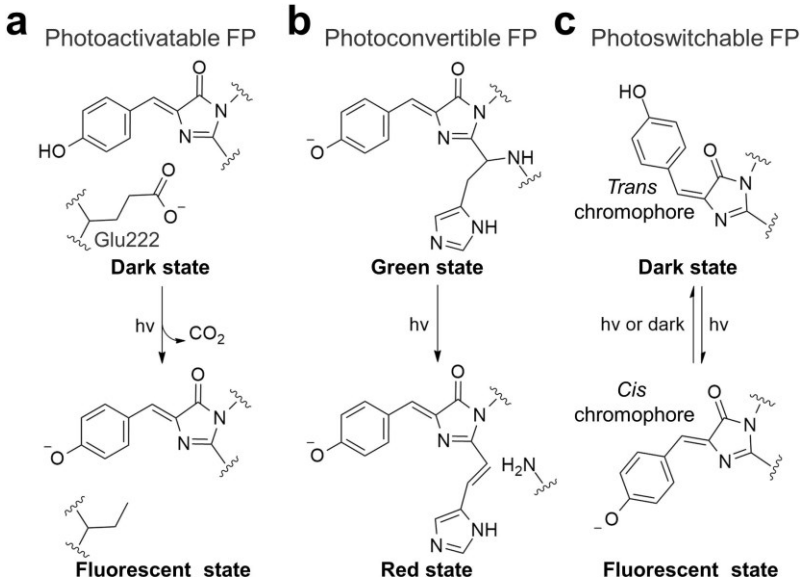

Figure 1.14. Representative photochemistry of phototransformable FPs. (**a**) Photoactivation. (**b**) Green-to-red photoconversion. (**b**) Photoswitching.

1.6.4 FP-based actuators

The photochemistry occurring at the chromophore of a phototransformable FP is usually assisted by the surrounding amino acid residues. Likewise, changes in the chromophore structure or conformation can induce conformational rearrangements of the chromophore pocket [219,225–227]. For example, the chromophore *cis-trans* isomerization of the photoswitchable FP Dronpa destabilizes several of the β-strands and causes partial unfolding of the protein barrel [227]. In 2012, Zhou et al. reported that this light-induced conformational change could effectively convert Dronpa (K154N) from a tetramer to a monomer with the K_d changing from 9.9 μM to >100 μM [228]. A dimeric version of Dronpa has also been developed [228,229]. The low affinity of Dronpa variants hinders their use in LOVTRAP-like applications (as described in section 1.3.1.1). However, they are suitable for "intramolecular oligomerization"-based applications, which involve fusing two copies of Dronpa with the POI. In this situation, the protein activity can be

caged by steric hindrance due to association of the two Dronpa monomers. Illumination causes an increase in K_d, leading to dissociation of the Dronpa monomers and an increase in POI activity (**Figure 1.15**). This strategy has been applied to POIs including the Cdc42 GEF intersectin, HCV protease and kinases Raf1, MEK1, MEK2, and CDK5 [228,229]. Prior to the work described in Chapter 2, no other class of phototransformable FPs had been exploited to build optogenetic actuators.

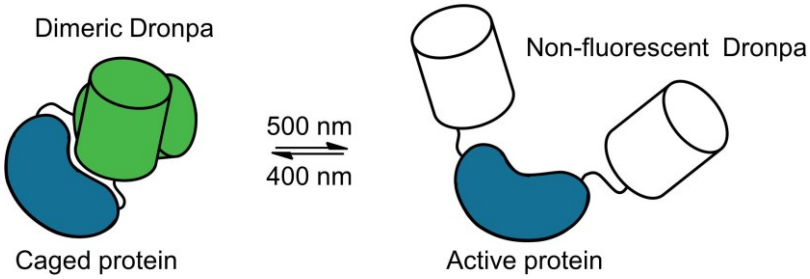

Figure 1.15. Schematic representation of Dronpa-based actuator design strategy.

1.6.5 FP-based indicators

The engineering of FPs has enabled non-invasive, real-time imaging of subcellular protein localization to become a routine experiment in biological research. To shine light on a wider range of biological processes, such as PPIs, analyte fluctuation, and enzymatic activity, researchers have engineered FP-based indicators that can change their fluorescence profiles in response to biochemical stimuli. Though some avGFP mutants are inherently sensitive to H^+ and Cl^- ions [15,230–232], FPs are generally inert to analytes encountered in the cellular environment. Several strategies have now been developed to transduce cellular dynamics into fluorescence changes. These strategies fall into three classes: bimolecular fluorescence complementation (BiFC); Förster

resonance energy transfer (FRET); and allosteric modulation of the FP chromophore environment.

Protein-fragment complementation has often been utilized to manipulate protein activity (as described in section 1.3.1.2). It is also a useful strategy to engineer biosensors, when the proximity-induced reconstitution of a split protein can produce a read-out. Some of the reporter proteins that have been successfully split and reconstituted include: antibiotic-resistant proteins [233,234]; chromogenic or fluorogenic enzymes [234–236]; luciferases [237–240]; and transcription factors [241]. Split avGFP variants were first reported in 2000 [242] and were later used to report PPIs in live cells. To report PPIs, the non-fluorescent N- and C-terminal FP fragments are fused to candidate POIs that are suspected to interact (**Figure 1.16a**) [243–245]. The FP-based protein complementation is also known as bimolecular fluorescence complementation (BiFC) [243], which has been applied to FPs with different hues ranging from blue to far red [246–250]. Disadvantages of the BiFC approach are the slow kinetics of chromophore formation and the irreversibility of the FP reconstruction [243]. To overcome the limitations, Alford et al. developed dimerization-dependent FPs (ddFPs) as a fast and fully reversible alternative. (**Figure 1.16b**) [251–253]. Instead of structurally splitting one FP, Alford et al. engineered a palette of FP pairs. Each pair consists of one FP (ddFP-A) that is dimly fluorescent in its monomeric state, but becomes significantly brighter upon binding with the other FP copy (ddFP-B) that is not fluorescent.

FRET is nonradiative energy transfer from one chromophore (donor) to another (acceptor) via dipole–dipole coupling which requires the donor emission and the acceptor absorbance to overlap in terms of wavelength. When

the parameters of donor quantum yield, acceptor extinction coefficient, and spectra overlap are fixed, the FRET efficiency is only dependent on the distance and relative orientation between donor and acceptor [254]. For most FP-based FRET pairs, their FRET efficiency is most sensitive at donor to acceptor distances between 3 nm and 9 nm (**Figure 1.16c**) [254,255]. Accordingly, fusing FP FRET pairs with a POI or POIs can enable fluorescent indication of a wide variety of biological events that occur on the length scale. For example, FRET can be used to investigate protein conformational changes (when donor and acceptor are both fused to one POI), and PPIs or relative protein proximity (when donor and acceptor are fused to two different POIs). FRET is a highly versatile strategy for engineering of biosensors [256].

The third strategy for engineering FP-based biosensors is to engineer allosteric control of FP fluorescence properties. For this strategy, protein domains that can change their conformation or oligomerization state in response to biological stimuli, are fused with FPs at sites that are structurally adjacent to the chromophore. Since the N- and C-termini of FPs are far from the chromophores (which is buried near the center of the β-barrel [202,204]), simply fusing the interacting protein to one of the termini typically does not produce the desired allosteric control of fluorescence. Rather, interacting proteins can be inserted into the β-barrel or linked to the termini of a circularly permutated FP (cpFP), in which the original N- and C-termini are joined by a peptide linker and new termini have been introduced close to the chromophore (**Figure 1.16d**) [257–259]. Examples include, but not limited to: Ca^{2+} indicators, including GCaMPs, PeriCaMs and GECOs [17,258,260,261]; voltage indicators, ASAP and FlicR [251,262]; adenosine triphosphate (ATP) -

adenosine diphosphate (ADP) indicator Perceval [263,264]; and glutamate indicator GluSnFR [265].

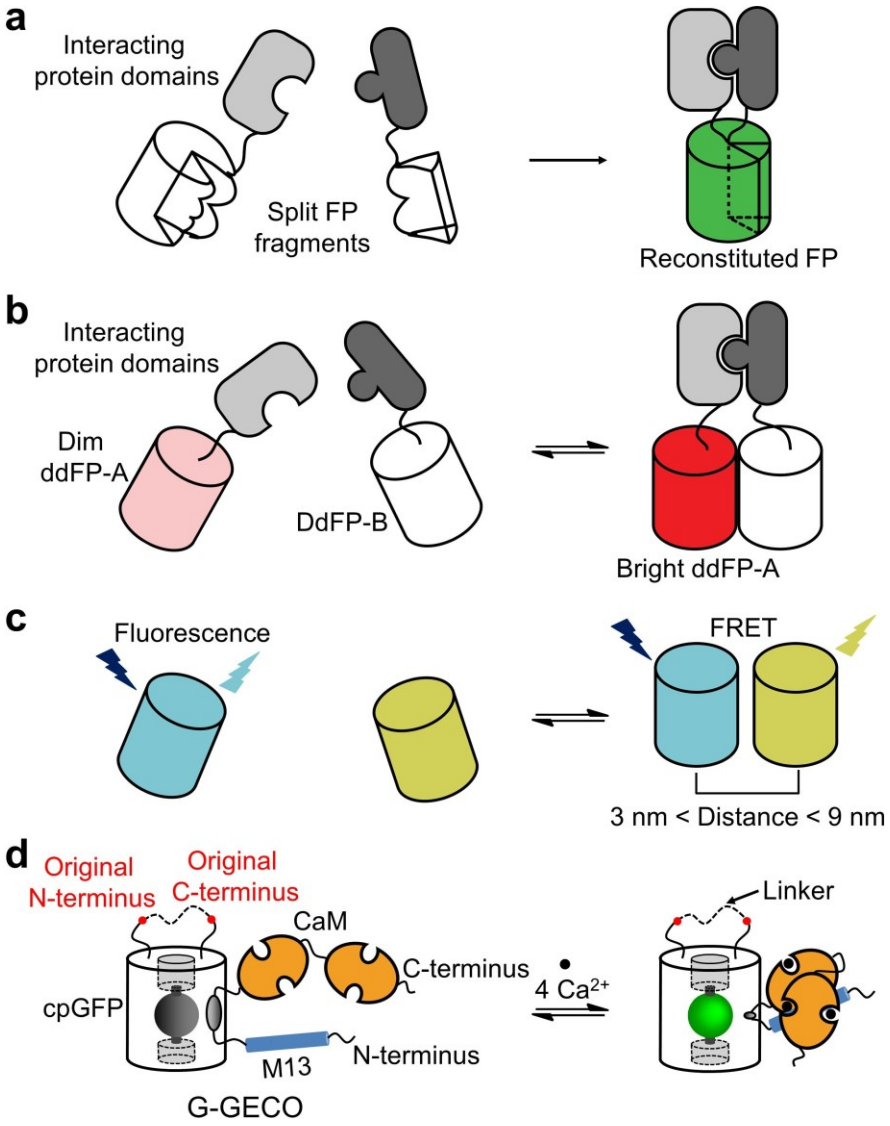

Figure 1.16. Schematic representations of FP-based indicator design strategies. (**a**) BiFC. (**b**) DdFP. (**c**) FRET. (**d**) Allosteric effect. The example shown is G-GECO**.**

1.7 Phytochromes

The phytochromes are a family of red/far-red light-sensing proteins first discovered in plants and later in cyanobacteria, bacteria, and fungi [266]. The phytochromes covalently bind a linear tetrapyrrole bilin as the chromophore.

These bilin have an extensive conjugation system and phytochromes therefore have the most red-shifted excitation wavelength among all the known photoreceptor proteins. **Figure 1.17a** shows the excitation wavelength ranges of photoreceptor proteins described in this chapter. Non-invasive *in vivo* optogenetic control and imaging (with tissue depth ranging from ~0.1 to 1 cm) requires the use of light within the "NIR optical window" (wavelength ~650 – 900 nm). Light in this region exhibits lower scattering and phototoxicity than visible light, as well as minimal absorption by hemoglobin, melanin, and water within mammalian tissue [267]. As the phytochromes can absorb light with wavelengths ranging from 620 to 800 nm [268], they are attractive templates for the development of optogenetic tools including actuators and indicators.

1.7.1 Phytochrome-based actuators

As naturally photosensitive proteins, the phytochromes typically consists of a C-terminal module with a biological function, and a N-terminal photosensory module which contains the bilin chromophore. Upon illumination, the bilin undergoes reversible photoisomerization (**Figure 1.17b**) and induces protein conformational changes that allosterically change the biological function of the C-terminal module [269,270]. The activation and deactivation of phytochromes can be driven bidirectionally with light. Cyanobacterial and plant phytochrome-based photoswitches have been used to control biological processes heterologously [271–274]. A representative example is the Phytochrome B (PhyB) -Phytochrome Interaction Factor (PIF) heterodimer which can be fast turned on and off by red and far-red light, respectively (**Figure 1.17c**) [272]. The PhyB-PIF interaction has been adapted to regulate protein location and PPIs in cells. Some examples include: light-switchable gene

expression [275–277]; protein splicing [278]; cell protrusion [272]; protein translocation [279–281]; organelle targeting [282]; actin assembly [283]; and signal-cascade activation [284,285]. One limitation of this system is the requirement for exogenous phytochromobilin (PΦB) or phycocyanobilin (PCB) chromophores that are not available in mammalian cells and, when added, cannot diffuse deep into tissues [286].

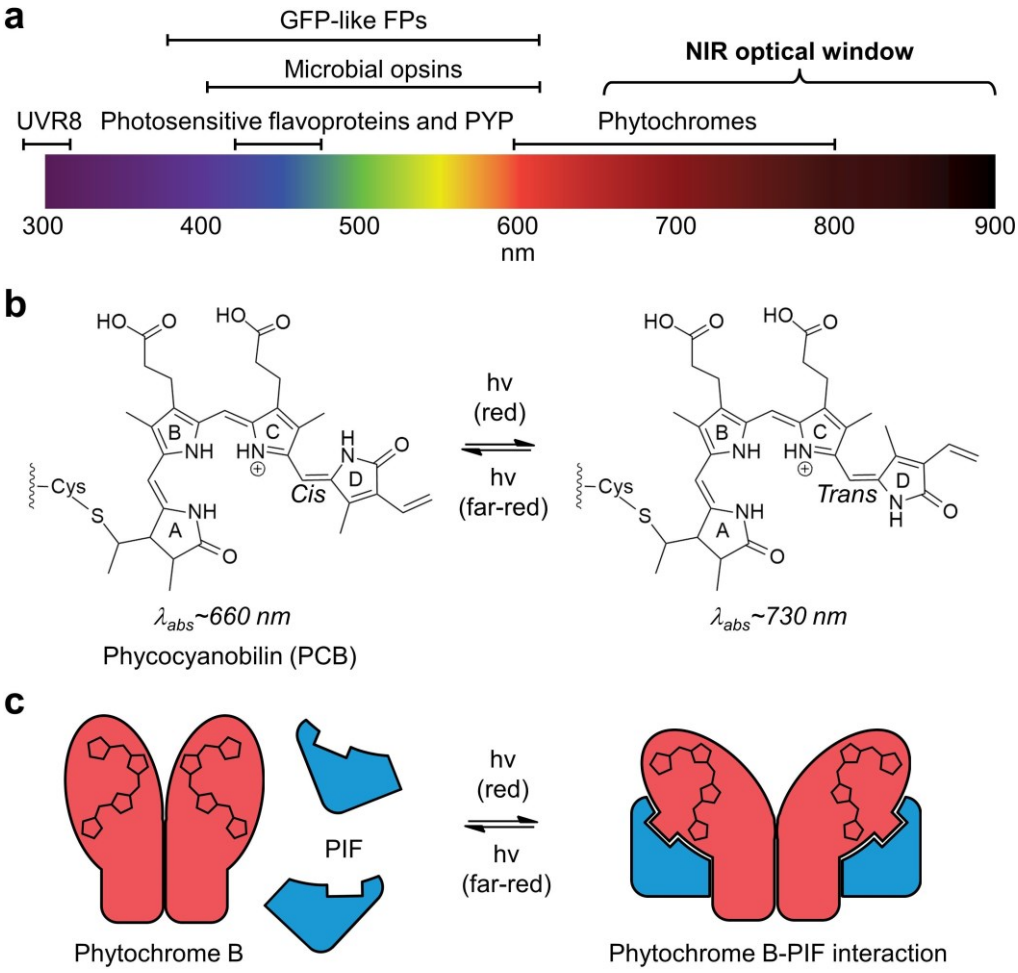

Figure 1.17. Phytochromes. (**a**) The effective excitation wavelength ranges of common photoreceptor proteins and the NIR optical window. (**b**) The photochemistry of PhyB from *Arabidopsis thaliana*. (**c**) Schematic representation of the reversible interaction between PhyB (including the C-terminal tandem PAS repeat which dimerizes the protein) and PIF [272].

1.7.2 Bacterial phytochromes

In contrast to the plant-derived phytochromes, the bacterial phytochromes are able to use the endogenous biliverdin (BV) as their chromophore. This bilin is ubiquitously present in mammalian cells [287] and the bacterial phytochromes are therefore more feasible for optogenetic applications in rodent models. In 2009, Shu et al. first demonstrated the potential of bacterial phytochromes for cell imaging by developing a photosensory module that had been evolved for bright fluorescence [288]. Since then, many fluorescent variants of bacterial phytochromes have been developed. These variants include ones with improved BV binding, altered fluorescence hues, photoactivation, and even the capability to sense biological events [289–291]. More details will be presented in section 3.1. Recently, a bacterial phytochrome-based photoswitch (BphP1–PpsR2 heterodimerization) for optogenetic regulation has been reported [292–294]. Encouragingly, *in vivo* application in intact mice was demonstrated [293]. One limitation of this photoswitch was the relatively low contrast (7-fold) [293], which suggests there is room for further improvement.

1.8 The scope of the thesis

Despite the enormous diversity of photosensory proteins currently available, optogenetic tools with new photosensory mechanism and favourable optical properties are required to further fuel the growth of this rapidly growing field. In this thesis, we present our work in developing a series of optogenetic actuators using a photocleavable FP variant, and our efforts to engineer a NIR fluorescent pH indicator derived from a bacterial phytochrome.

In Chapter 2, we describe our efforts to engineer a photocleavable protein (PhoCl) from a photoconvertible FP. The photocleavage of PhoCl was

thoroughly characterized *in vitro* using spectroscopy, mass spectrometry (MS) and gel filtration chromatography (GFC). We further demonstrated the utility of PhoCl as a photosensory domain to build optogenetics actuators that are functional in live cells. PhoCl was used to cage the activity of a POI by joining it with a subcellular localization tag or a genetically encoded inhibitor. The photocleavage could release the caging. This strategy was successfully applied to Gal4 transcription factor, Cre recombinase, and HCV protease. We also explored the usage of the light-activatable HCV protease to control a large pore ion channel, Panx1.

In Chapter 3, we focus on the development of a NIR fluorescent pH indicator, pH-mIFP. A pH insensitive monomeric NIR FP, mIFP, was converted to be pH sensitive by introducing point mutations around the BV chromophore. We also developed a bacterial colony-based high-throughput screening methods to evolve the initial pH-sensitive variant for improved brightness and pH sensitivity. The pH dependence of pH-mIFP was further characterized *in vitro* and on the surface of mammalian cells.

In Chapter 4, we provide a summary of this thesis and a brief discussion on the future directions regarding the development of PhoCl technology and pH-mIFP.

Chapter 2: Optogenetic control with a photocleavable protein, PhoCl

2.1 Introduction

Optogenetics is a burgeoning class of experimental techniques in which genetically encoded proteins, which change their activity upon absorption of light, are used for the spatial and temporal control of cell physiology [5]. The current repertoire of optogenetic tools can be subdivided into three categories: light-activated channels, pumps, GPCRs and enzymes, based on opsins (as described in section 1.2) [28,32,63]; proteins subject to light-dependent steric or allosteric control (as described in section 1.3.1.1, 1.3.3 and 1.5) [16,155]; and proteins that undergo light-dependent changes in oligomeric interactions (as described in section 1.3.1.2, 1.3.2, 1.4, 1.6.4 and 1.7) [87,122,228]. Despite the tremendous progress in development and application of these tools, the scope of physiological processes that can be optogenetically controlled remains limited.

Among photoreceptor proteins, FPs have some beneficial properties for optogenetics, such as strong fluorescence, robust heterologous expression, small and compact protein structure, and self-sufficient chromophore maturation [6,7]. However, FPs have been used predominantly as optogenetic reporters rather than actuators, due to the rigid β-barrel of FP that rarely undergoes pronounced conformational change in response to light. The only reported exception is the photoswitchable FP Dronpa, which changes its oligomerization tendency light-dependently and has been exploited to control protein activities [228,229].

To expand the scope of photosensory mechanisms and the usage of FPs, we introduce a fourth category of optogenetic actuator that is enabled by a photocleavable protein engineered from the green-to-red photoconvertible FP, mMaple [295]. The photoconversion reaction is a violet light (~400 nm) induced β-elimination reaction that extends the conjugated system of the chromophore with concomitant cleavage of the polypeptide backbone to form a ~66-residue N-terminal fragment and a ~166-residue C-terminal fragment that remain associated [216,217]. (**Figure 2.1a**). The extension of the conjugated system shifts the absorbance spectrum of mMaple to a longer wavelength region. (**Figure 2.1b**).

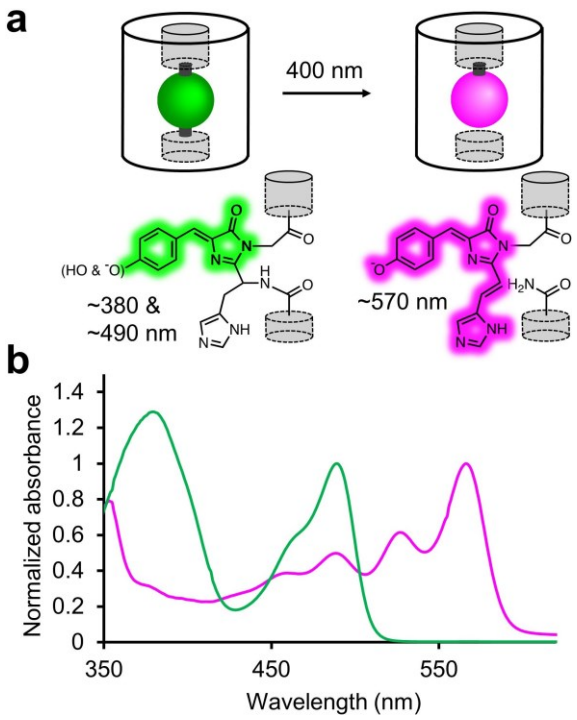

Figure 2.1. Photoconversion of mMaple. (**a**) mMaple photoconversion mechanism. Excitation of the protonated chromophore (~380 nm) leads to photoconversion and backbone cleavage. (**b**) Normalized absorbance spectra for mMaple before (green) and after (magenta) partial photoconversion.

Recognizing that mMaple [295], and its immediate progenitor mTFP1

[296], are highly tolerant of circular permutation [297,298], we envisioned engineering a topological variant of mMaple in which photoconversion would produce a small peptide fragment and a large "empty barrel" fragment that would spontaneously dissociate (**Figure 2.2**). As the chromophore is near the middle of a helical segment that runs through the middle of the protein, the positions that are closest to the chromophore and most likely to tolerate the introduction of new termini, are at either end of this segment [299]. We expected that the photocleavable variant could be used to manipulate protein localization or activity by using it as a protein linker to join a POI with a subcellular localization tag, or with a proteinaceous inhibitor. Upon illumination, the POI is released from the subcellular localization or its inhibitor, and is free to act.

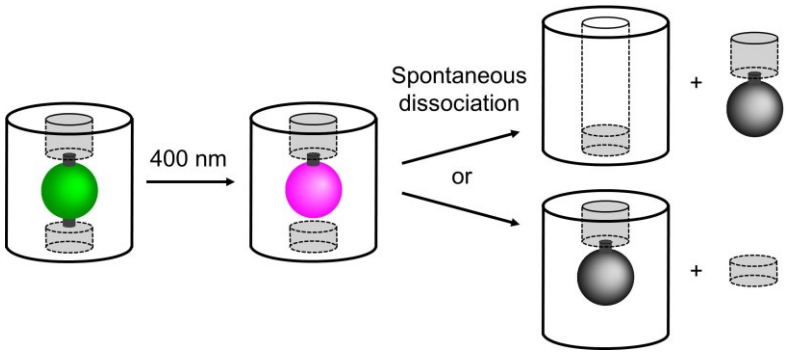

Figure 2.2. Schematic representation of the envisioned photocleavage.

2.2 Results and discussion

2.2.1 Circular permutation and directed evolution

To bring this design to fruition, we constructed six gene libraries (with 400 variants each) encoding circularly permutated mMaple variants with the original termini joined with a 5-residue linker, new termini either just before, or just after, the central segment, and randomized terminal residues. As shown in

Figure 2.3a,b, to construct these libraries, the gene encoding mMaple was circularly permuted at six surface exposed positions either N- or C-terminal to the central helix. For each permutation, the library was constructed by randomizing both the N-terminal residue (X) and the C-terminal residue (Y) to all 20 amino acid possibilities, to give a total of 400 possible variants. For circularly permuted variants, the residues are numbered as in mMaple (**Figure 2.5**) and the C-terminal residue (Y) is the residue that precede the N-terminal residue (X) in mMaple. For all locations, cleavage would produce one fragment of ~10-residues and one fragment of ~220-residues (**Figure 2.3b**)

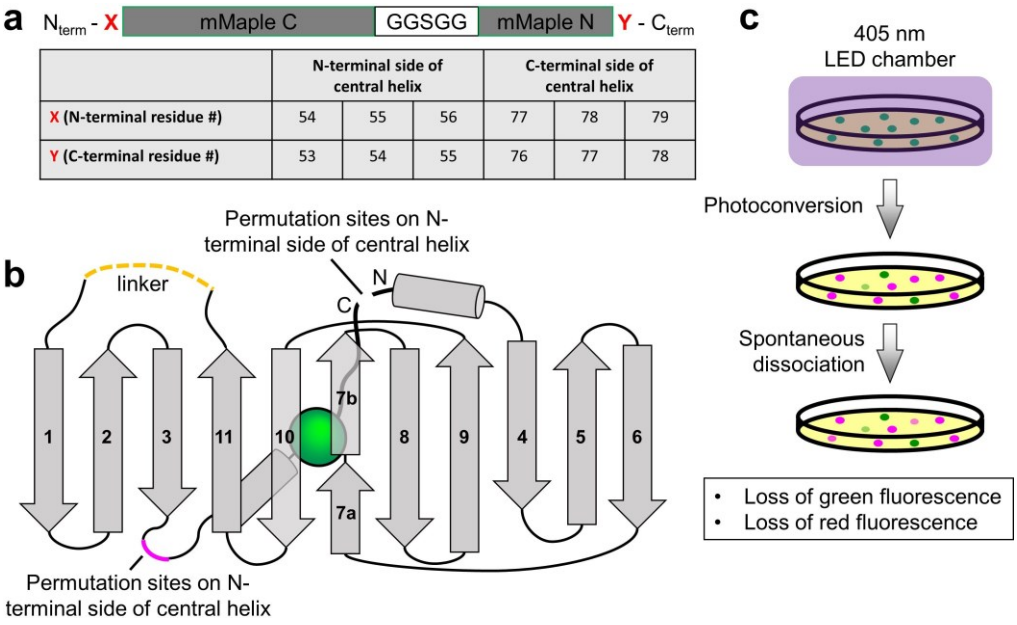

Figure 2.3. Strategy for design and screening of PhoCl variants. (**a**) Schematic of circular permutation libraries. (**b**) The two-dimensional topology representation of PhoCl (based on the structure of mTFP1 (PDB ID 2HQK) [296]), the permutation site is on the C-terminal side of the central helix. The yellow dashed line represents the GGSGG linker connecting the original N- and C-termini. Residues 53–56 are indicated in magenta. (**c**) Schematic of colony-based screening of libraries of PhoCl variants.

Using custom-built imaging and photoconversion systems [300], libraries were screened in colonies of *E. coli* (each expressing a library variant). As shown in **Figure 2.3c**, Petri dishes containing hundreds of colonies were imaged (for both green and red fluorescence), illuminated in a 405-nm light-emitting diode (LED) chamber at 0.15 mW/mm^2, imaged immediately after being removed from the chamber, and then imaged again after 10 min at room temperature. Expecting that the dissociation would result in the quenching of red fluorescence, we sought to identify variants that exhibited violet light-dependent green-to-red photoconversion followed by a rapid loss of red fluorescence in the dark.

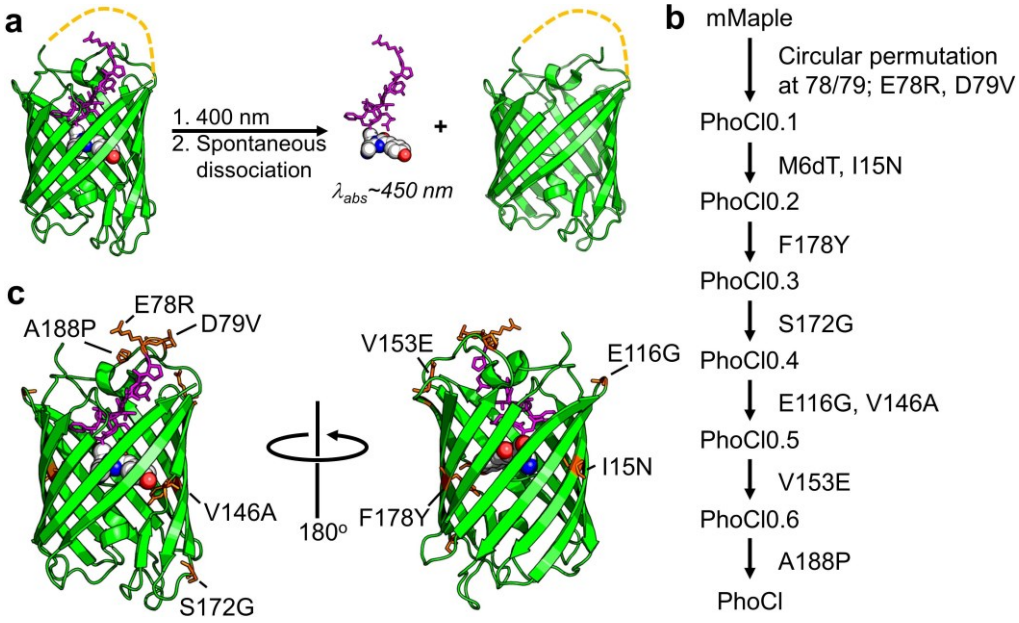

Figure 2.4. Representation of PhoCl structure and lineage of improved variants. (**a**) Structural representation of PhoCl dissociation modeled on the structure of mTFP1 (PDB ID 2HQK [296]). The small and large fragments are coloured magenta and green, respectively. (**b**) Lineage of improved PhoCl variants discovered during iterative cycles of library screening. (**c**) PhoCl mutations (orange) modeled on the structure of mTFP1 (PDB ID 2HQK [296]). Small and large fragments resulting from photocleavage are coloured magenta

and green, respectively. M6dT is not visible in the mTFP1 crystal structure and is therefore not represented here.

This approach led to a first generation photocleavable protein, designated PhoCl0.1, which lost red fluorescence with a half-life ($t_{1/2}$) of ~900 s, and had N-terminal residue Asp79Val and C-terminal residue Glu78Arg (**Figure 2.3b** and **2.4a,b**). As photocleavage occurred on the N-terminal side of the chromophore, and the permutation site was on the C-terminal side of the chromophore, the small peptide that dissociated from the larger fragment contained the chromophore and the fluorescence of the chromophore was quenched outside of the β-barrel (**Figure 2.4a**). The permutations at residues 53-56 led to photoconvertible proteins that did not spontaneously dissociate.

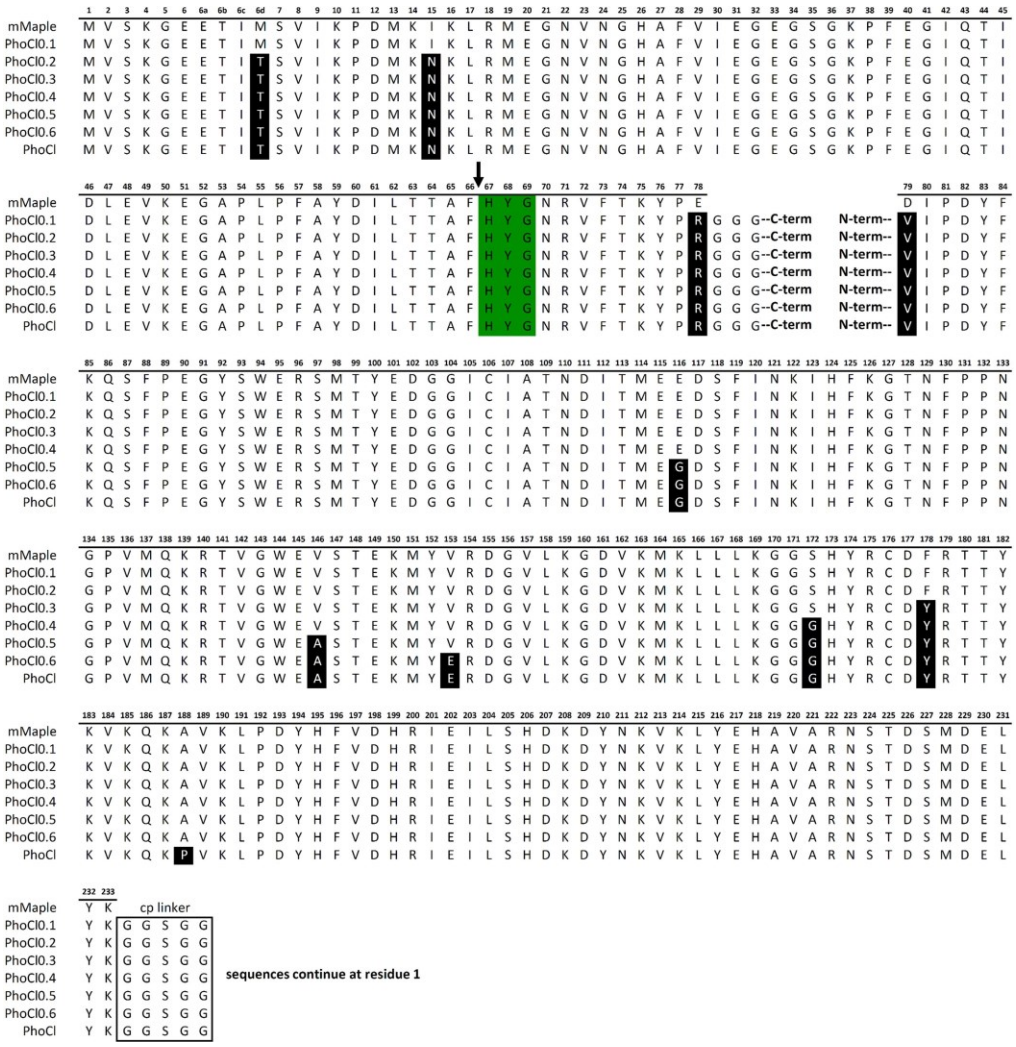

Figure 2.5. Sequence alignment of mMaple and PhoCl variants. Mutations relative to mMaple are represented as white text on a black background. The chromophore-forming residues are represented as black text on a green background. The circular permutation (cp) linker sequence is enclosed in a box. The site of photocleavage is indicated with an arrow.

To improve the properties of PhoCl0.1, we performed directed evolution for more efficient chromophore formation (brighter green fluorescence), more efficient photoconversion (more loss of green fluorescence), and faster peptide dissociation (more rapid loss of red fluorescence after photoconversion). Libraries were generated by error-prone polymerase chain reaction (PCR). This effort led to the discovery of PhoCl, which has 8 substitutions relative to

PhoCl0.1 (**Figure 2.4b,c** and **2.5**) and exhibits improved maturation, photoconversion, and rate of dissociation ($t_{1/2}$ of ~500 s, **Figure 2.6**).

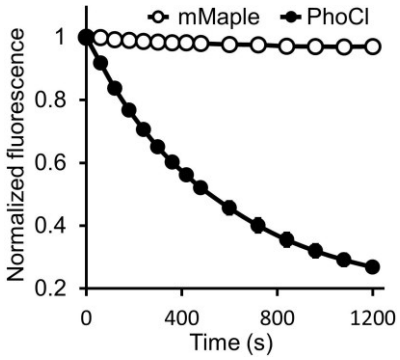

Figure 2.6. Kinetics of dissociation determined by loss of red fluorescence after photocleavage of mMaple and PhoCl. Values are means ± standard deviations (s.d.) (n = 3 independent experiments).

2.2.2 Protein characterization

Fluorescence spectroscopic characterization of purified PhoCl revealed that the initial state of PhoCl exhibits green fluorescence (**Figure 2.7a**) which is similar to that of the initial state of mMaple (**Figure 2.7b**). It also revealed that PhoCl loses its red fluorescence after photoconversion, however the photoconverted mMaple stays red fluorescent (**Figure 2.6** and **2.7b,c**). Furthermore, UV-vis spectroscopic characterization indicated that the photoconversion results in the transient formation of the red fluorescent form that spontaneously converts to a non-fluorescent species with a broad absorbance from ~400 to 500 nm (**Figure 2.7c**) that is similar to denatured mMaple (**Figure 2.7d**). This result is consistent with spontaneous dissociation to release a C-terminal peptide fragment with the chromophore at its N-terminus.

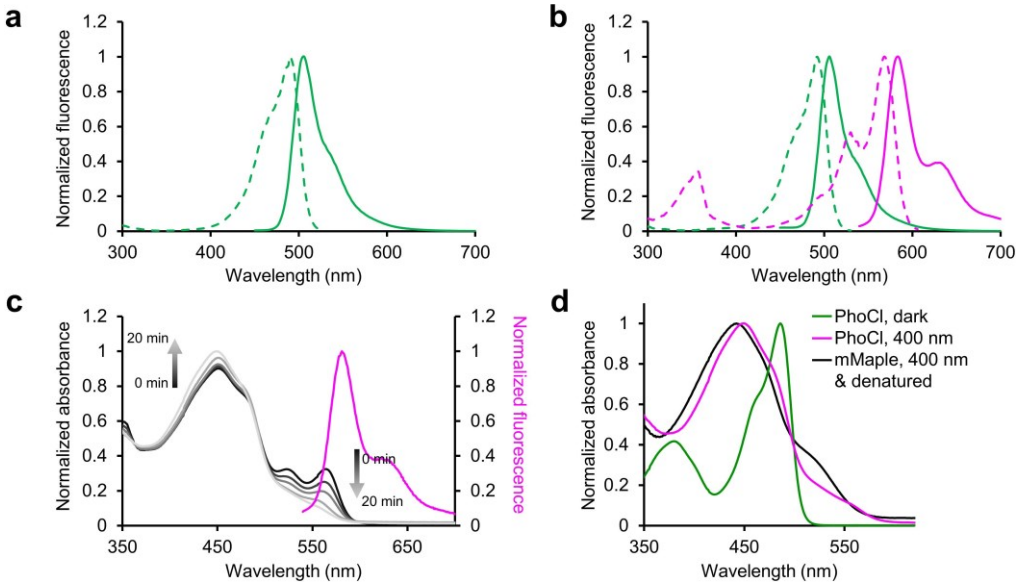

Figure 2.7. Absorbance and fluorescence spectra of mMaple and PhoCl. (**a**) Normalized fluorescence excitation (dashed line) and emission (solid line) spectra for the initial green state of PhoCl. (**b**) Normalized fluorescence excitation (dashed) and emission (solid) for the initial (green lines) and photoconverted (magenta lines) states of mMaple. (**c**) Normalized absorbance (black to gray lines) and fluorescence emission (magenta line) spectra for PhoCl post photoconversion. Fluorescence emission was acquired less than 30 s after a 5 min photoconversion in the 405-nm LED chamber. The "0 min" absorbance spectrum was acquired less than 10 s after photoconversion. Subsequent spectra were acquired 5, 10, 15, and 20 min later. Most of the protein had dissociated prior to the first measurement. (**d**) Normalized absorbance spectra for the initial (green line) state of PhoCl and the photoconverted state of PhoCl (magenta line) and mMaple (black line).

The photocleavage of PhoCl has also been analyzed by time-lapse electrospray ionization mass spectrometry (ESI-MS). As shown in **Figure 2.8a**, PhoCl was photoconverted in the 405-nm LED chamber (0.15 mW/mm^2) with a 2-min illumination starting at t = 0 s, and a 6-min illumination starting at t = 2015 s. ESI (electrospray ionization) mass spectra were acquired every 1 s for 30 min starting at t = 215 s, and for 10 min starting at t = 2500 s. The mass

spectra (**Figure 2.8b**) indicated that the photoconversion of PhoCl (molecular weight (MW): 31566 Da) produced a large fragment (MW: 29735 Da) and a small fragment (MW: 1830 Da). The MW of the large fragment and the small fragment are consistent with that of the empty barrel and the C-terminal chromophore-containing peptide, respectively. This result strongly supports our proposed mechanism of cleavage followed by dissociation.

The fraction of photocleavage was calculated as $EB/(EB + PhoCl) \times 100$, where *EB* and *PhoCl* are the sum of the peak heights for various corresponding ionization states. The rate of spontaneous dissociation determined by mass spectrometry (MS) ($t_{1/2}$ of ~250 s) (**Figure 2.8c**) is faster than that determined by loss of red florescence ($t_{1/2}$ of ~500 s) (**Figure 2.6**). The difference most likely is caused by the distinct buffer systems used in these two experiments.

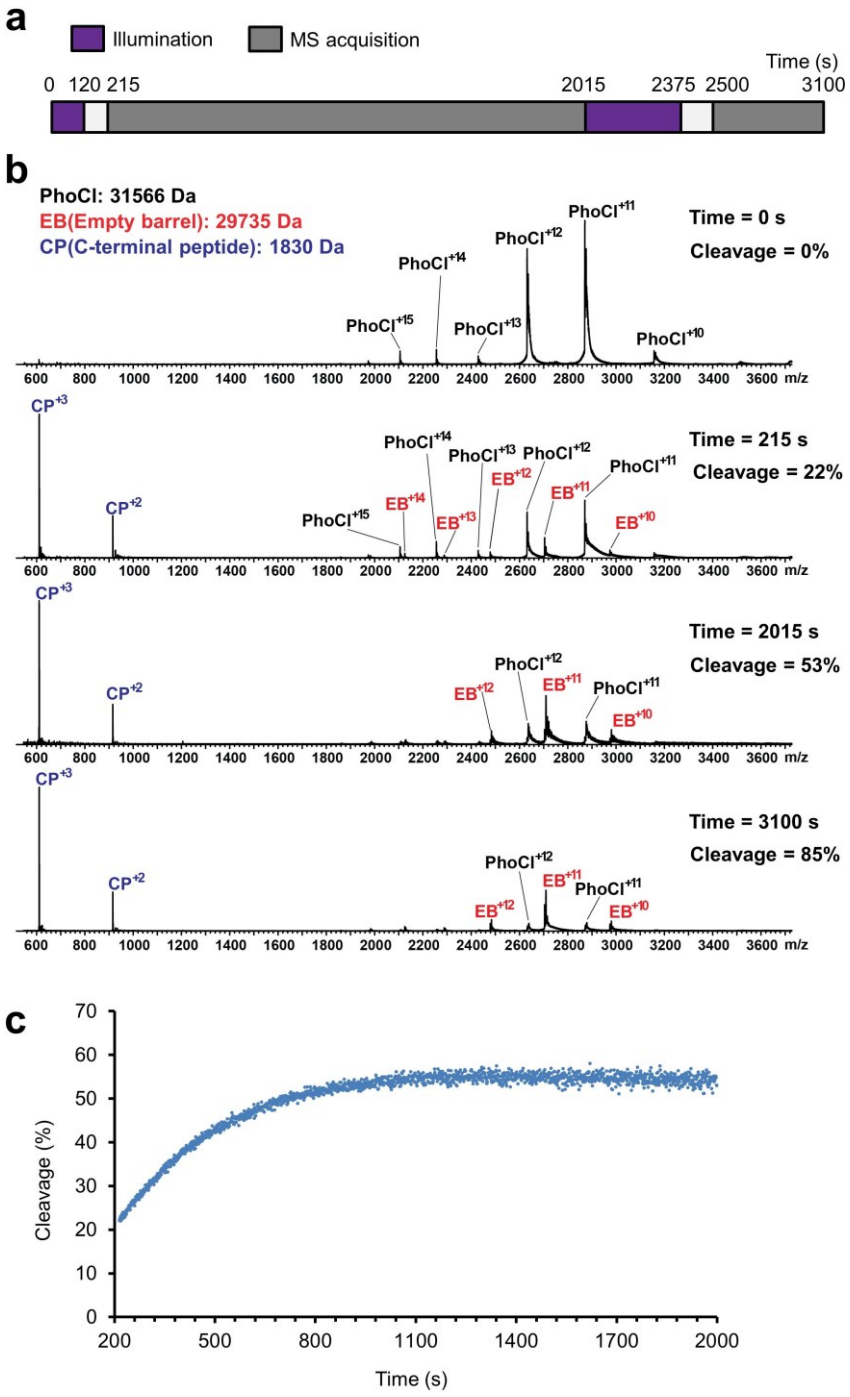

Figure 2.8. Demonstration of PhoCl photocleavage by mass spectrometry. (**a**) Schematic representation of illumination and ESI-MS data acquisition. (**b**) Representative ESI mass spectra of PhoCl acquired at t = 0 s (before photoconversion), 215 s, 2015 s and 3100 s. (**c**) Percent cleavage versus time, from t = 215 s to t = 2015 s.

To demonstrate the photocleavage of PhoCl as a fusion protein, we genetically fused maltose binding protein (MBP) to the C-terminus of PhoCl. The purified PhoCl-MBP was partially photoconverted in the 405-nm LED chamber (0.15 mW/mm^2) and tested by gel filtration chromatography (GFC) followed by sodium dodecyl sulfate polyacrylamide gel electrophoresis (SDS-PAGE) analysis of the GFC fractions.

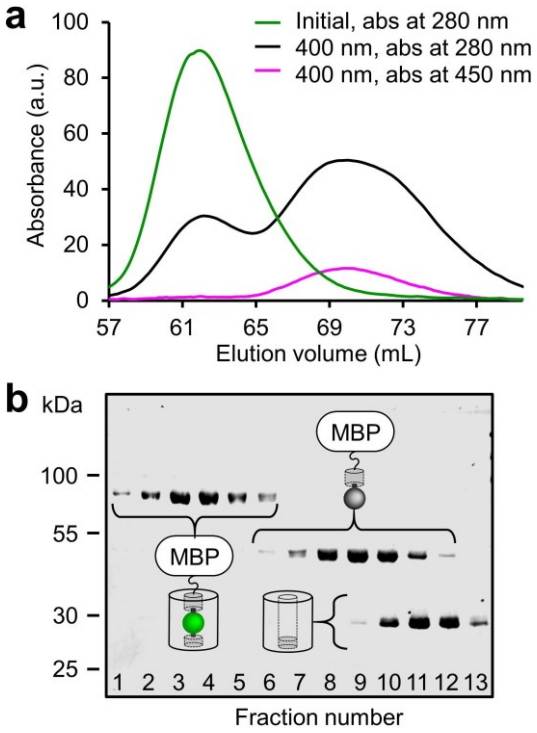

Figure 2.9. GFC and SDS-PAGE analysis of PhoCl-MBP. (**a**) Determination of the PhoCl-MBP photocleavage by GFC. Designated proteins were resolved on a HiLoad 16/60 Superdex 75pg gel filtration column. The absorbance at 280 nm and 450 nm were detected. (**b**) SDS-PAGE analysis of GFC fractions (13 × 1.5 mL; 57 – 77 mL elution volume).

Prior to photocleavage the chimeric PhoCl-MBP protein (75 kDa) eluted from a GFC column at an elution volume of ~62 mL. Partial photoconversion before analysis decreased the peak at ~62 mL and produced a broad peak at ~70 mL (**Figure 2.9a**). SDS-PAGE analysis of GFC fractions revealed that the ~70

mL peak was two overlapping peaks that corresponded to MBP-peptide fragment (45 kDa; absorbance at 450 nm due to quenched chromophore) and the empty PhoCl β-barrel (30 kDa) (**Figure 2.9a,b**).

To further demonstrate the photocleavage of mammalian cell-expressed PhoCl-fusion protein, we constructed a mammalian expression vector for PhoCl-mCherry-myc. At 48 hours post gene transfection, human embryonic kidney (HEK) 293 cells were exposed to 405-nm LED (0.15 mW/mm^2) for 0, 2, 4, 6, 8 mins. As determined by western blot, violet light induced a band shift from ~60 kDa (full length PhoCl-mCherry-myc) to ~30 kDa (mCherry-myc) indicating the cleavage of PhoCl (**Figure 2.10**).

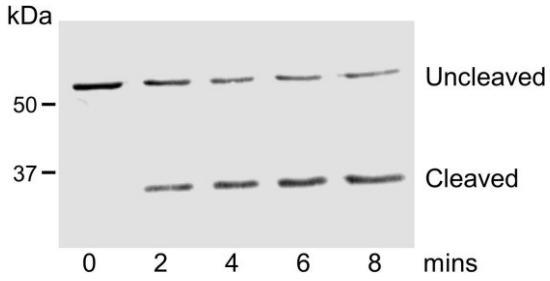

Figure 2.10. Western blot to assess the photocleavage of PhoCl-mCherry-myc expressed in HEK 293 cells. Cell lysates were separated by SDS-PAGE. Membranes were probed with an anti-myc primary antibody.

2.2.3 Optogenetic control of protein localization

To exploit PhoCl as an optogenetic tool, we first attempted to manipulate subcellular protein localization by optical detachment of a localization tag (i.e., a nuclear exclusion sequence (NES) and a nuclear localization sequence (NLS)) from a POI (**Figure 2.11a**). This approach proved successful, and redistribution of a red FP between the nucleus and the cytoplasm was achieved with NES-PhoCl-mCherry (**Figure 2.11b,c**) and NLS-PhoCl-mCherry (**Figure 2.11d,e**). The processes of photoconversion and protein redistribution were recorded and

analyzed by time-lapse fluorescent imaging (**Figure 2.12a,b,c,d,e,f**). The optogenetic manipulation of protein localization in a single cell was demonstrated using NLS-PhoCl-mCherry (**Figure 2.13a,b,c**). Similar results have also been obtained using NES-GFP-PhoCl-mCherry-NLS (**Figure 2.14a,b**) and ddFP reporters (**Figure 2.14c,d,e**).

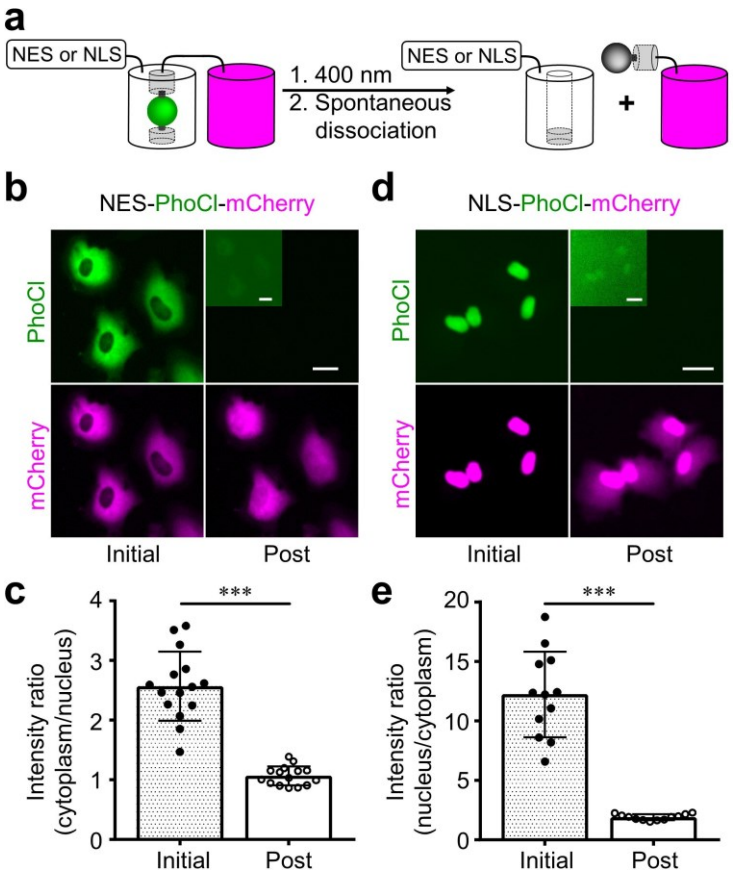

Figure 2.11. Optogenetic manipulation of protein localization with PhoCl. (**a**) Schematic of NES or NLS photocleavage. (**b**) HeLa cells expressing NES-PhoCl-mCherry, before and after (9 min) illumination with 5 s violet light pulses (390/40 nm, 4.89 mW/mm^2) every 15 s, for 6 min. Inset is the same image with 10× increased contrast. Scale bar, 20 μm. (**c**) Cytoplasm-to-nucleus intensity ratio for cells expressing NES-PhoCl-mCherry. Ratios were calculated for single cells (n = 15). Values are means ± s.d. $P = 4.0 \times 10^{-8}$ by unpaired Student's t-test (t (16.1) = 9.7). (**d**) HeLa cells expressing NLS-PhoCl-mCherry, treated and presented as in **b**. (**e**) Nucleus-to-cytoplasm intensity ratio for cells expressing NLS-PhoCl-mCherry (n = 12), presented as in **c**. $P = 7.4 \times 10^{-7}$ by

unpaired Student's t-test (t (11.1) = 9.9).

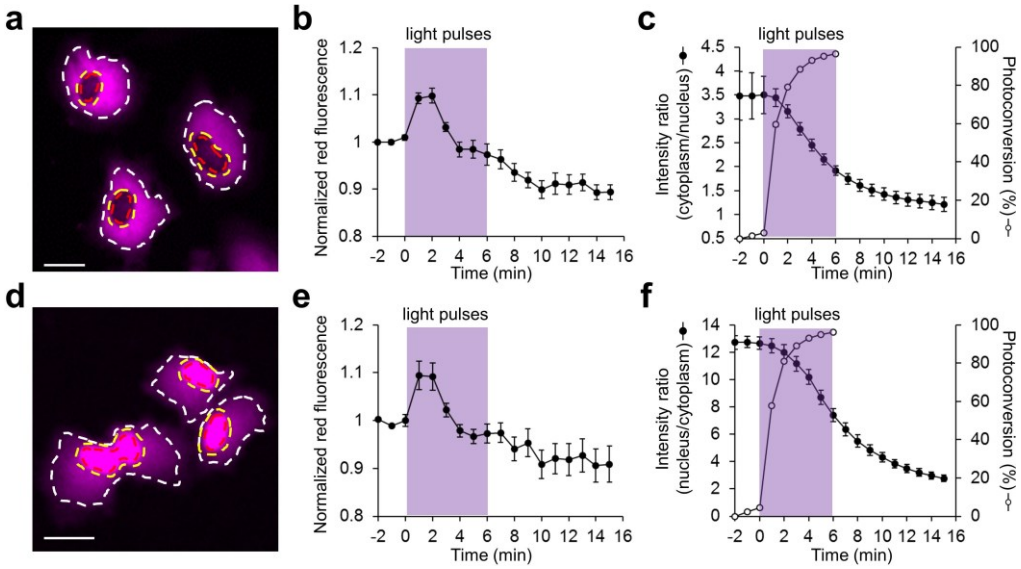

Figure 2.12. Time-lapse analysis for optogenetic manipulation of protein localization with PhoCl. (**a**) Representative fluorescence image of HeLa cells expressing NES-PhoCl-mCherry before photoconversion. Regions of interest used to quantify fluorescence intensity changes are indicated as follows: nucleus (region outlined in red), cytoplasm (region outlined in white minus region outlined in yellow), and the whole cell (region outlined in white). Scale bar, 20 μm. (**b**) Normalized and averaged whole cell red fluorescence intensity versus time for the cells in **a**. Light pulses (390/40 nm, 4.89 mW/mm^2) are 5 s in duration, every 15 s for 6 min (purple interval). Values are means ± s.d. (n = 3). (**c**) Photoconversion of PhoCl (quantified by the loss of whole cell green fluorescence) and red fluorescence intensity localization ratio (cytoplasm to nucleus) versus time, for the cells in **a**. Illumination conditions are as described in **b**. Values are means ± s.d. (n = 3). (**d**) Representative fluorescence image of HeLa cells expressing NLS-PhoCl-mCherry before photoconversion. Regions of interest are defined as in **a**. Scale bar, 20 μm. (**e**) Normalized and averaged whole cell red fluorescence intensity versus time for the cells in **d**. Illumination conditions are as described in **b**. Values are means ± s.d. (n = 3). (**f**) Photoconversion of PhoCl (quantified by the loss of whole cell green fluorescence) and red fluorescence intensity localization ratio (nucleus to cytoplasm) versus time, for the cells in **d**. Illumination conditions are as

described in **b**. Values are means ± s.d. (n = 3).

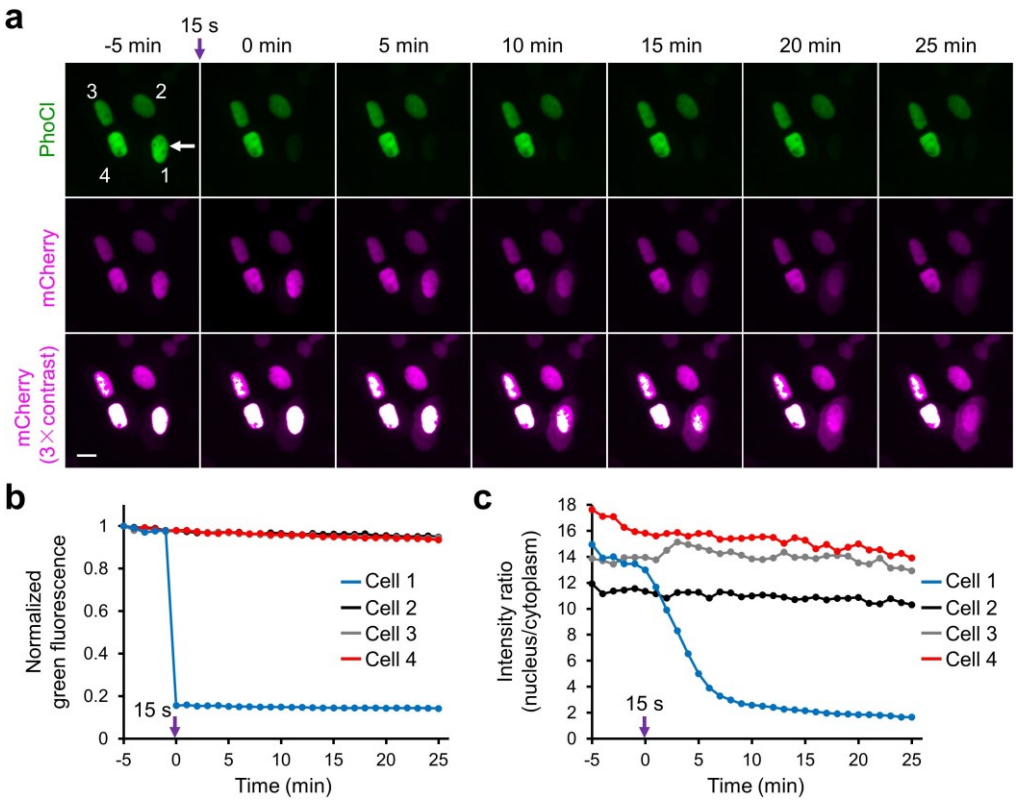

Figure 2.13. Optogenetic manipulation of protein localization in a single cell. (**a**) Time-lapse images of HeLa cells expressing NLS-PhoCl-mCherry before and after 15 s illumination of cell 1 (arrow) with a 405-nm laser (0.12 mW). Saturated pixels in the mCherry channel with 3-fold increased contrast are shown in white. Scale bar, 20 μm. (**b**) Normalized whole cell green fluorescence intensity versus time for the cells in **a**. (**c**) Red fluorescence localization ratio (nucleus intensity to cytoplasm intensity) versus time, for the cells in **a**.

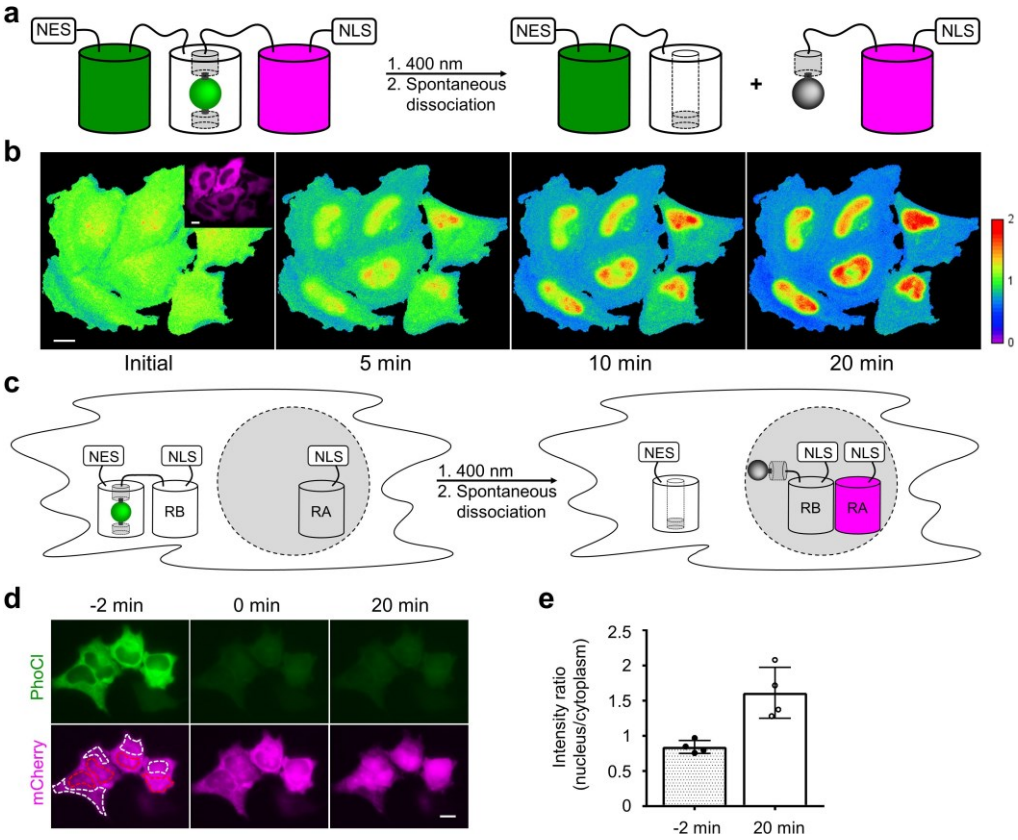

Figure 2.14. Optogenetic redistribution of the N- and C-terminal portions of NES-GFP-PhoCl-mCherry-NLS following photocleavage and *in situ* demonstration of PhoCl photocleavage using ddFPs. (**a**) GFP with a NES and mCherry with an NLS were genetically fused to the N- and C-termini, respectively, of PhoCl. Upon photocleavage the two FPs are released from each other and the GFP is now excluded from the nucleus, while the red FP is sequestered in the nucleus. (**b**) Ratiometric images (red/green) of HeLa cells expressing the construct described in a before and after illumination with ~400-nm light. Before illumination with 400-nm light, the protein is largely excluded from the nucleus (inset of leftmost image) but the ratio of red to green fluorescence is generally consistent throughout the nucleus and cytoplasm. After photocleavage the ratio of red to green fluorescence decreases in the cytoplasm and increases in the nucleus. Scale bar, 15 µm. (**c**) Demonstration of PhoCl photocleavage in live cells using ddFP technology [251,252]. "RA" is a dimly fluorescent red FP that becomes brighter upon heterodimerization with its non-fluorescent homolog "RB". As with NES-GFP-PhoCl-mCherry-NLS in **b**, the NES-PhoCl-RB-NLS construct is initially excluded from the nucleus. Upon photocleavage, the RB-NLS portion is separated from the NES and

translocates to the nucleus where it heterodimerizes with RA, causing an increase in red fluorescence. (**d**) Green and red fluorescence images of cells expressing the constructs described in c before and after illumination with ~400-nm light. Within 20 min of illumination, the red fluorescence in the nucleus is observed to increase due to translocation and interaction of RA with RB. Regions of interest used to quantify fluorescence intensity changes are indicated as follows: nucleus (outlined in red) and cytoplasm (outlined in white). Scale bar, 20 μm. (**e**) Nucleus-to-cytoplasm intensity ratio for cells in **d**. Values are means ± s.d. (n = 4 cells).

2.2.4 Optogenetic control of gene expression

We next attempted to achieve optogenetic control of gene expression by using PhoCl photocleavage to release a Gal4-VP16 transcription factor [301] that was initially excluded from the nucleus due to genetic fusion with the plasma-membrane associated β-2 adrenergic receptor (β2AR) [302] (**Figure 2.15a**). However, this strategy gave high levels of background transcriptional activation (**Figure 2.15b,c**).

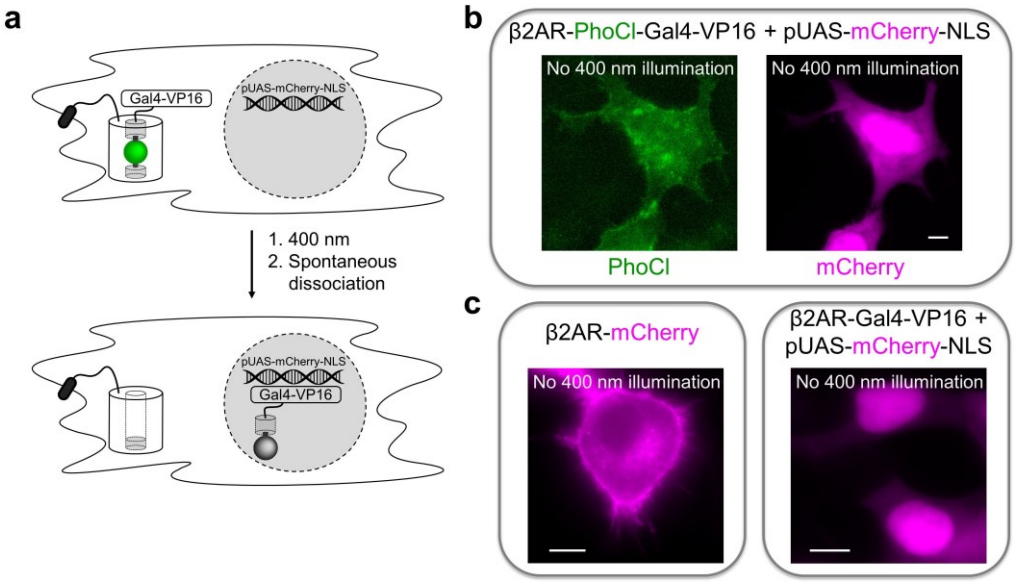

Figure 2.15. Optogenetic release of membrane-tethered Gal4 transcription factor to induce gene expression. (**a**) Schematic representation of activation mechanism. PhoCl was genetically inserted between the Gal4-VP16

transcription factor [301], with or without an NLS, and the plasma-membrane associated β2AR [302]. The resulting plasmid (β2AR-PhoCl-Gal4-VP16), together with a reporter plasmid encoding mCherry-NLS under control of a repeated upstream activator sequence (UAS) [303], was used to cotransfect mammalian cells. Photocleavage would allow Gal4-VP16 to translocate to the nucleus, bind to the UAS promoter, and activate gene expression. (**b**) Green (PhoCl) and red (mCherry) fluorescence images of a HeLa cell that has been transfected with the genes encoding β2AR-PhoCl-Gal4-VP16 and pUAS-mCherry-NLS, and has not been illuminated with 400-nm light. The strong mCherry-NLS expression in the absence of illumination reveals a high level of transcription even though β2AR-PhoCl-Gal4-VP16 does appear to be membrane localized and excluded from the nucleus. Scale bar, 20 μm. (**c**) Red fluorescence images of HeLa cells expressing β2AR-mCherry (left image) and both β2AR-Gal4-VP16 and pUAS-mCherry-NLS (right image), and not illuminated with 400-nm light. These control experiments confirm the membrane localization of β2AR and that mCherry-NLS expression occurs even with a membrane tethered Gal4-VP16 construct that does not contain PhoCl. Scale bars, 20 μm.

We turned to the well-established approach of POI inactivation (or "caging") by fusion to steroid receptor (SR) domains [304]. POI inactivation likely involves interaction of the SR with heat shock protein 90 (Hsp90), leading to steric blocking, partial unfolding, and cytoplasmic confinement of the POI [305]. Typically, treatment with a steroid is used to release Hsp90 and activate the POI. To test whether PhoCl could be used to uncage a POI by photocleavage of Hsp90-SR (**Figure 2.16a**), we co-expressed SR-PhoCl-Gal4-VP16-PhoCl-SR with either a UAS-NanoLuc or a UAS-mCherry-NLS reporter. Fusion to two SR domains gives lower background activity than fusion to one SR domain [306]. Violet light illumination led to a 57 ± 2-fold induction of mCherry-NLS expression (**Figure 2.16b** and **2.17a**) and a 52 ± 2-fold induction of NanoLuc

activity (**Figure 2.16c** and **2.17b**). The SR-fusion strategy also enabled optogenetic activation of Cre recombinase (**Figure 2.16d**) as quantified by flow cytometry (**Figure 2.16e** and **2.18**). The use of high energy violet light to elicit photocleavage can be circumvented by using primed conversion [307] with lower energy 458-nm and 730-nm light (**Figure 2.19a,b,c,d**).

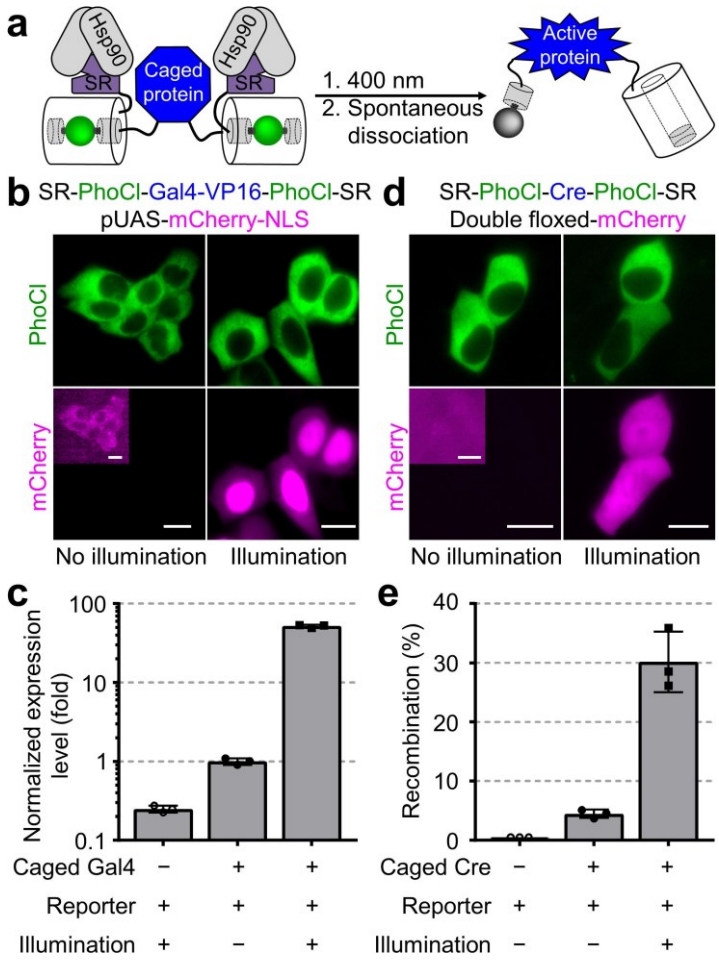

Figure 2.16. Optogenetic manipulation of gene expression with PhoCl. (**a**) Schematic of protein activation using PhoCl and fused SR domains. (**b**) HEK 293 cells expressing SR-PhoCl-Gal4-VP16-PhoCl-SR and containing a UAS-mCherry-NLS reporter gene. Images were acquired 24 hours post illumination (2 min of 405 nm at 0.15 mW/mm^2, repeated at 24, 25, and 26 h post transfection). Scale bar, 20 μm. (**c**) Normalized NanoLuc luminescence for cell lysates 12 hours after being illuminated as in **b**. Values are means ± s.d. (n = 3 cell cultures). (**d**) HEK 293 stable cell line containing the inverted gene encoding mCherry flanked by *loxP* sites (floxed) and transiently transfected

with the gene encoding SR-PhoCl-Cre-PhoCl-SR (illumination as in **b**). Scale bar, 20 μm. (**e**) Cre-dependent recombination rates for mCherry-positive cells by flow cytometry 24 hours post illumination. Values are means ± s.d. (n = 3 cell cultures).

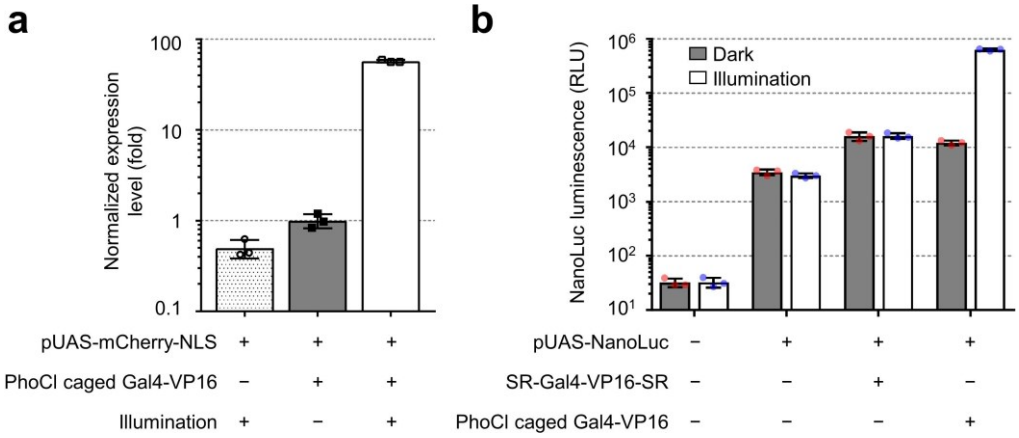

Figure 2.17. Quantification of optogenetically activatable Gal4-VP16. (**a**) Quantification of light-activated gene expression with SR-PhoCl-Gal4-VP16-PhoCl-SR and an mCherry reporter. Cells were transiently transfected with the constructs indicated, illuminated as in **Figure 2.16b**, and then analyzed 24 hours after illumination. Values are means ± s.d. (n = 3 cell cultures). (**b**) Quantification of light-activated gene expression with SR-PhoCl-Gal4-VP16-PhoCl-SR and a NanoLuc reporter. Cells were transiently transfected with the constructs indicated, illuminated as in **Figure 2.16b**, analyzed 12 hours after illumination. Values are means ± s.d. (n = 3 cell cultures).

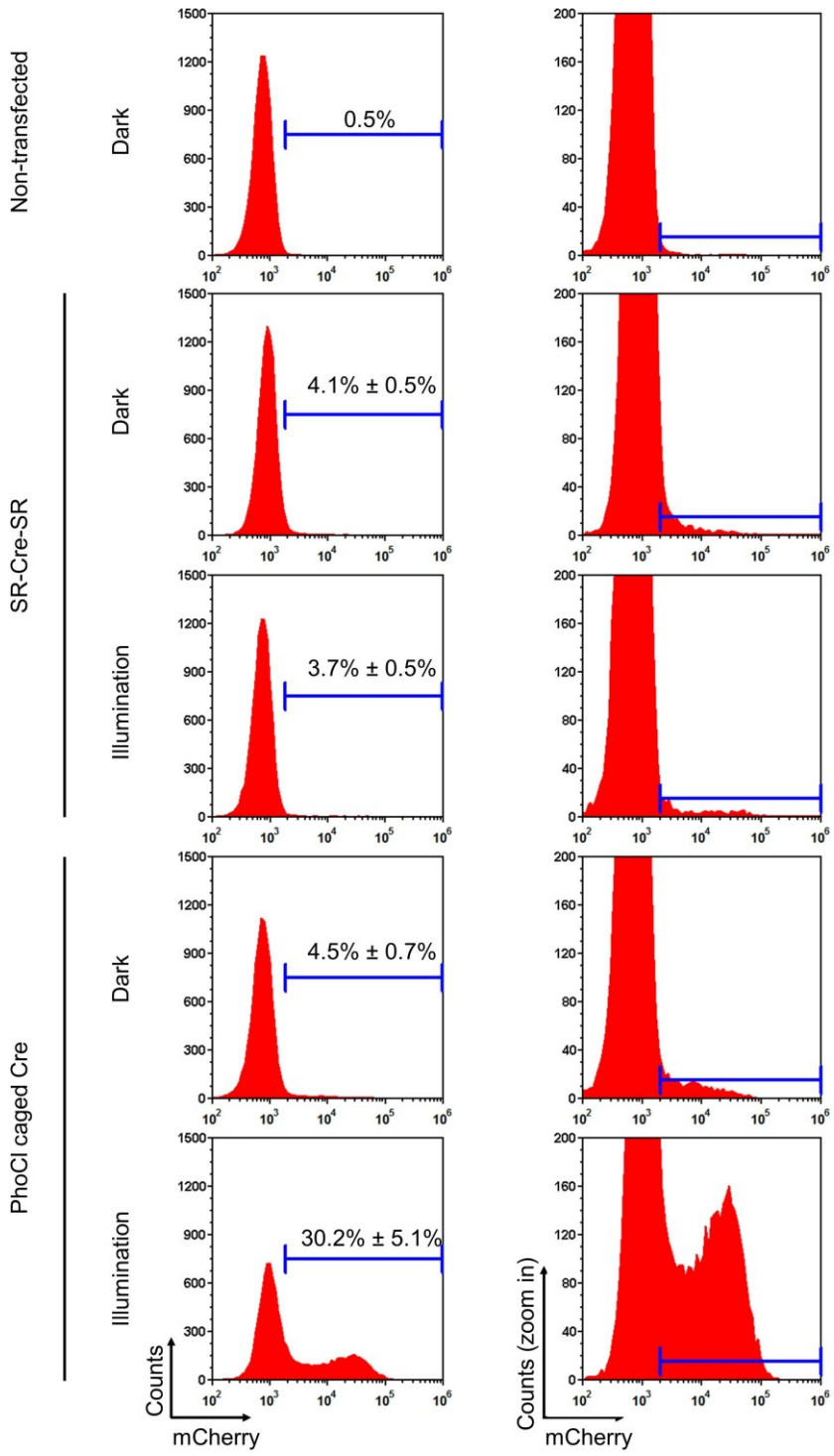

Figure 2.18. Flow cytometry analysis to assess optogenetic activation of Cre recombinase. Representative histograms show distribution of mCherry fluorescence intensity in a HEK 293 stable cell line (containing a floxed inverted mCherry reporter gene) that has been transiently transfected with the constructs indicated, with and without illumination (as in **Figure 2.16b**). The range of intensities considered to be mCherry-positive cells is indicated with a

blue line. Values are means ± s.d. (n = 3 cell cultures). Histograms with the Y-axis (counts) zoomed in are presented in the right column.

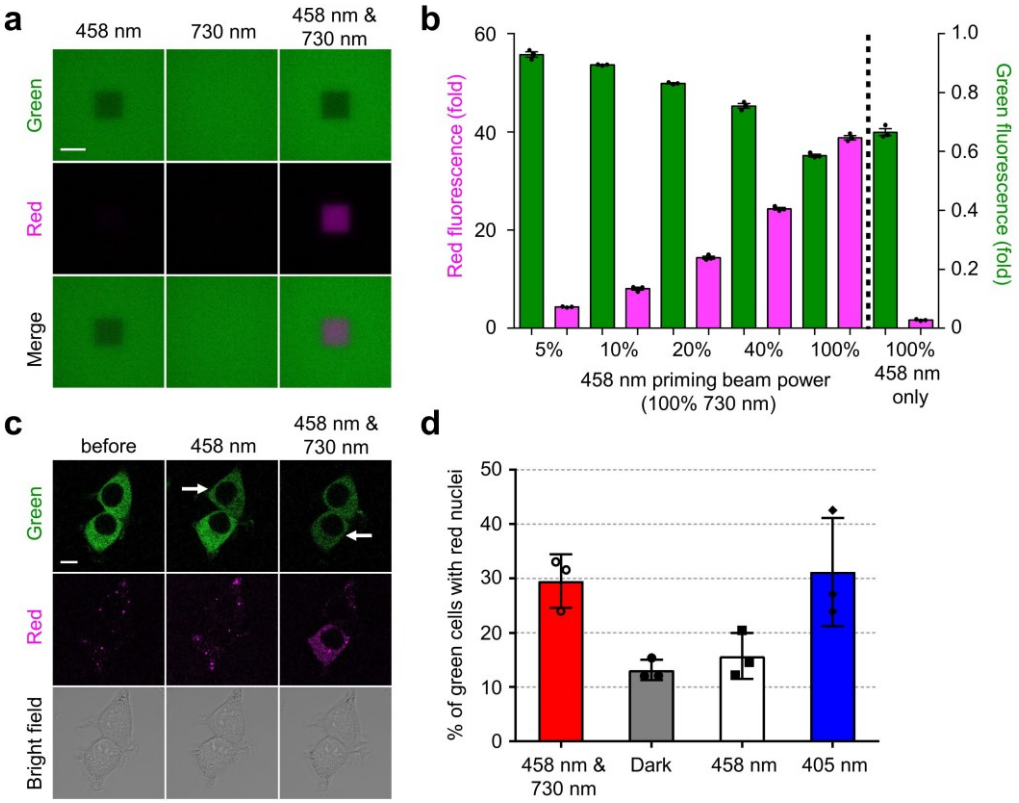

Figure 2.19. Primed conversion *in vitro* and in live cells. (**a**) Primed conversion [308,309] of PhoCl-MBP embedded in a polyacrylamide gel. Green and red PhoCl fluorescence signal after attempted 458-nm photoconversion (left), 730-nm photoconversion (center), and primed conversion using 458-nm and 730-nm laser beams (right). Merged channels are shown on the bottom row. Laser powers were both set to 100%. Scale bar, 50 µm. (**b**) Change in green (green bars) and red (magenta bars) fluorescence intensity of PhoCl-MBP upon primed conversion using a 458-nm priming beam at varying laser powers and constant 100% 730-nm laser. Values are means ± s.d. (n = 3). (**c**) Fluorescence microscopy images of HEK 293T cells co-transfected with SR-PhoCl-Gal4-VP16-PhoCl-SR and pUAS-mCherry-NLS. Before illumination (left), after 458-nm laser only illumination on upper cell (center), and primed conversion on the lower cell (right). Scale bar, 10 µm. (**d**) Quantification of red nuclei over total number of green cells treated as in **c**. Cells were either subjected to primed conversion using 458-nm plus 730-nm beams (red bar), kept in dark (grey bar), illuminated with only 458-nm beam (white bar), or illuminated with 405-nm

beam (blue bar). Values are means ± s.d. (n = 3).

2.2.5 Optogenetic control of HCV protease

PhoCl could enable a generic approach for optogenetic activation of enzymes if used as a photocleavable linker between an enzyme and its proteinaceous inhibitor. In such constructs, the enzyme function would be nullified or "caged" prior to inhibitor release by photocleavage. Following this design strategy, we proposed to develop a photoactivatable HCV NS3/4A protease (HCVp) by inserting PhoCl between HCVp and an inhibitory peptide (I) [310] (**Figure 2.20a,b**).

To develop a photoactivatable HCVp we sought to identify an inhibitory peptide (I) that would provide a high level of intramolecular inhibition in the context of an intact I-PhoCl-HCVp fusion and a low level of intermolecular inhibition at a stoichiometric concentration following photocleavage. To assay HCVp activity in live cells, we used a membrane tethered red FP composed of mCherry linked to a C-terminal protein prenylation motif (CAAX box) via a consensus substrate (4A/4B) for HCVp (mCherry-4A/4B-CAAX) (**Figure 2.21a**). To determine if a stoichiometric concentration of a particular peptide inhibitor would be sufficient to fully inhibit HCVp in live cells, we incorporated peptide inhibitors into an I-p2A-HCVp construct, where p2A is a self-cleaving peptide sequence (**Figure 20a,c**). We explored the use of five peptide inhibitors with inhibitory constant (K_i) values ranging from 0.5 – 100 nM (**Figure 20d**). Fluorescence imaging of cells contransfected with each of the five I-p2A-HCVp constructs and mCherry-4A/4B-CAAX revealed that the red fluorescence was entirely cytoplasmic in all cases (**Figure 20e, top row**), indicating that HCVp retained activity in the presence of a stoichiometric concentration of even the

highest affinity (K_i = 0.53 nM) inhibitor. Fluorescence imaging of cells contransfected with each of the five I-PhoCl-HCVp constructs and mCherry-4A/4B-CAAX (no violet light illumination) revealed that the red fluorescence was entirely cytoplasmic for the lowest affinity inhibitor (K_i = 105 nM), partially membrane localized for the second lowest affinity (K_i = 57 nM) inhibitor, and entirely membrane localized for the three highest affinity inhibitors (K_i = 0.5 – 10.5 nM) (**Figure 20e, bottom row**). Rationalizing that a higher K_i would allow higher levels of HCVp activity following photocleavage, we employed the I-PhoCl-HCVp construct containing the K_i = 10.5 nM inhibitor (CP5-46A-4D5E) for all other experiments.

To demonstrate the utility of the I-PhoCl-HCVp construct, we co-expressed it with a red FP that was tethered to the membrane with an HCVp substrate-containing linker (**Figure 2.21a**). Consistent with negligible activity in the "off" state, red fluorescence was initially membrane localized even in cells expressing high concentrations of I-PhoCl-HCVp (**Figure 2.21b,c**). Photoinduced dissociation of Dronpa FP oligomers (fluorescent light-inducible protein (FLIP) system) has been used for photoactivation of HCVp, but this approach was limited by substantial activity in the "off" state. Following optogenetic uncaging, red fluorescence was observed to decrease at the membrane and increase in the cytoplasm (over approximately 1 h) as the red FP was proteolytically released. A variety of protease activatable (or inactivatable) proteins have previously been engineered (**Table 2.1**), so I-PhoCl-HCVp expands the range of cellular functions that can be optogenetically manipulated.

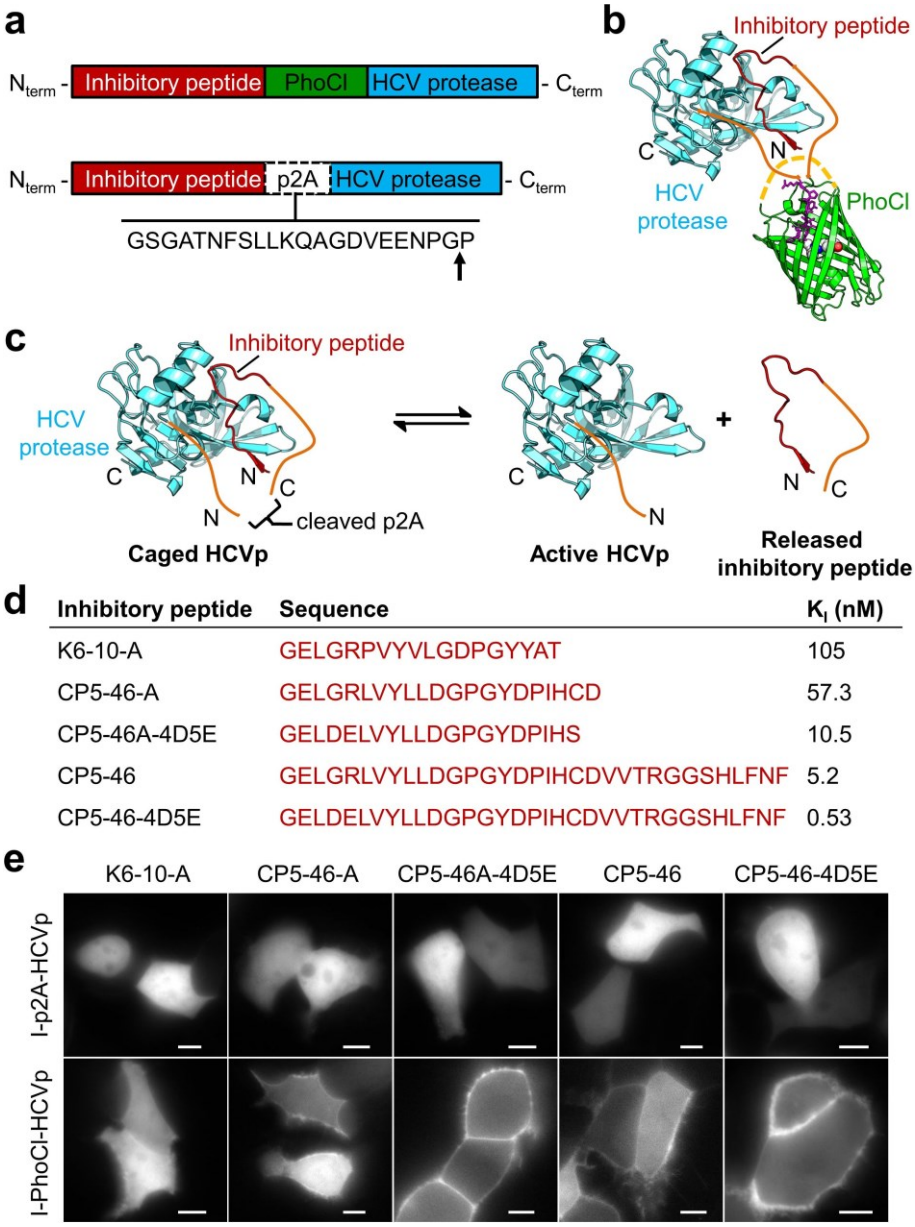

Inhibitory peptide	Sequence	K_i (nM)
K6-10-A	GELGRPVYVLGDPGYYAT	105
CP5-46-A	GELGRLVYLLDGPGYDPIHCD	57.3
CP5-46A-4D5E	GELDELVYLLDGPGYDPIHS	10.5
CP5-46	GELGRLVYLLDGPGYDPIHCDVVTRGGSHLFNF	5.2
CP5-46-4D5E	GELDELVYLLDGPGYDPIHCDVVTRGGSHLFNF	0.53

Figure 2.20. Identification of an optimal inhibitory peptide (I) for I-PhoCl-HCVp. (**a**) Schematic of I-PhoCl-HCVp and I-p2A-HCVp constructs. (**b**) Structural representation of I-PhoCl-HCVp. HCVp (cyan) in represented in complex with the inhibitory peptide CP5-46A-4D5E (red) (PDB ID 4A1V [310]), and PhoCl (green) is represented using the structure of mTFP1 (PDB ID 2HQK [296]). (**c**) Structural representation of I-p2A-HCVp, where p2A is a self-cleaving peptide. (**d**) Amino acid sequences of five peptide inhibitors, with K_i values ranging from 0.5 to 100 nM [311]. (**e**) Representative fluorescence microscopy images (mCherry channel) of HEK 293 cells co-expressing I-p2A-HCVp plus mCherry-4A/4B-CAAX (top row) or I-PhoCl-HCVp plus mCherry-4A/4B-CAAX (bottom row). None of the cells are illuminated with 400 nm

light to induce photocleavage. In each column, I is the same for both I-p2A-HCVp and I-PhoCl-HCVp, and corresponds to one of the sequences provided in **c**. Scale bars, 10 µm.

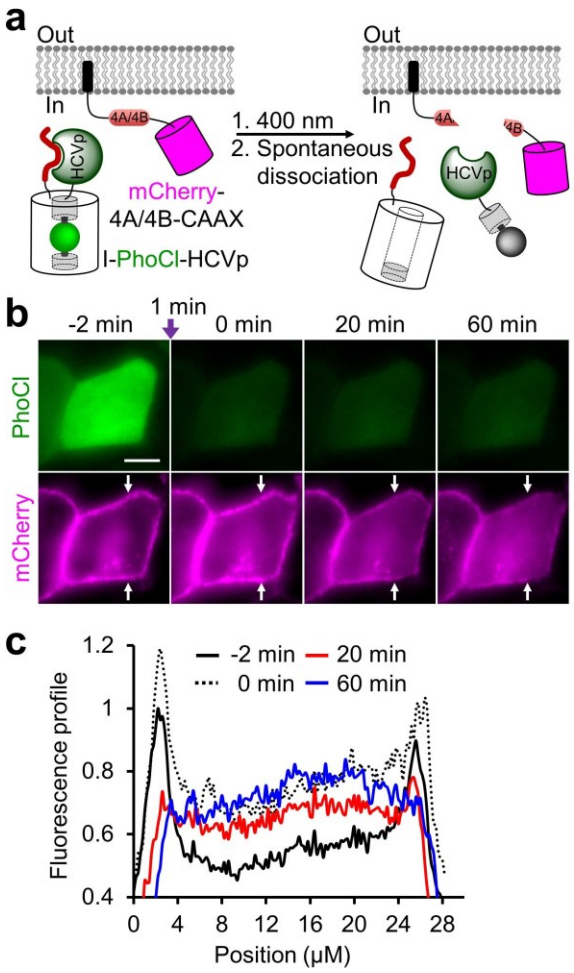

Figure 2.21. Optogenetic activation of HCV protease. (**a**) Schematic of using I-PhoCl-HCVp to release membrane-tethered mCherry. (**b**) A HeLa cell expressing mCherry-4A/4B-CAAX and I-PhoCl-HCVp. Cells were illuminated 1 min with 390/40 nm at 7.23 mW/mm^2. Scale bar, 10 µm. (**c**) Red fluorescence intensity profiles between white arrows in **b**.

Table 2.1.

Selected previously reported examples of engineered protease-sensitive proteins.

Protease-sensitive protein	Protease	Effect	Ref.
Pannexin-1	Tobacco etch virus (TEV) protease	Activation	[312]
Rec8 and Scc1 α-kleisin proteins	TEV protease	Inactivation	[313]
caspase-3, caspase-6, and caspase-7	TEV protease	Activation	[314]
Membrane tethered (MT) Gal4-VP16, MT luciferase, Gal4-VP16 fused to steroid receptor (SR), and luciferase-SR	Split TEV protease	Activation	[315]
diphtheria toxin A and Ricin A chain	HCV NS3 protease	Activation	[316]

2.2.6 Opto-Panx1

To demonstrate that I-PhoCl-HCVp could enable optogenetic activation of a protease activatable protein, we used it to develop an optogenetically-activated Pannexin-1 (Opto-Panx1). Panx1 is a large pore ion channel that is opened by proteolytic truncation of the C-terminal tail and serves to regulate cellular processes that include ATP release, phagocyte chemotaxis, inflammasome assembly, and neuronal excitotoxicity [312,317]. Ascribing specific effects to Panx1 has proven difficult due to the lack of highly specific pharmacological antagonists and the potential for compensation by other Panx isoforms [318]. Opto-Panx1 is the combination of I-PhoCl-HCVp and an engineered HCVp-activatable Panx1 ($Panx1^{HCV}$) in which the caspase cleavage site of Panx1 C-terminal tail is converted to an HCVp substrate (**Figure 2.22a,b**). Illumination of N2a cells expressing Opto-Panx1 (**Figure 2.22c**)

resulted in cleavage of the C-terminal tail (**Figure 2.22d,e**) and uptake of the TO-PRO-3 dye [319] (**Figure 2.23a,b,c**). Opto-Panx1 activation induced ATP release (**Figure 2.24a**) and increased whole cell currents (**Figure 2.24b,c,d,e,f**) in HEK 293T cells. Chronic photoactivation induced cell blebbing, consistent with the reported activity of Panx1 in ischemic neurons [320] (**Figure 2.25a,b,c**). By providing exquisite spatiotemporal control of Panx1 activation, Opto-Panx1 should enable investigations of the isoform-specific contribution of this channel.

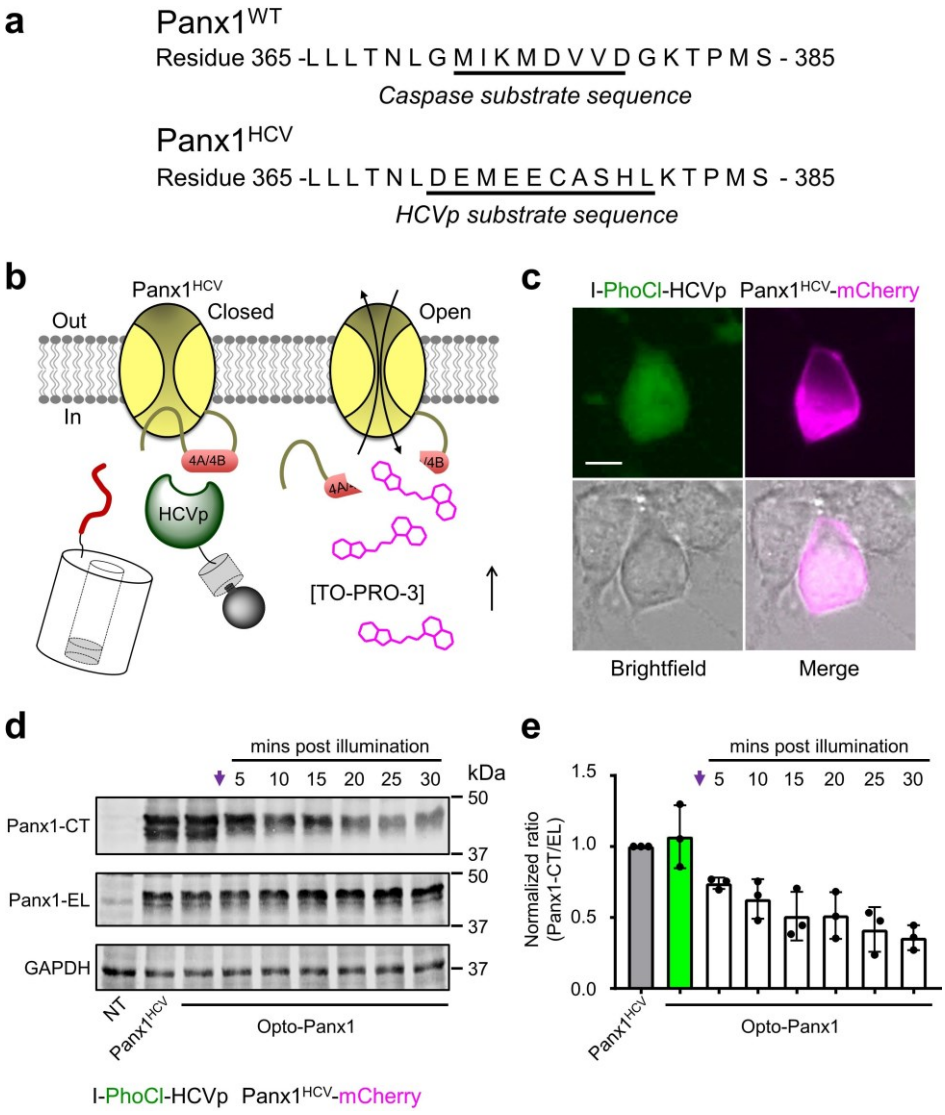

Figure 2.22. Engineering of Opto-Panx1 and validation by western blot. (**a**) Engineering of Panx1^{HCV}. Partial amino acid sequence showing the caspase-

3 substrate sequence within Panx1^{WT} [312]. This sequence was substituted with an HCVp substrate sequence to make Panx1^{HCV}. (**b**) Schematic of Opto-Panx1 (I-PhoCl-HCVp with Panx1^{HCV}). (**c**) Expression of Opto-Panx1 (I-PhoCl-HCVp and Panx1^{HCV}-mCherry) in N2a cells. Scale bar, 10 µm. (**d**) Representative western blot showing Opto-Panx1 C-tail cleavage upon violet light stimulation (405 nm, 0.15 mW/mm^2). Panx1-EL denotes a primary antibody against the first extracellular domain of Panx1 (total Panx1). Panx1-CT denotes a primary antibody directed against an epitope distal to the HCVp site in the C-terminal domain of Panx1^{HCV} (uncleaved Panx1). NT = non-transfected, Panx1^{HCV} = Panx1^{HCV} only, Opto-Panx1 = I-PhoCl-HCVp and Panx1^{HCV}. (**e**) Quantification of band density ratio (uncleaved Panx1 to total Panx1) in **d** normalized to the ratio for cells expressing Panx1^{HCV} only. Values are means ± s.d. (n = 3).

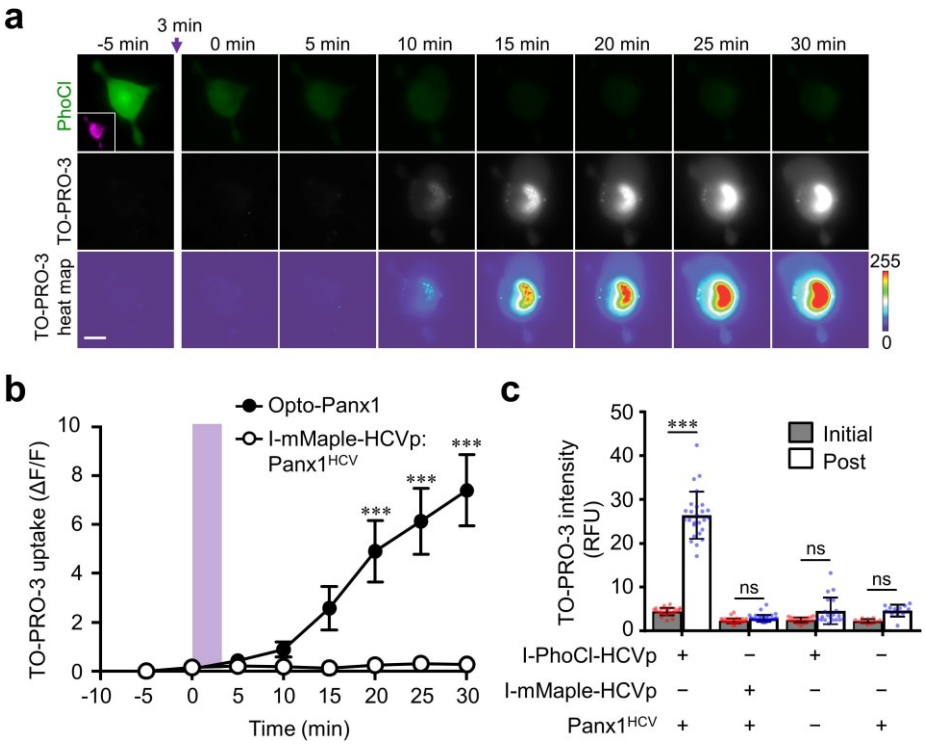

Figure 2.23. Validation of Opto-Panx1 by TO-PRO-3 dye uptake. (**a**) Time-lapse images of TO-PRO-3 dye uptake resulting from 380-nm LED light activation (2.31 mW/mm^2 for 3 min) of Opto-Panx1 in N2a cells. Inset in leftmost PhoCl image shows Panx1^{HCV}-mCherry expression. Scale bar, 10 µm. (**b**) Quantification of dye in cells expressing Panx1^{HCV} and either I-PhoCl-

HCVp (Opto-Panx1) or I-mMaple-HCVp, when activated as in **a** (purple interval). Values are means ± s.d. ($n_{Opto\text{-}Panx1}$ = 26, $n_{I\text{-}mMaple\text{-}HCVp:Panx1HCV}$ = 40), $P_{20\ min}$ = 1.9 × 10^{-9}, $P_{25\ min}$ = 3.6 × 10^{-14}, $P_{30\ min}$ < 1 × 10^{-15} for Opto-Panx1 compared to I-mMaple-HCVp:Panx1^{HCV} by two-way ANOVA (analysis of variance) (F (7, 448) = 25.9). (**c**) Summary data of TO-PRO-3 uptake at 30 min post stimulation (as in **a**). Values are means ± s.d. Opto-Panx1: P = 5×10^{-15}, n = 26; I-mMaple-HCVp with Panx1^{HCV}: P = 0.968, n = 40; I-PhoCl-HCVp only: P = 0.078, n = 20; Panx1^{HCV} only: P = 0.179, n = 12 by one-way ANOVA (F (7,188) = 338.1).

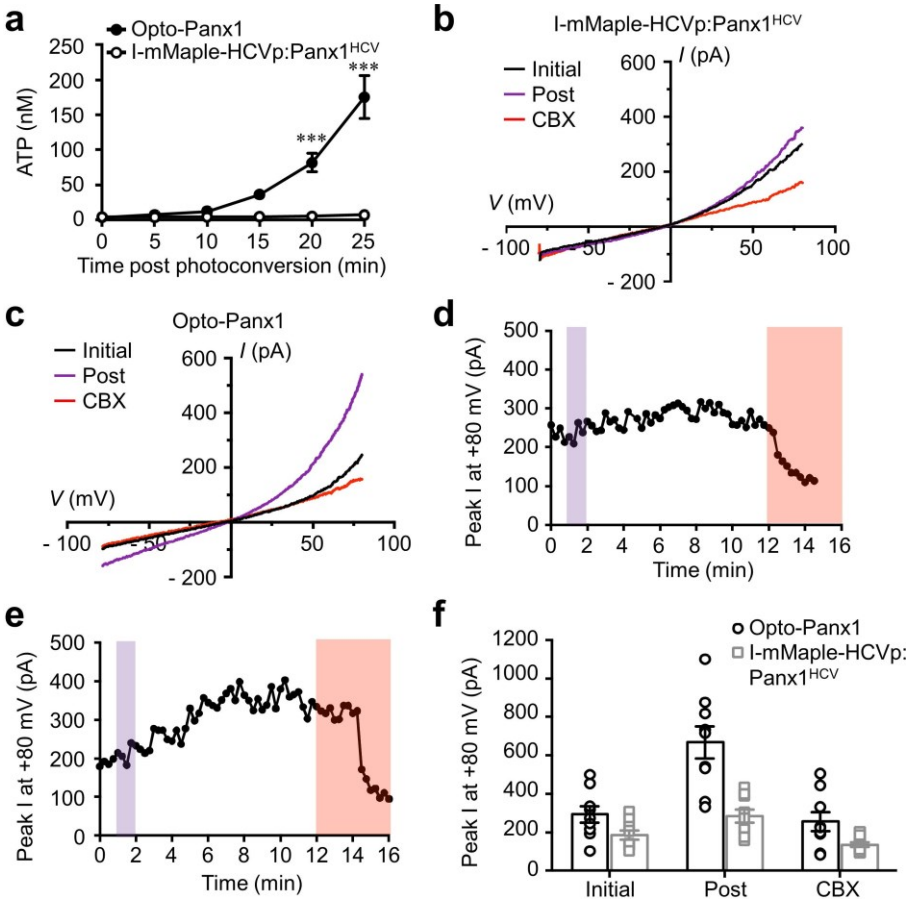

Figure 2.24. ATP release and whole-cell patch clamp analysis of Opto-Panx1 or the mMaple control construct. (**a**) ATP release of HEK 293T cells expressing Panx1^{HCV} and either I-PhoCl-HCVp (Opto-Panx1) or I-mMaple-HCVp, when activated using a 380-nm LED (2.31 mW/mm^2 for 1 min). Values are means ± s.d. ($n_{Opto\text{-}Panx1}$ = 6, $n_{I\text{-}mMaple\text{-}HCVp:Panx1HCV}$ = 6). $P_{20\ min}$ = 3.6 × 10^{-6}, $P_{25\ min}$ < 1 × 10^{-15} by two-way ANOVA (F (5, 50) = 28.6). (**b,c**) Representative

current (I) versus voltage (V) curves for whole-cell patch clamp analysis of HEK 293T cells expressing Panx1^{HCV} and either I-mMaple-HCVp (**b**) or I-PhoCl-HCVp (Opto-Panx1) (**c**). Cells were illuminated as in **a** and then treated with carbenoxolone (CBX: 100 μm). (**d, e**) Representative current (at +80 mV) versus time data for whole-cell patch clamp analysis of HEK 293T cells expressing Panx1^{HCV} and either I-mMaple-HCVp (**d**) or I-PhoCl-HCVp (Opto-Panx1) (**e**). Cells were illuminated as in **a** (purple interval) and treated with carbenoxolone (CBX: 100 μm, 10 min post illumination, red interval). (**f**) Summary data of the maximum Panx1 currents at +80 mV after photoactivation. Cells were treated as in **d,e**. Values are means ± s.d. ($n_{Opto\text{-}Panx1}$ = 8, $n_{I\text{-}mMaple\text{-}HCVp:Panx1HCV}$ = 8).

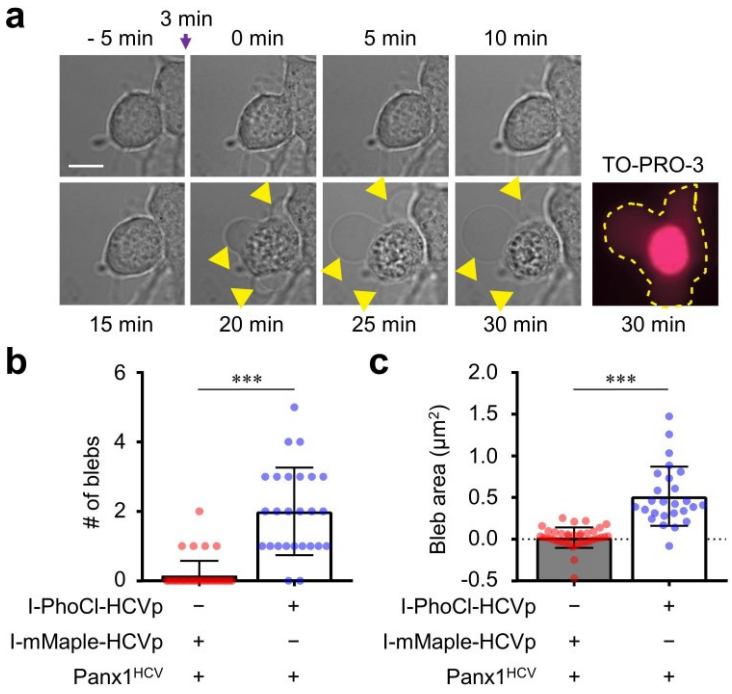

Figure 2.25. Cell blebbing analysis of cells expressing Opto-Panx1 or the mMaple control construct. (**a**) Representative time course images of N2a cells expressing Opto-Panx1 following 3 min of illumination with a 380-nm LED at 2.31 mW/mm^2. Blebs are indicated with yellow arrowheads. Scale bar, 10 μm. (**b**) Summary of number of blebs per cell following activation of Opto-Panx1 or I-mMaple-HCVp:Panx1^{HCV} in N2a cells. Cells were illuminated as in **a**. Values are means ± s.d. ($n_{Opto\text{-}Panx1}$ = 26, $n_{I\text{-}mMaple\text{-}HCVp:Panx1HCV}$ = 40). P = 3.3 ×

10^{-12} by unpaired Student's t-test (t (64) = 8.6). (**c**) Average bleb area per cell for data in **b**. $P = 1.6 \times 10^{-11}$ by unpaired Student's t-test (t (64) = 8.2).

2.3 Conclusion

PhoCl is an optogenetic technology that uses only naturally occurring amino acids and uniquely enables the covalent caging of proteins in an inactive state from which irreversible photocleavage is the only escape. Although no other optogenetic technology shares this feature, it is still informative to compare PhoCl to optogenetic systems that undergo reversible dissociation (e.g., FP-based FLIP [228,229] and LOV2-based LOVTRAP [93]). In reversible systems, the equilibrium between the bound and dissociated protein partners is shifted towards the bound state in the dark and the dissociated state in the light, and necessarily concentration dependent in both states. In contrast, the covalently bonded nature of PhoCl's dark-state means that there is no equilibrium concentration of released state prior to illumination and no concentration dependence. Once uncaged by transient illumination of PhoCl, activated proteins will persist until destroyed by the normal process of intracellular protein degradation. Long-term activation with a reversible system would require constant illumination that could lead to phototoxicity. In this work we have demonstrated a number of applications of PhoCl that illustrate its utility and versatility. We anticipate that PhoCl will prove useful in a yet wider variety of applications that require low levels of dark-state activity, activation on the timescale of minutes, and persistence for prolonged periods of time.

2.4 Materials and methods

2.4.1 General molecular biology methods

Plasmid construction was performed using standard restriction enzyme cloning. Pfu (Thermo Fisher Scientific), Taq (New England BioLabs), and Q5 (New England BioLabs) DNA polymerases were used for polymerase chain reaction (PCR) amplification. Restriction enzymes were purchased from New England BioLabs or Thermo Fisher Scientific. DNA extractions were performed using GeneJET gel extraction kit and plasmid miniprep kit (Thermo Fisher Scientific) according to the manufacturer's protocols. Sequencing reactions were performed at the University of Alberta Molecular Biology Service Unit.

2.4.2 Library creation and screening

Overlap PCR was used to circularly permute the gene encoding mMaple such that the original termini were joined with a GGSGG (G, Gly; S, Ser) linker and new termini were introduced at residue numbers 54/53, 55/54, 56/55, 75/76, 78/77, and 79/78. To create gene libraries, the N- and C-terminal residues were randomized to all 20 amino acids using an NNK codon (where N = A, G, C, T and K = G, T). Circular permutation libraries with termini at the N-terminal side of the central helix (54/53, 55/54, 56/55) were fused to the C-terminus of a gene encoding maltose binding protein (MBP) through a GGGGS linker with a *Kpn*I site. Libraries with termini at the C-terminal side of the central helix (75/76, 78/77, 79/78) were fused to the N-terminus of the gene encoding MBP through a GGGGS linker with a *Kpn*I site. These MBP fusion libraries were inserted between the *Xho*I and *Hind*III sites of pBAD/His B (Thermo Fisher Scientific). DH10B competent cells (Thermo Fisher Scientific) were transformed with these

gene libraries and grown as colonies on Luria-Bertani (LB) agar plates supplemented with 100 μg/mL ampicillin and 0.02% L-arabinose. Fluorescence images of colonies were acquired using a custom-built colony screener [321] equipped with optical filters with the following wavelengths/bandwidths (in nm): excitation 470/40 and emission 510/20 for green channel; excitation 560/40 and emission 630/60 for red channel. Photoconversion was performed using a custom-built 405-nm LED chamber (light intensity 0.15 mW/mm^2), equipped with six 9 × 11 arrays of LEDs (OptoDiode Corporation) [300]. Libraries were screened by fluorescence imaging to identify colonies that exhibited green-to-red photoconversion followed by a rapid loss of red fluorescence in the dark. Data analysis was performed by software Image-Pro 6.0 (Media Cybernetics). Error-prone PCR was used to generate libraries of PhoCl variants. *E. coli* was transformed with plasmid DNA encoding PhoCl libraries, and grown on agar plates overnight. Clones that had bright green fluorescence within 16 to 24 h, underwent green-to-red photoconversion, and exhibited the most rapid loss of red fluorescence following photoconversion, were picked and used as templates for the next round of library creation and screening.

2.4.3 Construction of PhoCl expression vectors

DNA encoding the nuclear exclusion signal (NES) of MAPKK (NLVDLQKKLEELELDEQQ) [322] and the nuclear localization signal (NLS), of SV40 (PKKKRKV) [323] were separately appended to the 5' end of the gene encoding PhoCl by PCR. The gene encoding mCherry was inserted between the *Kpn*I and *Xho*I sites of pcDNA3.1(+) (Thermo Fisher Scientific). Genes encoding NES-PhoCl and NLS-PhoCl were then separately inserted

between *Nhe*I and *Kpn*I of the mCherry-pcDNA3.1(+) plasmid to yield the NES- and NLS-PhoCl-mCherry expression vectors. DNA encoding the myc tag (EQKLISEEDL) was appended to the 3' end of the gene encoding mCherry by PCR. The DNA encoding mCherry-myc (with 5' *Kpn*I and 3' *Hind*III restriction sites) and the DNA encoding PhoCl (with 5' *Nhe*I and 3' *Kpn*I restriction sites) were digested and inserted between the *Nhe*I and *Hind*III sites of pcDNA3.1(+) by 3-part ligation to yield the PhoCl-mCherry-myc expression vector.

The SR-PhoCl-Gal4-VP16-PhoCl-SR expression vector was derived from pCAG-ERT2CreERT2, a gift from Connie Cepko (Addgene plasmid #13777) [306]. pCAG-ERT2CreERT2 has an *Xho*I site between the DNA encoding Cre and the second ERT2. A *Kpn*I restriction site was introduced between the DNA encoding the first ERT2 and Cre by QuikChange site-directed mutagenesis kit (Agilent Genomics). The gene encoding Gal4-VP16 was amplified from N114 nLV EF-1a-Gal4-VP16-PGK-Puro, a gift from Jerry Crabtree (Addgene plasmid #44014) [324]. The gene encoding PhoCl-Gal4-VP16 (with 5' *Kpn*I, 3' *Kpn*2I, and an *Nhe*I restriction site between PhoCl and Gal4-VP16), and the gene encoding PhoCl (with 5' *Kpn*2I and 3' *Xho*I restriction sites), were assembled by overlap PCR and digested with *Kpn*I/*Kpn*2I and *Kpn*2I/*Xho*I, respectively. A 3-part ligation was performed with these two digested fragments and pCAG-ERT2CreERT2 (digested with *Xho*I and *Kpn*I) to produce the SR-PhoCl-Gal4-PhoCl-SR expression vector. To produce the SR-PhoCl-Cre-PhoCl-SR expression vector, the gene encoding Cre was ligated into the *Nhe*I and *Kpn*2I restriction sites of the appropriately digested SR-PhoCl-Gal4-VP16-PhoCl-SR vector.

The pUAS-mCherry-NLS and pUAS-NanoLuc reporter vectors were derived from pUAS-*luc2*, a gift from Liqun Luo (Addgene plasmid #24343) [325]. The DNA encoding the SV40-derived NLS was added to the 3' end of the gene encoding mCherry by PCR. The gene encoding NanoLuc was amplified from pNL1.1[*Nluc*] vector (Promega) by PCR. The genes encoding mCherry-NLS and NanoLuc were cloned between the *EcoR*I and *Xba*I sites of pUAS-*luc2* in place of *luc2*. pLenti-CMV-double floxed-mCherry was used to generate the Cre reporter cell line. It was derived from pLenti CMV GFP Neo (657-2), a gift from Eric Campeau (Addgene plasmid #17447) [326]. The gene encoding double floxed mCherry was amplified by PCR from pAAV-EF1a-double floxed-mCherry-WPRE-HGHpA, a gift from Karl Deisseroth (Addgene plasmid #20299). The DNA encoding double floxed mCherry was cloned between the *Xba*I and *Sal*I sites of pLenti CMV GFP Neo (657-2) in place of the gene for GFP.

To construct I-PhoCl-HCVp expression vectors, the gene encoding hepatitis C virus (HCV) NS3 domain (genotype 1a) was amplified from pCMV-Tag1-NS3, a gift from Xin Wang (Addgene plasmid #17645) [327]. It was genetically changed to the NS3 domain (genotype 1b) (GenBank sequence DQ071885.1 [328]) by site-directed mutagenesis performed by overlap PCR. The DNA encoding the 4A peptide (GSVVIVGRIILS) was added to the 5' end of the DNA encoding the NS3 domain (genotype 1b) through a DNA linker encoding GSGS, by PCR, to make the gene encoding active single-chain HCV NS3-4A serine protease (HCVp) [329]. The gene encoding HCVp was cloned between the *Xho*I and *Hind*III sites of pcDNA3.1(+). DNA encoding for a series of five inhibitory peptides with a range of K_i values (K_i = 0.53 to 105 nM) [310]

were fused to the 5' end of the gene encoding PhoCl through a DNA linker (encoding GGSGGSGGSGGSGSMVSKGEETTM) with an internal *BamH*I site by PCR. These DNA fragments were then ligated to the 5' end of the gene encoding HCVp through a DNA sequence encoding a peptide linker (GGSTDGMDELYKSRGSGTG) with an internal *Xba*I site by overlap PCR. These I-PhoCl-HCVp gene fragments were cloned between the *Xho*I and *Hind*III sites of pcDNA3.1(+). To construct I-mMaple-HCVp control vectors, the gene encoding mMaple was used to replace the gene encoding PhoCl between the *BamH*I and *Xba*I sites of I-PhoCl-HCVp (where I is the three lowest K_i inhibitors from **Figure 2.20**). To construct I-p2A-HCVp control vectors, DNA encoding the p2A peptide (GSGATNFSLLKQAGDVEENPGP) [311] was first generated by Pfu DNA polymerase extension of overlapping forward and reverse oligonucleotides with 5' *BamH*I and 3' *Xba*I. This fragment was cloned between the *BamH*I and *Xba*I sites of I-PhoCl-HCVp in place of the gene encoding PhoCl. The DNA encoding the 4A/4B substrate sequence (DEMEECASHL) [330] of HCVp was added to the 3' end of the gene encoding mCherry through a DNA linker (encoding GSGS) by PCR. DNA encoding the CAAX motif of K-Ras (KMSKDGKKKKKKSKTKCVIM) [331] was further added to the 3' end of the gene encoding mCherry-4A/4B through a DNA linker (encoding GSGS) to get the gene for mCherry-4A/4B-CAAX. This gene was cloned between the *Xho*I and *Hind*III sites of pcDNA3.1(+).

To construct Panx1^{HCV}, DNA encoding the caspase cleavage sequence (GMIKMDVVDG) [312] of Panx1 was exchanged with the DNA encoding the HCVp 4A/4B substrate sequence (DEMEECASHL) [330]. The Panx1^{HCV} expression plasmid was constructed by cloning the gene between the *Nhe*I and

*Hind*III sites of pcDNA3.1(+). The Panx1^{HCV}-mCherry expression plasmid was constructed by first ligating the genes encoding Panx1 and mCherry through an *Xho*I restriction site, and then ligating the fused Panx1^{HCV}-mCherry gene between the *Nhe*I and *Hind*III sites of pcDNA3.1(+).

2.4.4 Protein purification and *in vitro* characterization

The genes for mMaple, PhoCl, and PhoCl-MBP in pBAD/His B were used to transform *E. coli* strain DH10B or Top10. LB media supplemented with 100 µg/mL ampicillin was inoculated with these transformants and the cultures were allowed to grow to an OD_{600} = 0.5. Cultures were induced with 0.02% L-arabinose and allowed to grow overnight at 28 °C, after which the *E. coli* were harvested by centrifugation. The proteins were purified with Ni-NTA agarose (Mclab). Protein concentrations were determined by denaturing in 0.1 M NaOH and using an extinction coefficient at 447 nm of 44,000 $M^{-1}cm^{-1}$ to determine the protein concentration by UV-vis spectroscopy.

Photoconversion was performed using a custom-built 405-nm LED chamber [295]. Absorbance spectra were acquired with a DU-800 UV-visible spectrophotometer (Beckman). Fluorescence spectra were acquired with a Safire2 platereader (Tecan). Gel filtration chromatography was performed with a HiLoad 16/60 Superdex 75 pg column on an AKTA protein purification system (GE Healthcare). To denature mMaple prior to UV-vis spectroscopy, purified mMaple protein was diluted in 50 mM Tris-Cl, 150 mM NaCl, 9 M urea, 1 mM DTT, pH 7.5, and incubated at 95 °C for 5 min.

To perform electrospray mass spectrometry (ESI-MS) analysis of PhoCl, purified protein was concentrated to 6.5 µM in 200 mM NH_4OAc (pH 6.9) using an Amicon Ultra-0.5 mL Centrifugal Filter Unit with Ultracel-10K membrane

(EMD Millipore). Mass spectra were acquired using a Synapt G2S Q-IMS-TOF mass spectrometer (Waters, Manchester, UK) equipped with nanoflow ESI (nanoESI) source.

2.4.5 Cell culture and transfection conditions

All cell lines were grown from their original frozen stocks without authentication or mycoplasma detection. The HEK 293 cell line is listed in the International Cell Line Authentication Committee (ICLAC) database of commonly cross-contaminated or misidentified cell lines. As no endogenous biology was involved, contamination of HEK 293 cell line with HeLa cells would not be expected to affect any of the results reported in this work. HEK 293 (ATCC CRL-1573) and HeLa (ATCC CCL-2) cells were maintained at 37 °C and 5% CO_2 in complete cell culture medium (Dulbecco's modified Eagle medium (DMEM) supplemented with 10% fetal bovine serum (FBS), 10% GlutaMAX (Thermo Fisher Scientific), 1% penicillin, and 1% streptomycin). Cells were seeded in 35 mm glass bottom cell culture dishes (In vitro scientific). For NES- and NLS-PhoCl-mCherry imaging experiments, HeLa cells were transiently transfected with 2 μg of DNA mixed with 4 μL Turbofect transfection reagent (Thermo Fisher Scientific) according to the manufacturer's protocols and cultured for 24 hours prior to experiments. For light induced gene expression with caged Gal4-VP16, HEK 293 cells were co-transfected with DNA vectors encoding SR-PhoCl-Gal4-VP16-PhoCl-SR (1 μg) and either pUAS-mCherry-NLS (1 μg) or pUAS-NanoLuc (1 μg) mixed with 4 μL Turbofect transfection reagent.

For light induced gene expression with caged Cre recombinase, a Cre recombinase reporter cell line was generated. HEK 293FT cells (Thermo Fisher

Scientific) were maintained in complete cell culture medium containing 110 mg/mL sodium pyruvate, at 37 °C and 5% CO_2. HEK 293FT cells in 35 mm cell culture dishes (Corning) with 80% confluency were transfected with 1.5 μg pLenti-CMV-double floxed-mCherry, 1.0 μg psPAX2 (a gift from Didier Trono, Addgene plasmid #12260), 0.5 μg pMD2.G (a gift from Didier Trono, Addgene plasmid #12259), and 0.2 μg pAdvantage (Promega), using 9 μL Turbofect transfection reagent in 2 mL Opti-MEM media (Thermo Fisher Scientific). Opti-MEM media containing Turbofect and DNA mix were replaced with 2 mL complete cell culture medium containing 110 mg/mL sodium pyruvate at 24 hours post-transfection. At 48 hours post-transfection, the virus-containing supernatant was collected, spun at 400g (relative centrifugal force, RCF) for 5 min to pellet cellular debris, and filtered through a 0.45 μm PVDF Syringe Filter Unit (EMD Millipore). HEK 293 cells in 35 mm dishes were transduced with 2 mL virus-containing supernatant. At 24 hours post-transduction, the virus-containing supernatant was replaced with complete cell culture medium containing 500 μg/mL of G418 (Thermo Fisher Scientific) to select and maintain a stable Cre reporter cell line. The Cre reporter cells were seeded in 35 mm glass bottom cell culture dishes and transiently transfected with 2 μg of DNA vector encoding SR-PhoCl-Cre-PhoCl-SR mixed with 4 μL Turbofect transfection reagent.

For imaging of I-PhoCl-HCVp activity in live cells, HeLa cells were cultured as described above and co-transfected with DNA vectors encoding I-PhoCl-HCVp (1 μg) and mCherry-4A/4B-CAAX (1 μg) mixed with 4 μL Turbofect transfection reagent and cultured for 24 hours prior to experiments.

For dye uptake experiments and cell blebbing analysis, Neuro-2a (N2a) cells (ATCC CCL-131) were cultured in DMEM high glucose medium supplemented with 10% FBS, 1% penicillin and 1% streptomycin. Cells were maintained at 37 °C in a humidified cell culture incubator with 22% O_2 and 5% CO_2. For expression of I-PhoCl-HCVp and Panx1^{HCV} constructs, N2a cells were seeded in 35 mm MatTek glass bottom cell culture dishes and transfected with 2.5 µg of each plasmid using 5 µL Lipofectamine 2000 transfection reagent (Thermo Fisher Scientific) and cultured for 48 hours prior to experiments.

For whole-cell patch clamp electrophysiology and ATP release experiments, HEK 293T cells (ATCC CRL-3216) were maintained at 37 °C and 5% CO_2 in complete cell culture medium. HEK 293T cells were seeded in 6-well plates at a density of $1 – 2 \times 10^5$ cells/well and co-transfected with plasmids encoding Panx1^{HCV} and I-PhoCl-HCVp (Opto-Panx1) or I-mMaple-HCVp using Lipofectamine 2000 according to the manufacturer's protocol.

For primed conversion in live cells, HEK 293T cells were co-transfected with pUAS-mCherry-NLS and SR-PhoCl-Gal4-VP16-PhoCl-SR constructs via nucleofection (Lonza nucleofector 4D, SF cell culture kit, program CM150). Transfected cells were immediately seeded into 4-well culture inserts (ibidi GmBH) and kept in the dark.

2.4.6 Cell treatments and imaging conditions

For imaging of protein translocation, images were acquired using a Nikon Eclipse Ti microscope that was equipped with a 75 W Nikon xenon lamp, a 16-bit 512SC QuantEM CCD (Photometrics), and a 20× objective (NA = 0.75, air) and was driven by a NIS-Elements AR 4.20 software package (Nikon). Filter sets had the following wavelengths/bandwidths (in nm): excitation 390/40,

dichroic mirror 425dclp for photoconversion channel; excitation 475/40, dichroic mirror 510dclp, emission 530/50 for GFP; and excitation 543/10, dichroic mirror 565dclp, and emission 620/60 for mCherry. Before photoconversion, images were acquired in the GFP and mCherry channels every 15 s for 2 min. Photoconversion was performed by illumination with 5 s violet light pulses (photoconversion channel, 4.89 mW/mm^2) every 15 s for 6 min. Each light pulse was followed by image acquisition in the GFP and mCherry channels. Image acquisition continued another 9 min after photoconversion. Single cell photoconversion was performed using the Fluorescence Recovery After Photobleaching (FRAP) module of a Ti-LAPP Modular Illumination System (Nikon) equipped with a 405-nm laser (Coherent). Two 25% neutral density filters were used and the laser power measured at the objective was 0.12 mW. Images acquired using the GFP channel were used to track the photoconversion of PhoCl. Red fluorescence images were acquired to analyze protein localization. Image analysis was performed using ImageJ software. For the NES-PhoCl-mCherry construct, protein translocation was analyzed using the ratio of the intensity of the cytoplasm to the intensity of the nucleus. For NLS-PhoCl-mCherry construct, protein translocation was analyzed using the ratio of the intensity of the nucleus to the intensity of the cytoplasm.

For imaging of light induced gene expression, transfected cells were maintained for 24 hours after transfection. Photoconversion was performed using the custom-built 405-nm LED chamber (0.15 mW/mm^2). Each dish of cells (maintained at 37 °C and 5% CO_2) was illuminated for 2 min, once per hour for 3 hours, for a total illumination time of 6 min. For analysis of light induced gene expression, images were acquired 24 hours after the last

illumination using an Axiovert 200M (Zeiss) microscope that was equipped with a 75 W xenon-arc lamp, a 40× objective lens (NA = 1.3, oil), and a 14-bit CoolSnap HQ2 cooled charge-coupled device (CCD) camera (Photometrics) and was driven by μManager software [332]. Filter sets had the following wavelengths/bandwidths (in nm): excitation 470/40, dichroic mirror 495dclp, emission 525/50 for GFP; and excitation 535/50, dichroic mirror 565dclp, and emission 585/29 for mCherry. Images of cells with and without photoconversion were acquired in both the GFP and mCherry channels. For light activated Gal4-VP16, gene expression levels were quantified using the total NanoLuc luminescence or mCherry fluorescence from cell lysates. For light activated Cre, recombination was quantified using mCherry fluorescence from cell lysates and flow cytometry. To measure luminescence, cells in 35 mm dishes were dissociated by addition of 2 mL phosphate-buffered saline (PBS) supplemented with 2 mM ethylenediaminetetraacetic acid (EDTA). The NanoLuc luminescence intensity was quantified using Nano-Glo Luciferase Assay Kit (Promega) and a SpectraMax i3x plate reader (Molecular Devices). To measure fluorescence from cell lysates, cells in 35 mm dishes were lysed by addition of 400 μL M-PER mammalian protein extraction reagent (Thermo Fisher Scientific). Cell debris was removed by centrifugation at 22,500g (RCF) for 2 min. The fluorescence intensity of mCherry in the supernatant was quantified using a Safire2 plate reader (Tecan). For analysis of light activated Cre recombinase by flow cytometry, rates of recombination were quantified for mCherry-positive cells by using BD Accuri™ C6 (BD Biosciences).

For imaging of I-PhoCl-HCVp activity in live cells, images were acquired using the Axiovert 200M (Zeiss) microscope. Filter sets for GFP and mCherry

channels are as described above. A 390/40 nm excitation filter and a 425 nm dclp dichroic mirror were used for photoconversion channel. Before and after illumination, images were acquired in both the GFP and mCherry channels. Photoconversion was performed by illumination (7.23 mW/mm^2) in the photoconversion channel for 1 min. Image analysis was performed using ImageJ software.

For imaging of Opto-Panx1 activity in live cells, transfected cells were washed 3× with an artificial cerebrospinal fluid (aCSF) solution (in mM: 120 NaCl, 26 $NaHCO_3$, 3 KCl, 10 glucose, 1.25 NaH_2PO_4, 1.3 $MgSO_4$, 2 $CaCl_2$, pH = 7.3) and equilibrated for 30 min in aCSF. Dishes were then transferred to a Zeiss AxioObserver.Z1 inverted epifluorescence microscope and continually superfused with fresh aCSF at a rate of 2 mL/min. To photoactivate I-PhoCl-HCVp, cells were illuminated with a 380 nm LED light source (2.31 mW/mm^2). To assess TO-PRO-3 uptake by Opto-Panx1 channels in transfected cells, TO-PRO-3 (1 μM) was superfused into the bath and intracellular fluorescence was monitored every 5 min for 30 min following photoconversion (3 min) and expressed as mean fluorescence intensity in dark and post-illumination states. Cell blebbing was quantified using ImageJ software. Cell area was measured prior to and 30 min after photoactivation and bleb area was calculated as the difference in these values.

2.4.7 Western blot

Quantitative western blotting was performed by conventional protein separation by SDS-PAGE and transfer to nitrocellulose membranes. Briefly, whole cell lysates were obtained from transfected cells using NP-40 lysis buffer (Thermo Fisher) containing protease and phosphatase inhibitors and centrifuged

at 13,000 g to remove cell debris. Total protein was quantified using the Micro BCA Assay Kit (Thermo Fisher) and 25 μg of total protein was separated on 12% Tris-glycine polyacrylamide gels. Following separation, protein was transferred to nitrocellulose membranes which were subsequently blocked for 1 hour with 5% bovine serum albumin (BSA) in Tris-buffered saline (TBS). Membranes were incubated with primary antibodies in TBS with 0.05% Tween-20 (TBST) and 5% BSA overnight at 4°C. Following 3× washes in TBST, membranes were incubated with IRDye secondary antibodies (Li-COR) for 1 hour at room temperature. Membranes were washed 3× in TBST then developed with a Li-COR Odyssey CLx imaging system. For quantification of Opto-Panx1 C-tail cleavage, Opto-Panx1 expressing HEK cells were photoconverted and lysed at 24 hours post transfection. A primary antibody directed towards an epitope residing in the first extracellular loop (Panx1-EL) was used to detect total Panx1 and a primary antibody directed against an epitope distal to the HCVp cleavage site in the Panx1^{HCV} C-terminal domain (Panx1-CT) was used to detect uncleaved Panx1 [319,333]. For analysis of PhoCl photocleavage, HEK 293 cells transfected with the PhoCl-mCherry-myc construct were lysed by addition of 400 μL lysis buffer containing 1% NP-40, 150 mM NaCl, 50 mM Tris, 5 mM EDTA, 1 mM ethylene glycol tetraacetic acid (EGTA), pH 8.0. mCherry-myc dissociation from PhoCl was assessed using a primary antibody directed against the myc tag (Cell Signaling).

2.4.8 Whole-cell patch clamp electrophysiology

At 48 hours post transfection, cells were trypsinized and seeded onto poly-D-lysine coated coverslips. After 1 – 2 hours, coverslips were transferred to a recording chamber and continually perfused with extracellular recording

solution (in mM: 140 NaCl, 3 KCl, 2 $MgCl_2$, 2 $CaCl_2$, 10 HEPES, 10 glucose. pH = 7.3). Whole-cell patch clamp recordings were conducted at room temperature using a MultiClamp 700B amplifier and Digidata 1550A digitizer. Cells were patched with borosilicate glass micro electrodes (Sutter Instrument) with tip resistance of 3 – 5 MΩ pulled using a P-1000 Flaming/Brown Micropipette Puller (Sutter Instrument), and filled with an intracellular solution containing (in mM) 120 CsCl, 1 EGTA, 10 HEPES, 2 Mg-ATP and 0.3 Na_3-GTP. Access resistance was continually monitored and always less than 20 MΩ. Opto-Panx1 or I-mMaple-HCVp:Panx1^{HCV} expressing cells were identified with a Zeiss AxioObserver.Z1 inverted epifluorescence microscope. After entering the whole-cell configuration, cells were held at -60 mV and voltage ramps applied from -80 mV to +80 mV over 150 ms and repeated every 15 s. Following baseline recording, cells were illuminated with a 380 nm LED for 1 min (2.31 mW/mm^2) and recorded for 10 min at which time the Panx1 antagonist carbenoxolone (CBX, 100 μM) was bath applied to isolate CBX-sensitive Panx1 currents. The % change in CBX-sensitive current was calculated at +80 mV as $\frac{(Ipeak-ICBX)-(Iinitial-ICBX)}{(Iinitial-ICBX)} \times 100$, where I_{peak} is the maximum current following illumination, I_{CBX} is the current following CBX application, and $I_{initial}$ is the baseline current prior to illumination.

2.4.9 ATP release assays

Transfected cells were seeded in poly-D-lysine coated 24-well plates and grown to confluence. To quantify ATP release, cells were washed 3× with extracellular recording solution and incubated for 30 min at 37°C. Following 1 min illumination with 380 nm light, supernatant samples were collected at 5

min intervals and immediately placed on ice. ATP concentration was quantified using the ATP Bioluminescence Assay Kit CLSII (Roche) according to the manufacturer's instructions.

2.4.10 Primed conversion *in vitro* and in live cells

For protein immobilization, 100 µL Tris-HCl (1.5 M, pH 7.4), 10 µL of a 10 µM purified protein stock in Tris (0.1 M, pH 7.4), 180 µL 30% acrylamide/bis-acrylamide solution, 1.5 µL 10% ammonium persulfate and 0.5 µL tetramethylethylenediamine were quickly mixed, transferred to a chambered coverslip and left to polymerize for 20 min. Immobilized proteins were converted on an area of 50 × 50 µm.

The imaging and illumination of immobilized proteins and cells was performed on a Zeiss LSM 780 microscope (Carl Zeiss AG) with a C Apo 40×/1.1 W DICIII objective. Light sources included: a Diode 405-30 for 405 nm (4.65 mW at 100%); an argon laser for 458 (0.165 mW at 100%) and 488 nm (1.10 mW at 100%); a diode pumped solid-state laser for 561 nm (3.45 mW at 100%); and a tunable two-photon laser source (Chameleon Ultra II, Coherent Inc.) set to "alignment mode" for continuous wave (i.e., not pulsed) 730 nm excitation (49.0 mW at 100%). Laser powers were measured using a PowerMax USB power meter (Coherent).

For the analysis of primed conversion in live cells, transfected cells were either kept in dark, or illuminated only with 405 nm (5% of maximum power) or 458 nm (50% of maximum power), or simultaneously illuminated with 458 nm (50% of maximum power) and 730 nm (100% power) lasers for 15 s at 24 hours after transfection. Cells were imaged and manually counted using Fiji software 24 hours after illumination.

2.4.11 Statistical analysis.

All data are expressed as means ± s.d. Sample sizes (n) are listed with each experiment. No cell culture samples were excluded from analysis for any reason. No randomization or blinding was used. For protein translocation, whole-cell patch clamp electrophysiology, and cell blebbing experiments, Student's t-test (two-tailed) was used to analyze significant differences between group means. Results were reported as: $P = P$-value and t (degrees-of-freedom (df)) = t-value. For summary data of dye uptake, one-way ANOVA (two-tailed) was used, followed by Tukey *post hoc* test for multiple comparisons. For time-lapse data of dye uptake and ATP release experiments, two-way ANOVA (two-tailed) was used, followed by Sidak *post hoc* test for multiple comparisons. Results for ANOVAs were reported as: $P = P$-value and $F\,(df_{numerator}, df_{denominator}) = F$-value. For all statistics, ns = $P \geq 0.05$, *$P < 0.05$, **$P < 0.01$, ***$P < 0.001$. The significance level (α) was set to be 0.05 for all statistical analysis. There was no estimate of variation within each group of data. Equal variances were not assumed. A normal distribution of each group was verified by the Shapiro-Wilk normality test. Power analysis (power ≥ 80%) for each experiment to validate sample size was done by Stata 12 (STATA).

Chapter 3: Development of a pH-sensitive near-infrared fluorescent protein

3.1 Introduction

Fluorescent protein (FP)-based indicators are among the most impactful and widely-used optogenetic tools. These tools allow researchers to image biological events, such as protein interactions, bioanalyte flux, and enzymatic activities, in real time [256]. Among these biological events, the fluctuations of small molecule and ion bioanalytes, including Ca^{2+}, ATP, Cl^{-}, NO and H^{+}, are particularly important to cell physiology. A broad range of optogenetic reporters have been developed based on the principle of FRET or allosteric effect (as described in section 1.6.5) to monitor the concentration of small molecules and ions in live cells. However, to indicate H^{+} concentration (i.e., pH), GFP and its analogues have a built-in sensing mechanism: the protonation and deprotonation of the chromophore phenolate group causes reversible changes in the fluorescence profile [334].

In 1988, Miesenböck et al. explored this mechanism and engineered two classes of pH-sensitive GFPs (pHluorins) by substituting several key amino acid residues in the vicinity of the chromophore [15]. The resulting pHluorins undergo intensiometric (ecliptic) or ratiometric fluorescence changes in response to physiological pH changes. Superecliptic pHluorin (SEP), a mutant of ecliptic pHluorin with enhanced fluorescence, was later reported [335]. The SEP protein has been extensively used to study exocytosis [335–339], endocytosis [338–342], and autophagy [343], by fusing it to relevant membrane-associated proteins at the luminal side of targeted vesicles. Red FPs

with pH dependence have also been developed [344–347], and used in conjunction with blue-light activated optogenetic tools (e.g., GCaMPs and ChRs), for two-colour imaging or all-optical assays. However, the development of even further red-shifted pH biosensors has been hindered due to the limited wavelength range of GFP-like proteins [348].

To expand the colour palette of pH-sensitive FPs to the near-infrared (NIR) region, we switched our focus to fluorescent variants of biliverdin (BV)-binding bacterial phytochrome photoreceptors (BphPs) [291]. In recent years, a series of NIR FPs have been engineered from various BphPs (**Table 3.1**). This series of NIR FPs are distinct from each other in terms of excitation and emission spectra, *in vitro* brightness (determined as extinction coefficient × quantum yield), oligomeric state, and, most importantly, brightness in mammalian cells. Brightness in cells is a function of multiple parameters including absolute (*in vitro*) brightness, BV binding efficiency, and protein expression level. The NIR FPs have been used to track protein location and dynamics in live cells, and as genetically encoded contrast agents for deep tissue fluorescence imaging. Another burgeoning application of NIR FPs (or their non-fluorescent analogues) is as the contrast agents for photoacoustic tomography (PAT) that detects ultrasonic waves rather than emitted photons, generated by photoexcited molecules [349–351]. Compared with fluorescence imaging that provides either high resolution with short imaging depth or low resolution with long imaging depth, PAT enables deep tissue (up to centimeters) imaging with relative high spatial resolution (~1/200 of imaging depth) [352]. PAT has opened a new era of deep tissue imaging and produced a huge demand for genetically encoded NIR biosensors.

However, despite the ever-growing repertoire of NIR FPs, the development of BphP-based biosensors has lagged far behind the development of biosensors based on avGFP homologues. The only reported examples of BphP-based biosensors have been based on the principle of protein-fragment complementation. The BiFC indicators, including iSplit derived from iRFP [353], IFP PCA (protein-fragment complementation assay) derived from IFP1.4 [354], and miSplit derived from miRFP [291], have been utilized to study PPIs in mammalian cells. As there are a growing number of NIR FP colour variants (**Table 3.1**), it is very likely that FRET-based NIR biosensors will be reported in the near future. Developing NIR biosensors based on allosteric effect or built-in protonation-deprotonation mechanism is a more challenging endeavour, but our lab is currently leading this exploration.

Table 3.1.

Properties of NIR FPs engineered from bacterial phytochromes.

FP	λ_{exi} (nm)	λ_{emi} (nm)	Brightness* ($mM^{-1}cm^{-1}$)	Oligomeric state	Brightness in mammalian cells relative to iRFP713 (%)†	pK_a‡	Ref.
IFP1.4	683	705	6.4	Weak dimer	8	>9.0	[288]
IFP2.0	690	711	7.9	Weak dimer	8, ~100 (coexpressed with heme oxygenase)	>9.5	[355]
mIFP	683	704	6.9	Monomer	15 (105)§	8.9	[290]
iRFP670	643	670	13.9	Dimer	119	>10	[356]
iRFP682	663	682	10.0	Dimer	105	>10	[356]
iRFP702	673	702	7.6	Dimer	61	>10	[356]
iRFP713	690	713	6.2	Dimer	100	>10	[357]
iRFP720	702	720	5.8	Dimer	110	>10	[356]

mIRFP670	642	670	12.2	Monomer	72	>9.5	[291]
mIRFP703	673	703	7.8	Monomer	37	>9.5	[291]
mIRFP709	683	709	4.2	Monomer	30	>9.5	[291]

* Calculated as extinction coefficient × quantum yield.
† Determined as NIR fluorescence intensity normalized by coexpressed GFP in transfected live HeLa cells with no supply of exogenous BV, and measured by Shcherbakova et al. [291].
‡ For the proton associated with the N of BV ring C (**Figure 3.1**).
§ The value in parenthesis was measured by Yu et al. [290].

In this Chapter, we describe our efforts to engineer a pH-sensitive NIR FP, pH-mIFP. The initial pH-sensitive variants were designed semi-rationally. To evolve them for enhanced function, we developed a bacterial colony-based high-throughput screening strategy allowing us to directly evaluate the brightness and pH sensitivity of each variant in Petri dishes. The work led to the identification of pH-mIFP which has been applied in live cells to indicate pH changes. We expect that pH-mIFP could be useful for deep-tissue imaging to report tissue acidification following ischemia as occurs during acute stroke or in tumors [358,359]. It could also be combined with other shorter wavelength biomolecular tools for multi-colour optogenetics.

3.2 Result and discussion

3.2.1 Rational design and library screening

As monomeric NIR FPs are generally more useful than dimeric FPs for subcellular targeting [206,207], we chose mIFP [288] and a monomeric NIR FP derived from *Rhodopseudomonas palustris* BphP1 (called 'mFBphP1' in this thesis), as the templates from which to engineer NIR pH biosensors. The mFBphP1 is an unpublished result from the Edward Boyden lab. It was the best

monomeric NIR FP we were aware of when we initiated this project, and is comparable to the recently published mIRFPs (**Table 3.1**) in terms of the brightness in mammalian cells.

In phytochrome proteins, the BV chromophore is typically protonated at the nitrogen atom of ring C with a positive charge distributed over both B and C rings (**Figure 3.1**) [360]. The pK_a values of most NIR FPs are over 9.0 (**Table 3.1**) and, accordingly, their fluorescence is largely invariant through the physiological pH range (5.5 – 8.5). In contrast, most of traditional FP-based pH indicators (i.e., those based on avGFP homologues) have pK_a values around 7.0. Therefore, we decided to explore the possibility of mutating amino acid residues surrounding the BV chromophore as a means to shift pK_as of the templates into the physiological region. Inspired by a previous study on the pK_as of several bacterial phytochrome mutants [360,361], we chose to target three positions (193, 199 and 252) for site-directed mutagenesis (**Figure 3.1**). The positions are numbered as in mIFP (**Figure 3.2**). Residues 199 and 252 can interact with the chromophore via direct hydrogen binding or through a hydrogen bond network. Residue 193 has been reported to influence the pK_a of phytochrome Agp2 from *Agrobacterium tumefaciens* [361]. We hypothesized that mutating these residues may lead to deprotonation of the chromophore at neutral pH, and thus the resulting proteins would exhibit pH dependent fluorescence changes within the physiological range. To test this hypothesis, we created gene libraries with both templates. In each library, one of the three positions was fully randomized to all 20 amino acid possibilities. We also simultaneously randomized two of the three positions to create three additional libraries for each template, each with $20 \times 20 = 400$ amino acid possibilities.

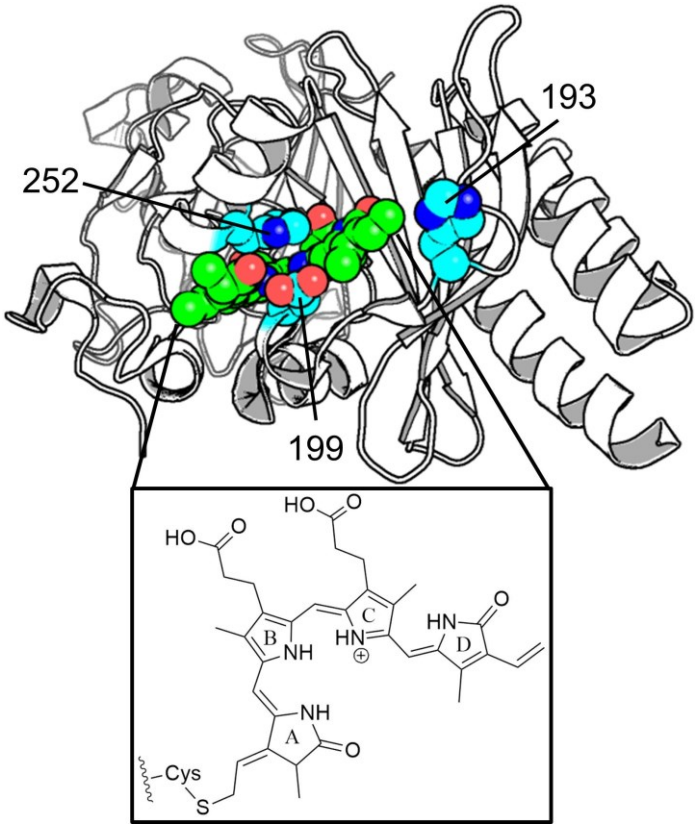

Figure 3.1. Structural representation of mIFP and mFBphP1. It is rendered from the structure of a monomeric bacterial phytochrome from *Deinococcus radiodurans* (PDB ID 4IJG [362]). The positions chosen for site-directed mutagenesis to generate the initial pH-sensitive variants and BV chromophore are coloured cyan and green, respectively.

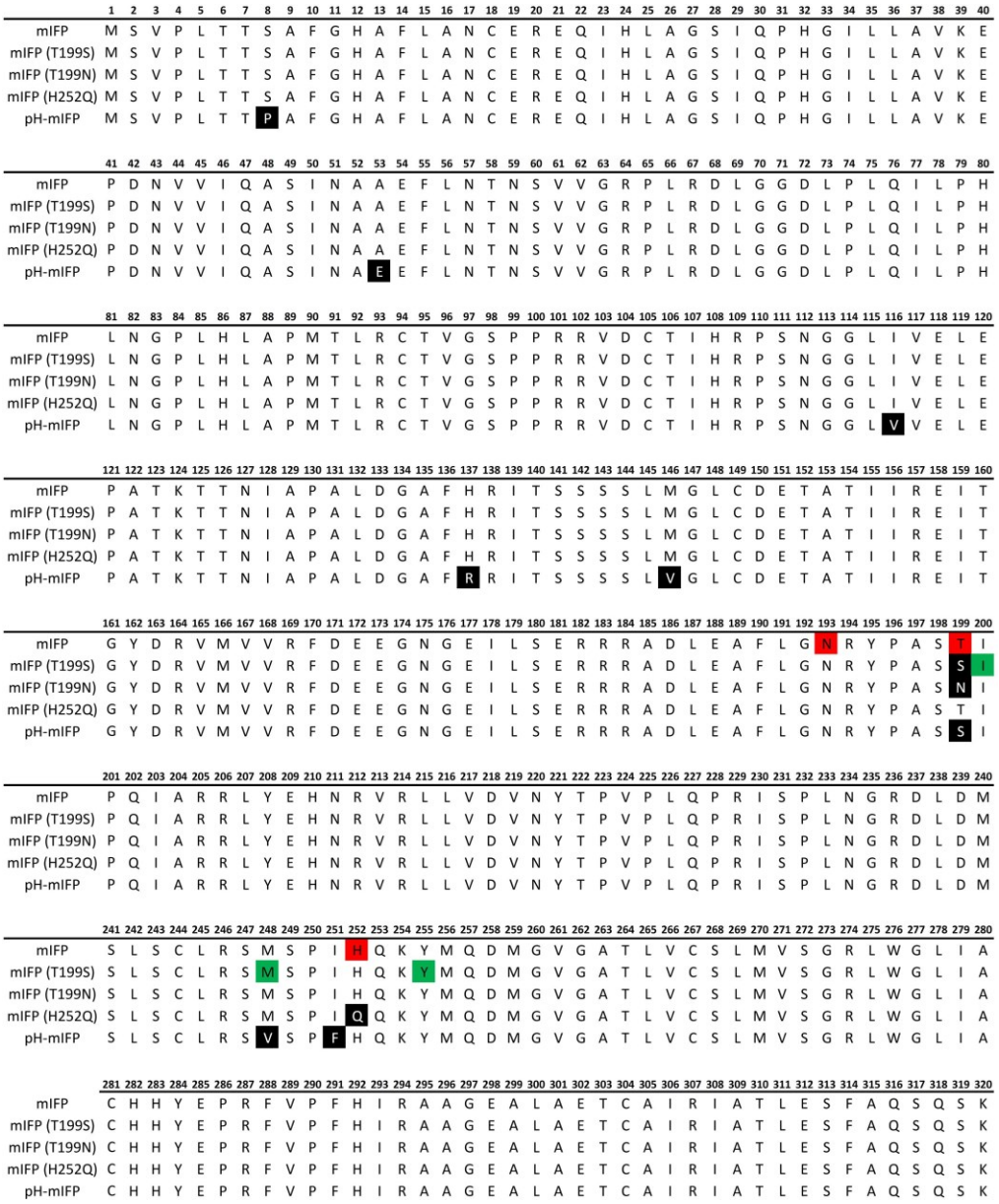

Figure 3.2. Sequence alignment of mIFP and pH-sensitive variants. Mutations relative to mIFP are represented as white text on a black background. The positions randomized for the initial pH-sensitive variants are represented as black text on a red background. The positions randomized on mIFP (T199S) for improved variants are represented as black text on a green background.

To identify the pH-sensitive variants within these libraries, we designed a bacterial colony-based high-throughput screening strategy. We took inspiration from a previous study on bacterial cytosolic pH [363], and reasoned that addition of a permeant acid (e.g., acetic acid) could effectively cause

cytoplasmic acidification (from pH 7.5 to 5.5) in bacterial colonies. To test this hypothesis, we separately transformed *E. coli* with genes encoding the red FP-based pH indicators, pHuji and pHtomato [346,347]. The transformed *E. coli* were grown on LB-agar media in Petri dishes. The expression of pHuji and pHtomato were induced with L-arabinose, and visualized in bacterial colonies using a custom-built colony screener [321]. We acquired red fluorescence images of the Petri dishes before and after overlaying a layer of acidic agar aqueous solution (0.75% agar, 50 mM sodium acetate, 35 mM MES, pH 5.5, ~45°C) on the colonies. The resulting images were then analyzed. The result revealed that the acidic agar overlay led to a decreased red fluorescence in colonies expressing pHuji and pHtomato (**Figure 3.3**). The calculated dynamic ranges (ratio of intensity at pH 7.5 to intensity at 5.5), in the context of *E. coli* colonies, were ~18-fold and ~2.2-fold for pHuji and pHtomato, respectively. These fluorescent changes are consistent with the *in vitro* characterizations of pHuji and pHtomato, which displayed 22-fold and 3-fold fluorescence increases respectively when pH was changed from 5.5 to 7.5 [346]. This effort demonstrated the potential of this method for screening improved pH-sensitive FPs.

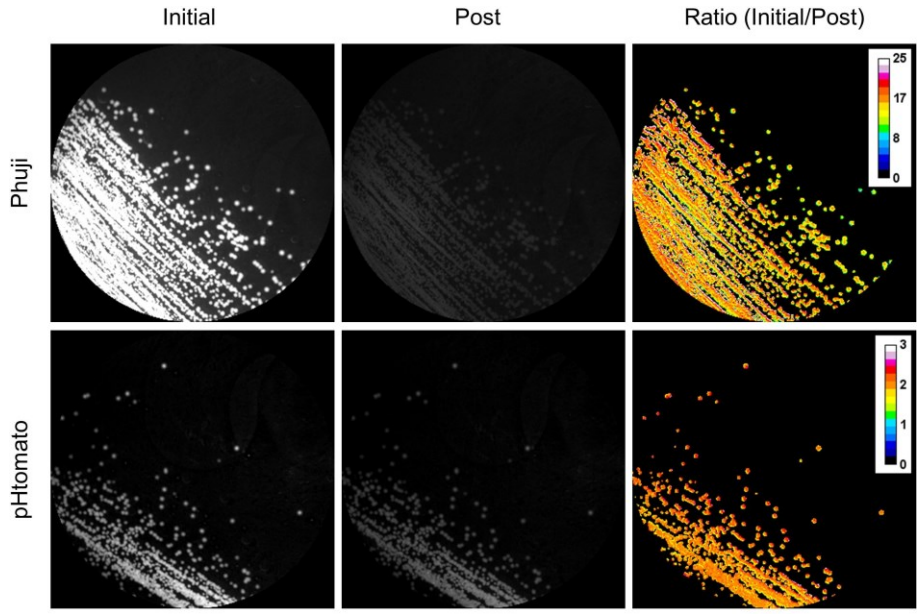

Figure 3.3. Validation of cytoplasmic acidification induced by acidic agar overlay. Fluorescence images of *E. coli* colonies expressing pHuji (top row) and pHtomato (bottom row) were acquired before and after agar addiction. The dynamic ranges were calculated based on the images of colonies.

We proceeded to use this strategy for screening the libraries of NIR FPs to identify the most highly pH-sensitive variants. A bicistronic plasmid was used to co-express the NIR FP variant and the enzyme hemeoxygenase, which is necessary for production of BV from endogenous heme in *E. coli* [288,364]. The screening led to the identification of three pH sensitive fluorescent variants derived from mIFP. These variants, mIFP (T199S), mIFP (T199N) and mIFP (H252Q), were dimly fluorescent at pH 8.5, and exhibited ~11-fold, ~4-fold and ~3-fold higher fluorescence intensity, respectively, at pH 5.5. The Hill coefficient (n_H) for each variant was also determined (**Table 3.2**). Unfortunately, we did not identify any pH-sensitive variants from any of the libraries that were created using the mFBphP1 template.

Table 3.2.

In vitro characterization of pH-sensitive NIR FPs.

FP	λ_{exi}§ (nm)	λ_{emi}§ (nm)	ε ($mM^{-1}cm^{-1}$)	Φ (%)	Brightness* ($mM^{-1}cm^{-1}$)	n_H	pK_a‡	Fluorescence fold change (pH 8.5–5.5) †
mIFP	683	704	82	8.4	6.9	-0.83	8.9	1.5 ± 0.1
mIFP (T199S)	680	704	67	1.2	0.8	-0.64	7.0	11.4 ± 0.2
mIFP (T199N)	682	704	69	1.6	1.1	-0.50	7.2	4.1 ± 0.3
mIFP (H252Q)	678	704	85	2.7	2.3	-0.44	7.8	2.7 ± 0.5
pH-mIFP	680	706	88	5.9	5.2	-0.61	7.0	9.8 ± 0.7

§ λ_{exi} and λ_{emi} are the wavelengths of excitation and emission maxima at pH 5.5.
* Calculated as extinction coefficient (ε) × quantum yield (Φ) at pH 5.5.
‡ For the proton associated with the N of BV ring C (**Figure 3.1**).
† Values are means ± s.d.

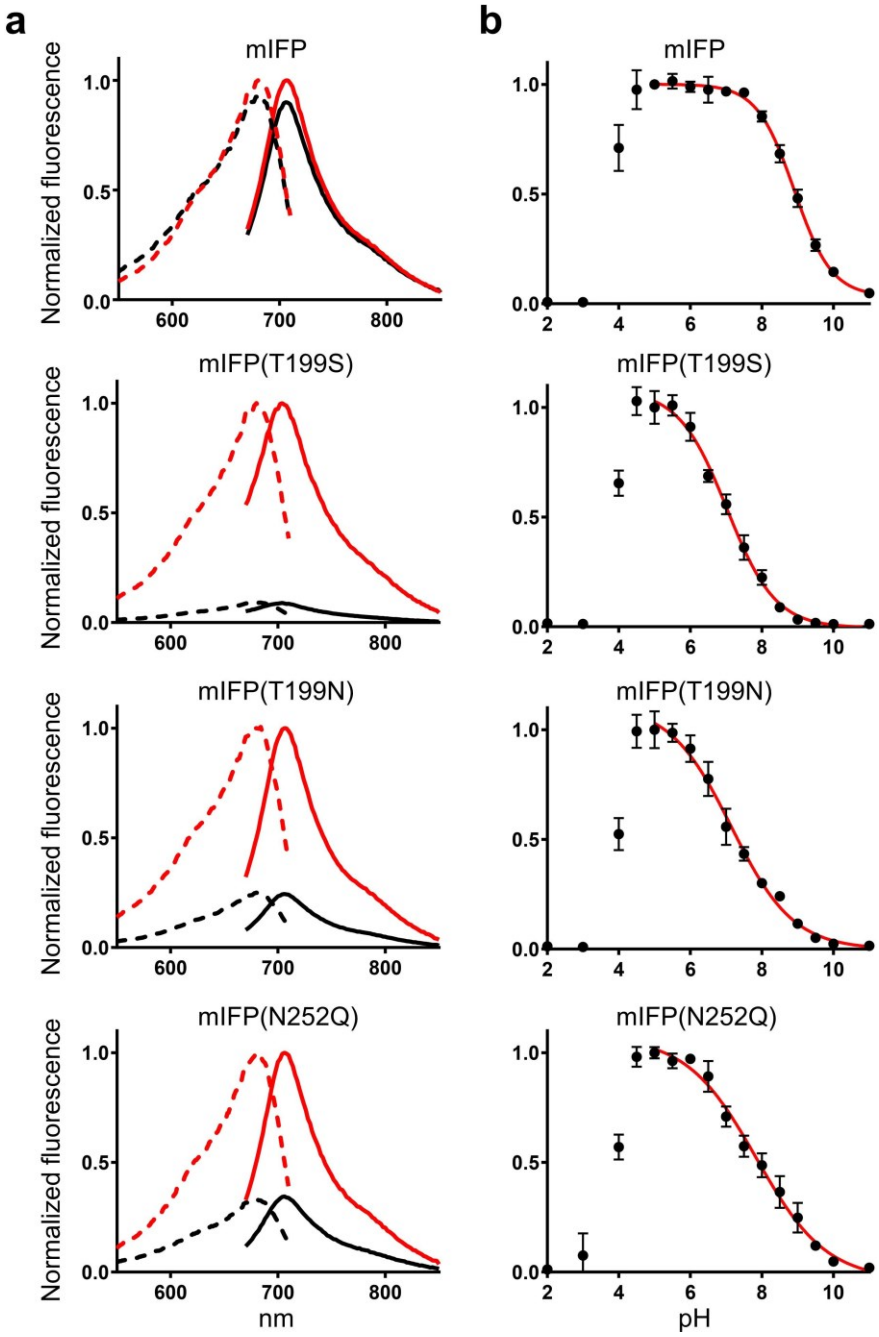

Figure 3.4. Spectra and pH titration curves of mIFP and its pH-sensitive variants. (**a**) Excitation (dashed) and emission (solid) spectra of mIFP, mIFP (T199S), mIFP (T199N) and mIFP (H252Q) at pH 5.5 (red lines) and 8.5 (black lines). (**b**) pH titration curves of the indicated FPs. The data points from pH 5 to 11 were used for curve fitting. Values are means ± s.d. (n = 3 independent experiments).

3.2.2 Directed evolution and characterization

The fluorescent spectroscopic characterization indicated that the apparent pK_a of the initial pH-sensitive mIFP variants were shifted to the neutral pH region (**Table 3.2** and **Figure 3.4**). However, the *in vitro* brightness of these pH sensitive variants was greatly reduced compared with mIFP (**Table 3.2**). We set out to rescue the fluorescence and improve the pH sensitivity by applying a combination of rational design and directed evolution. We chose mIFP (T199S) as the template for further optimization because of its pronounced pH sensitivity (**Table 3.2**). We selected several residues (I200, M248, Y255) (**Figure 3.2**) in close proximity to the BV for saturating site-directed mutagenesis. These efforts were followed by multiple rounds of random mutagenesis of the whole gene using error prone PCR. The resulting libraries were screened by fluorescence imaging of bacterial colonies for enhanced fluorescence, improved pH sensitivity, or a combination of both. After preselection, the candidate clones were cultured, purified, and subjected to a secondary screen in microplate format to determine the fold changes and pK_as. A mixture of 3 – 5 of the best variants was used as the template for the next round of library creation (**Figure 3.5**). This effort ultimately led to the identification of pH-mIFP with a pK_a of 7.0 (**Figure 3.6** and **Table 3.2**). Compared with mIFP (T199S), it is significantly brighter (~75% of the mIFP brightness), and exhibits a similar pH sensitivity (~10-fold fluorescence increase from pH 8.5 to 5.5) and n_H (-0.61) (**Figure 3.6** and **Table 3.2**). To demonstrate the usefulness of pH-mIFP for live cell imaging, we cloned the gene encoding pH-mIFP into the pDisplay vector such that the pH-mIFP protein would be anchored to the cell surface via a C-terminal fused transmembrane domain derived from platelet-derived growth

factor receptor [365]. This vector was used to transfect HeLa cells which were then imaged in buffered solutions ranging from pH 5.5 to 8.5. The fluorescence of HeLa cells expressing pDisplay-pH-mIFP was pH sensitive, exhibiting ~3-fold decrease from pH 5.5 and 8.5 and an apparent pK_a of 7.2 (**Figure 3.7**). The pH sensitivity in this context was less pronounced than that characterized *in vitro*, most likely due to the presence of an intracellular portion of protein that was not secreted to the cell surface, and thus inaccessible to extracellular pH changes [346].

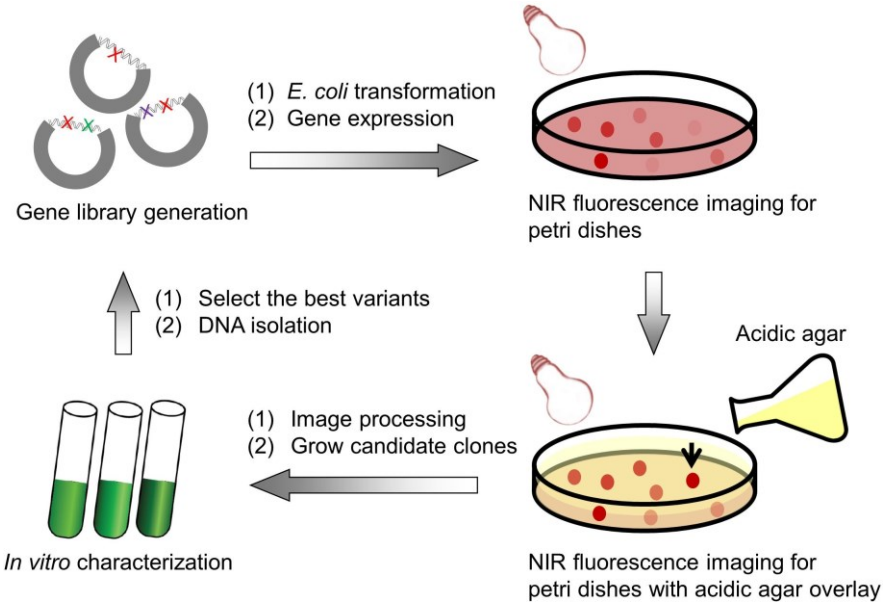

Figure 3.5. Schematic representation of the directed evolution process of pH-mIFP.

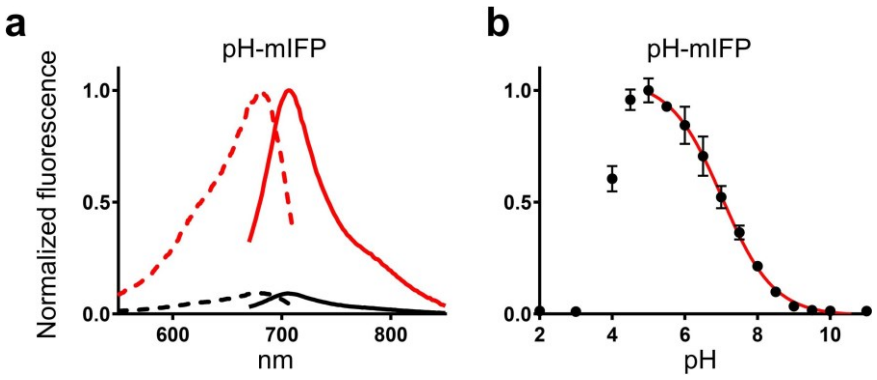

Figure 3.6. Spectra and pH titration curve of pH-mIFP. (**a**) Excitation (dashed) and emission (solid) spectra at pH 5.5 (red lines) and 8.5 (black lines). (**b**) pH titration curves of pH-mIFP. The data points from pH 5 to 11 were used for curve fitting. Values are means ± s.d. (n = 3 independent experiments).

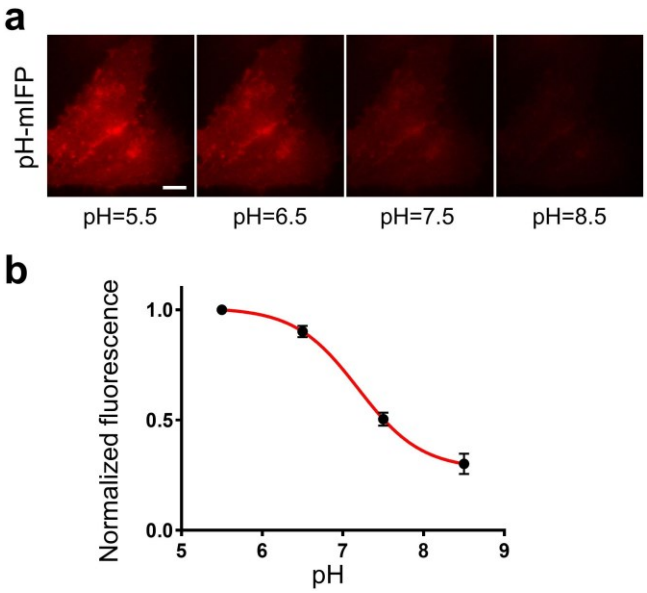

Figure 3.7. Characterization of pH-mIFP on the surface of live cells. (**a**) Fluorescence images of HeLa cells transfected with pDisplay-pH-mIFP. Scale bar = 10 μM. (**b**) Fluorescence intensities (normalized with intensities at pH 5.5) of pH-mIFP expressed on the surface of HeLa cells. Values are means ± s.d. (n = 3 cells).

3.3 Conclusion

By utilizing rational design and directed evolution, we have developed a NIR fluorescent pH indicator, pH-mIFP, with an *in vitro* intensiometric fluorescence change of 9.8 ± 0.7-fold increase upon decreasing pH from 8.5 to 5.5. It has an apparent pK_a of 7.0, which is close to optimal for reporting pH changes in the physiological range, though its pH sensitivity (as characterised by n_H) is relatively low compared with GFP and RFP-based pH indicator such as pHluorins and pHuji that have n_H values of 1.90 and 1.10 respectively

[15,335,346]. pH-mIFP is an inverted pH sensor, as it exhibits a *fluorescence decrease* with increasing pH, which is opposite to the response of all known pH-sensitive FPs. This unique and intriguing property of pH-mIFP may be advantageous in a number of applications, such as the labeling of acidic intracellular vesicles like endosomes, exosomes and maturated autophagosomes. In these cases, we might expect a low background fluorescence attributable to any pH-mIFP protein that is not in an acidic vesicle. As of yet, the utility of pH-mIFP for multicolour optogenetics and deep-tissue imaging remain to be demonstrated. However, we optimistically expect that the high-throughput screening methods we invented for pH-mIFP will prove widely useful to engineer other improved pH-sensitive FPs.

3.4 Materials and methods

3.4.1 General molecular biology methods

The general molecular biology methods used in this chapter were same to those described in section 2.4.1.

3.4.2 Library creation and screening

The DNA encoding mIFP was amplified by PCR amplification from pLenti CMV_mIFP IRES EGFP, a gift from Xiaokun Shu (Addgene plasmid # 72443) [355]; and similarly, the DNA encoding mFBphR1 was amplified from pcDNA-mFBphR1, an unpublished vector from the Edward Boyden lab. The bicistronic bacterial expression vectors of mIFP and mFBphR1 were derived from pBAD-smURFP-RBS-HO-1, a gift from Erik Rodriguez & Roger Tsien (Addgene plasmid # 80341) [364]. The genes encoding mIFP and mFBphR1

were separately digested, and inserted between the *BamH*I and *EcoR*I sites of pBAD-smURFP-RBS-HO-1 in place of smURFP.

For the generation of initial pH-sensitive variants, the codons for residues 193, 199 and 252 were mutated to NNK (encoding all 20 amino acids, where N = A, G, C, T and K = G, T) individually to create libraries with single mutation; and two codons for residues 193 and 199, 193 and 252, or 199 and 252, were mutated to NNK simultaneously to create libraries with double mutations. The site-directed mutagenesis was performed using QuikChange Lightning Site-Directed Mutagenesis Kit (Agilent Technologies). For improved fluorescence and pH sensitivity, the site-directed mutagenesis libraries were created with mIFP (T199S) by mutating the codons encoding residues I200, M248 and Y255 to NNK separately. The following random mutagenesis was generated by error-prone PCR amplification.

DH10B competent cells (ThermoFisher Scientific) were transformed with these gene libraries and grown as colonies on Luria-Bertani (LB) agar plates supplemented with 100 μg/mL ampicillin and 0.02% L-arabinose. NIR fluorescence images of colonies were acquired using a custom-built colony screener [321], equipped with optical filters (Semrock) with the following wavelengths/bandwidths (in nm): excitation 650/60 and emission 795/150. To prepare acidic agar overlay, agar was first mixed pure water. The mixture was heated to melt the agar, cooled to ~45°C at room temperature and added with prewarmed 10× acidic buffer, to get an acidic agar aqueous solution (0.75% agar, 50 mM sodium acetate, 35 mM MES, pH 5.5, ~45°C). Each plate was gently overlaid with 15 mL of the acidic agar solution. NIR fluorescence images of colonies were acquired again immediately after the agar solidified. Libraries

were screened by fluorescence imaging to identify colonies that were dimly fluorescent before and exhibited high brightness after the addition of acid agar. Data analysis was performed by software Image-Pro 6.0 (Media Cybernetics) or ImageJ (open source).

3.4.3 Protein purification and *in vitro* characterization

The genes encoding mIFP, mIFP (T199S), mIFP (T199N), mIFP (H252Q), and pH-mIFP in the bicistronic vector were used to transform *E. coli* strain DH10B or Top10 using Micropulser electroporator (Bio-Rad Laboratories). LB media supplemented with 100 μg/mL ampicillin was inoculated with these transformants and the cultures were allowed to grow to an $OD_{600} = 0.5$. Cultures were induced with 0.02% L-arabinose and allowed to grow overnight at 28 °C, after which the *E. coli* were harvested by centrifugation and lysed by cell disruptor (Constant Systems Ltd). The proteins were purified with Ni-NTA agarose (Mclab). The purified protein was concentrated in Tris buffered saline (TBS: 10 mM Tris-Cl, 150 mM NaCl, pH 7.5), using an Amicon Ultra-15 mL Centrifugal Filter Unit with Ultracel-10K membrane (EMD Millipore).

Absorbance spectra were acquired with a DU-800 UV-visible spectrophotometer (Beckman). Fluorescence spectra were acquired with a Safire2 platereader (Tecan). Protein concentrations were determined by the Pierce BCA kit (Thermo Fisher Scientific). pH titration buffers from pH 2 to 11 were prepared according to the Carmody buffer system [366]. The concentrated protein solutions were diluted with pH titration buffers at pH 5.5 and 7.0 with the same concentration. The extinction coefficient at pH 5.5 for each variant was determine by comparing the absorbance value of the 680-nm peak at pH 5.5 with the absorbance value of the 390-nm peak at pH 7.0. The absorbance

measured at 390 nm was assumed to have the extinction coefficient of the free BV at pH 7.0, which is 39.9 mM^{-1} cm^{-1} [290].

Fluorescence quantum yield (Φ) was determined using mIFP as standard. Briefly, for each variant and mIFP, the concentrated protein solution was diluted with pH titration buffer at pH 5.5 to make a serious of protein solutions with absorbance values ranging from 0.2 to 0.6. For each serious, fluorescence emission spectra were acquired, and the integrations of the total fluorescence intensity were plotted against their absorbance values. The slope (S) was determined by linear regression. Quantum yield of the pH-sensitive variant was then determined by using the following equation: $\Phi_{vatiant} = \Phi_{mIFP} \times (S_{variant}/S_{mIFP})$.

The pH titration was performed by dispensing 5 μL of the concentrated protein solution into 95 μL of the desired pH buffers in a 96-well plate (Thermo Fisher Scientific). The apparent pK_a and Hill coefficient (n_H) were determined by fitting the pH titration data to the following equation (F stands for the normalized fluorescence intensity):

$$F = F_{min} + \frac{F_{max} - F_{min}}{1 + 10^{(pK_a - pH) \times n_H}}$$

3.4.4 Plasmid construction

The genes encoding pHuji and pHtomato were amplified by PCR amplification from pDisplay-pHuji and pDisplay-pHtomato, respectively. The genes were then separately digested and inserted between the *Xho*I and *Hind*III sites of pBAD/His B (Thermo Fisher Scientific), to yield the bacterial expression vectors for pHuji and pHtomato. To construct pDisplay-pH-mIFP

vector for mammalian cell expression, the gene encoding pH-mIFP was cloned between the *Bgl*II and *Sal*I sites of pDisplay-pHuji in place of pHuji.

3.4.5 Cell treatments and imaging conditions

HeLa (ATCC CCL-2) cells were grown from the original frozen stock without authentication or mycoplasma detection, and maintained at 37 °C and 5% CO_2 in complete cell culture medium (Dulbecco's modified Eagle medium (DMEM) supplemented with 10% fetal bovine serum (FBS), 10% GlutaMAX (Thermo Fisher Scientific), 1% penicillin, and 1% streptomycin). Cells were seeded in 35 mm glass bottom cell culture dishes (Cellvis), and cultured until they reached 40–60% confluency. Then, the HeLa cells were transiently transfected with 2 µg of DNA mixed with 4 µL Turbofect transfection reagent (Thermo Fisher Scientific) according to the manufacturer's protocols and cultured for 24 hours prior to experiments.

For cell imaging, the culture medium was changed to Hank's Balanced Salt Solution (HBSS). The pH titration solutions were prepared using the HBSS solution, which was buffered at pH 8.5 and 7.5 with 20 mM HEPES, and at pH 6.5 and 5.5 with 20mM PIPES and MES respectively. Fluorescence images were acquired using a Nikon Eclipse Ti microscope that was equipped with a 75 W Nikon xenon lamp, a 16-bit 512SC QuantEM CCD (Photometrics), and a 40× objective and was driven by a NIS-Elements AR 4.20 software package (Nikon). Filter sets had the following wavelengths/bandwidths (in nm): excitation 650/60, dichroic mirror 715dclp and emission 795/150. The buffer solutions were changed with 10 ml syringes during imaging. Image analysis was performed using ImageJ software (open source).

Chapter 4: Conclusion and future directions

4.1 Summary of thesis

Optogenetics facilitates the precise interrogation of biological processes which display enormous diversity in the mechanism and spatiotemporal scale of molecular actions. In the last decade, the emergence of new classes of optogenetic tools has enabled the optical control of a variety of well-defined biological events. However, owing to complexity of biological system, optogenetics remains a burgeoning field. The development of new tools with generalizable photosensory mechanisms and advanced optical properties is highly desirable.

Despite the relatively rapid expansion of the optogenetic toolbox, the photosensory mechanisms used to design optogenetic actuators *de novo* are limited to just two main categories: 1. light-dependent steric or allosteric control mediated by animal opsins, AsLOV2, and PYPs; and 2. light-induced switches between the oligomeric states of proteins including LOVTRAP, VVD, CRY2, UVR8, Dronpa, and phytochromes. This limited number of options for designing new optogenetic actuators has limited the range of biological processes that can be subjected to optogenetic control. To address this deficiency, we engineered a photocleavable protein (PhoCl) that spontaneously dissociates into two fragments after violet-light-induced cleavage of a specific bond in the protein backbone. PhoCl was adapted to control protein translocation, gene expression, and protein activity in live cells. The work in Chapter 2 demonstrates the utility of the fully genetically encoded photocleavage mediated by PhoCl, as a third category of generalizable

photosensory mechanism for the development of optogenetic actuators.

Optogenetic imaging heavily relies on the development of indicators based on GFP-like proteins. Although tremendous efforts have been made to engineer further red-shifted variants, the practical wavelengths used to excite GFP-like proteins are still restricted to the visible wavelength range. It would be ideal to have a series of similar fluorescent indicators at wavelengths in the NIR optical window, which is optimal for biological imaging in many aspects (as described in section 1.7). The bilin-binding photoreceptor proteins, including phytochromes [289] and allophycocyanin [364], have been engineered for genetically encoded NIR fluorescence as a complement to the conventional FP technology. The development of NIR FP-based indicators is drawing increased attention, but remains challenging. In Chapter 3, we presented our efforts to engineer a NIR fluorescent pH indicator, pH-mIFP, which exhibits an inverted intensiometric fluorescence change compared with the existing FP-based pH indicators. The initial pH dependence of the fluorescence was introduced to mIFP using rational design. The following rounds of directed evolution resulted in variants with improved brightness and photosensitivity. To screen libraries containing up to tens of thousands of mutants, we designed a high-throughput screening strategy which enabled direct estimation of pH responses in bacterial colonies and facilitated the process of directed evolution. This work led to the identification of pH-mIFP which has been applied to indicate pH changes on the surface of mammalian cells.

In summary, this thesis described the development, optimization and application of PhoCl and pH-mIFP technologies. In the following sections of this concluding chapter, we present our general perspectives and prospective

applications for each technology.

4.2 PhoCl: General perspectives and future application

In Chapter 2 we described the development of optogenetic actuators based on a novel photosensory domain PhoCl, which is essentially a circularly permutated version of a green-to-red photoconvertible FP, with its new N- and C-termini at the C-terminal end of the central helix that contains the chromophore. The photoconversion of PhoCl is a violet light (~400 nm)-induced β-elimination reaction on the N-terminal side of the chromophore [216,217], which results in a red-shifted spectrum due to extension of the conjugated system of the chromophore. This β-elimination reaction also results in cleavage of the polypeptide backbone to form a large (~220-residue) N-terminal fragment and a small (~10-residue) C-terminal fragment that spontaneously dissociate. The dissociation is enabled by the circular permutation which has minimized the interaction between the N- and C-terminal fragments produced by photocleavage. Presumably, the relative loose protein structure surrounding the C-terminal portion of the central helix in PhoCl, which is a conjecture based on the crystal structure of its progenitor mTFP [296], may play a role in promoting the dissociation. Our attempts to circularly permute at the loop adjacent to the N-terminal portion of central helix, which is tightly compacted by the β-barrel, did not prove fruitful.

We reported a number of results to support the utility and versatility of PhoCl as an optogenetic technology. PhoCl uniquely enables the covalent trapping of protein away from the action site and the intramolecular caging of protein activity with a proteinaceous inhibitor, both of which could only be released via the irreversible photocleavage. In reversible optogenetic systems,

including both intermolecular (e.g., LOVTRAP, VVD and CRY2) and intramolecular systems (e.g., AsLOV2, BLUF, PYPs and Dronpa), the resting and activated states of the photosensory domain are in equilibrium. Illumination shifts this equilibrium towards the activated state. However, even in the dark there will always be a small fraction of the protein that exists in the activated state. In contrast, the covalently bonded nature of PhoCl's dark state means that there is no equilibrium between bound and released states prior to illumination, and consequently no released state exists in the dark. Upon transient illumination of PhoCl, the trapped or caged POI are released on the timescale of minutes, and the activated proteins persist until they are degraded in cells. According to these features, PhoCl is particular suitable for cell manipulation applications that require protein cleavage, low levels of dark-state activity, transient illumination for photoactivation, and long-term action.

One potential issue with PhoCl technology is the requirement of high-energy violet light to elicit photocleavage, which might lead to phototoxicity. It has been reported that the maximum dose of 405 nm light that cells can tolerate is ~50 J/cm^2 at an irradiation intensity of ~20 W/cm^2, though the use of short pulses of light could further reduce phototoxicity as determined by the ratio of apoptotic to viable cells [367]. The total doses of light used in the applications described in Chapter 2 were all close to or below this level, and at much lower light intensities (0.015 – 0.8 W/cm^2). No significant photodamage effects including plasma membrane permeabilization, cell morphology perturbation and cell death, were observed under these conditions. Regardless, the use of violet light will still remain a concern for users of PhoCl technology in the future.

In an effort to address concerns over phototoxicity, we have demonstrated

that the photocleavage can also be induced by primed conversion [307] with lower energy 458-nm and 730-nm light. However, the efficiency of primed conversion is much lower than that of regular photoconversion and this approach may be insufficient if robust photoactivation of PhoCl-based actuators in live cells is required. Another avenue is to enhance the photoconversion efficiency at 405 nm, which in turn would reduce the amount of violet light required for effective photoactivation. The photoconversion efficiency of photoconvertible FPs (PCFPs) has not received much attention in previous research, as it alone is not the key criterion for the performance of PCFPs for super-resolution microscopy, which has been the most prevalent application of PCFPs [368]. It has been reported by our lab that the photoconversion efficiency of another monomeric PCFP, mEos2, is 2.4× higher than that of mMaple, when determined by the amount of red-state proteins after 1 min conversion in a custom-built LED chamber (405 nm, 0.15 mW/mm^2) [295]. However, the use of mEos2 as a fusion tag for super-resolution imaging has been somewhat limited, possibly due to its tendency to form oligomers [369]. Truly monomeric variants of mEos2, mEos3.1 and mEos3.2, have been developed [369]. Both of these variants, especially the fast-folding mEos3.2, are attractive templates for engineering the next generation of PhoCl that would exhibit higher photoconversion efficiency. However, the reengineering of PhoCl based on Eos proteins might be a highly time-consuming endeavour.

We believe further directed evolution of the current PhoCl variant is a relatively low-risk endeavour. Although efficient photoconversion has been taken into account during the development of PhoCl, fluorescence-based methods for library screening in bacterial colonies proved to be not particularly

effective, as PhoCl does not have particularly bright fluorescence, and fluorescence is not even a necessary property of further improved variants. Non- or weakly fluorescent mutants could easily be ruled out during screening, when the loss of green fluorescence was used to determine the efficiency of photoconversion. A high-throughput screening method that enables direct estimation of photocleavage in colonies would accelerate efforts to identify PhoCl mutants with improved photoconversion. To design such a method, we need to couple the photocleavage of PhoCl with the conditional protein activation systems that could produce signal readouts. Before proceeding with the detailed strategies, we must carefully consider other aspects that might be critical for the performance of PhoCl.

Table 4.1.

Comparison of the photosensory domains used in optogenetic actuators.

Protein domain	**Chromophore**	**λ_{on}[§] (nm)**	**λ_{off}[§] (nm)**	**Turn-on* speed**	**Turn-off* speed**	**Ref.**
Microbial opsins	Retinal; endogenous	400 to 600	NA	milliseconds	milliseconds in the dark	[53]
AsLOV2	FMN; endogenous	450	NA	seconds	seconds to tens of minutes in the dark	[370–372]
VVD	FAD; endogenous	450	NA	seconds	tens of seconds to days in the dark	[99,371,373]
CRY2	FAD; endogenous	450	NA	seconds	minutes to tens of minutes in the dark	[13,122,139]
BLUF	FAD; endogenous	450	NA	seconds	seconds to minutes in the dark	[153]

PYP	pCA; endogenous	450	NA	seconds	milliseconds to minutes in the dark	[175, 176]
UVR8	Tryptophan	300	NA	seconds	irreversible in non-plant cells	[167, 374]
Dronpa	Autogenic	390	490	seconds	Seconds (tens of minutes in the dark)	[228, 229]
PhyB	PCB; Exogenous	650	750	seconds	seconds (hours in the dark)	[272, 277, 371]
Bacterial phytochrome	BV; endogenous	650	750	seconds	seconds (minutes in the dark)	[293, 294]
PhoCl	Autogenic	400	NA	minutes	irreversible	[376]

§ λ_{on} and λ_{off} are the wavelengths of light that can effectively turn on and off the systems, respectively.
* Determined as half of the time required to fully activate and reset the systems.

Table 4.1 compares several properties of the commonly used photosensory domains, which include turn-on and turn-off wavelengths, kinetics, chromophore requirement, and reversibility. The comparison serves as a guide to choosing photosensory domains for optogenetic tool development. Compared with others photosensory domains, the primary limitation of PhoCl is the slow turn-on kinetics which is the result of slow spontaneous dissociation after the photocleavage of peptide backbone. Turn-on kinetics is a key criterion to be considered when an endogenous cell signalling pathway is targeted, as the light-induced perturbation might be compensated by native feedbacks if the turn-on is not fast enough. To speed up the dissociation of PhoCl, we explored two avenues: rational design and directed evolution. Rational design to reduce the interactions between the two fragments after photocleavage proved to be challenging, due to the lack of crystallographic data for PhoCl, especially its

photoconverted state. Several attempts failed to yield any variant with fast dissociation. For directed evolution, we used the loss of red fluorescence to evaluate the spontaneous dissociation after photoconversion. Though the variant identified (PhoCl) has faster dissociation than its prototype (PhoCl0.1), the improvement was moderate. To engineer a PhoCl variant with substantially faster dissociation upon photoconversion, we propose to use directed evolution and a screening method that would allow high-throughput assessment of photoinduced protein fragment separation.

One logical strategy to design a screening method for improved PhoCl variants with enhanced photoconversion and rapid dissociation is to fuse the two split fragments of a reversible protein-fragment complementation assay (PCA) system via PhoCl. When expressed in *E. coli*, the fusion protein would stay active until violet light induces the photocleavage and spontaneous dissociation of PhoCl (**Figure 4.1a**). The reversible PCA systems currently available include: IFP PCA based on IFP1.4 [354]; split UnaG derived from a bilirubin-binding green fluorescent protein UnaG discovered in eel muscle [377,378]; and split luciferases [379–382]. Among them, IFP PCA and split UnaG are fluorescence-based systems. Split UnaG cannot be combined with PhoCl due to the spectrally similar green fluorescence from both proteins. In contrast, IFP PCA is spectrally compatible with PhoCl, however, the half-maximal time value ($T_{1/2}$) of its dissociation was determined to be over one minute [354]. These slow off kinetics would hinder the identification of PhoCl variant that would have a much faster dissociation kinetics than IFP PCA. Compared with IFP PCA, PCA systems based on split luciferases generally have fast off kinetics ($T_{1/2}$ of seconds) [379–382]. One complication might be

that the available split luciferases from firefly [379], copepod [381], sea pansy [380], and deep sea shrimp [382], have emission spectra that overlap with the excitation spectrum of the green or red state of PhoCl. The potential bioluminescence resonance energy transfer (BRET) between the luciferase and PhoCl may interfere the assessment of protein fragment dissociation. Overall, IFP PCA and split luciferases are attractive templates but both have certain drawbacks.

Another intriguing strategy would be to design advanced screening methods for PhoCl based on FRET between NIR FPs. This approach has become feasible in recent years, with the development of colour variants of NIR FPs [289,291]. We suggest choosing a FRET pair that consists of a red-shifted GFP-like protein like mCardinal (λ_{exi} at 604 nm and λ_{emi} at 659 nm) [348] and a monomeric bacterial phytochrome-based FP mIRFP709 (λ_{exi} at 683 nm and λ_{emi} at 709 nm) [291]. A FRET pair such as this could be genetically fused via PhoCl. When expressed in *E. coli*, colonies would exhibit strong fluorescence emission at wavelength range of >700 nm upon excitation at ~600 nm. Such FRET signal would be diminished by the photocleavage and spontaneous dissociation of PhoCl (**Figure 4.1b**). The extent and rate of FRET signal decrease could reveal the photoconversion efficiency and the kinetics of PhoCl fragment dissociation, respectively.

Finally, PhoCl-mediated caging and photo-uncaging of a fluorogenic or chromogenic enzymes may also represent a promising strategy. Here, we take β-lactamase as an example. To cage the activity of β-lactamase, we could fuse a well-characterized protein [383] or peptide [384,385] inhibitor to it via PhoCl. Upon violet light illumination, the β-lactamase would be released from

inhibition, and could freely react with fluorogenic or chromogenic substrates [386,387] (**Figure 4.1c**). However, before bringing such a design to reality, one must evaluate the reaction time required to produce detectable readouts after the substrates are added to the colonies expressing active β-lactamase. The utility of this strategy will largely depend on the activated enzyme having high catalytic rate, and the caged enzyme having low background activity.

In addition to the appropriate design of the gene construct, the other factor that must be considered is the duration of light illumination required for the photoconversion of sufficient amount of PhoCl. Photoconversion in the LED chamber used in this work takes several minutes, which is much longer than the optimum duration (within seconds) desired for fast dissociation. Without a large increase in photoconversion efficiency, increasing light intensity is the only approach towards short and effective photoactivation. A 405 nm LED system with medium to high light intensity (~10 W/cm^2) would also be beneficial for the identification of variant that undergoes decreased photobleaching upon intense light illumination.

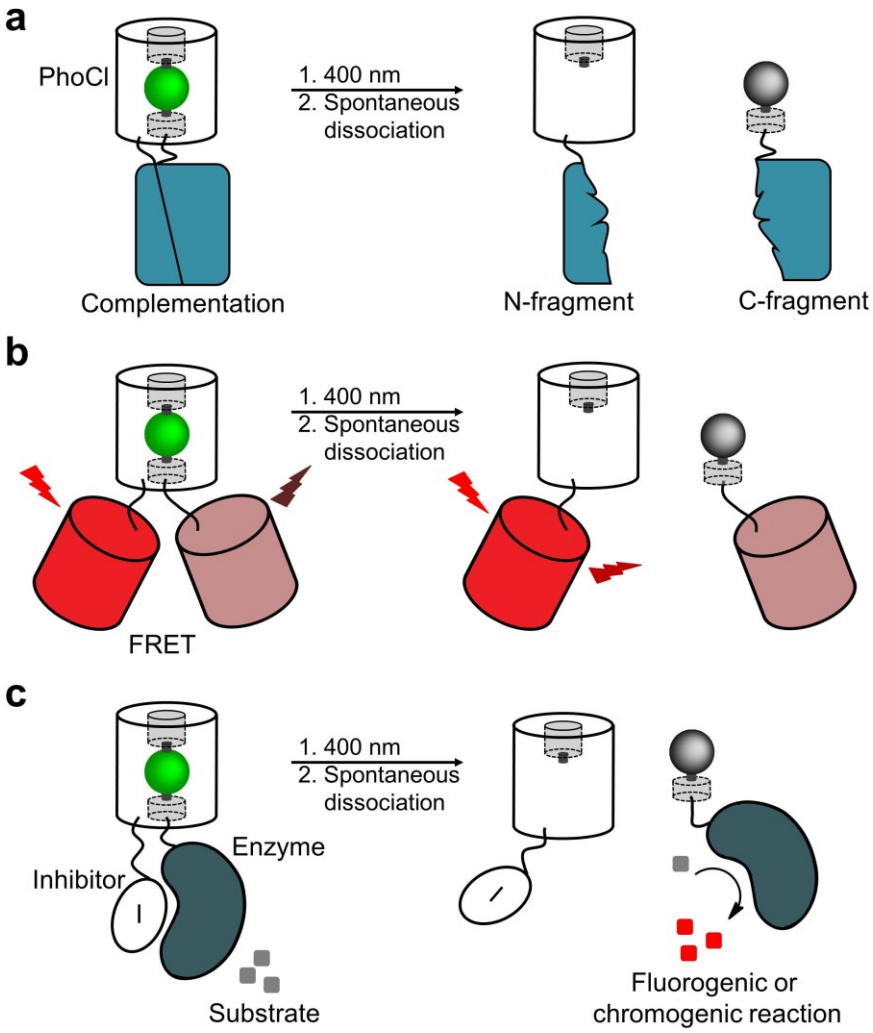

Figure 4.1. Schematic representation of proposed strategies for the discovery of improved PhoCl. (**a**) reversible PCAs. (**b**) FRET between NIR FPs. (**c**) Caging and photo-uncaging of a fluorogenic or chromogenic enzyme.

In this work, we have demonstrated several applications of PhoCl technology that do not require fast turn-on. We anticipate that directed evolution, using one of the proposed advanced screening methods, will lead to the discovery of an improved PhoCl variant that rapidly photoactivates upon violet light illumination. Such a PhoCl variant could be used to covalently trap or cage cell signalling proteins (e.g., kinases, GTPases, and their effectors) in the dark, and induce a surge of activity upon light illumination before any feedback loop dampens the response. Among cell signalling proteins, autoinhibited proteins

are particularly suitable for PhoCl-based optogenetic control. The usage of PhoCl in studying cell signaling remains to be explored.

4.3 pH-mIFP: General perspectives and future application

In Chapter 3 we reported pH-mIFP, an inverted-response intensiometric NIR fluorescent pH indicator. It exhibits 9.8 ± 0.7-fold and 2.6 ± 0.7-fold fluorescence increase *in vitro* upon decreasing pH from 8.5 to 5.5 and from 7.5 to 5.5, respectively. The apparent pK_a of pH-mIFP, determined by the fluorescence change, is 7.0, which is close to optimal for detection of pH changes in the physiological range. **Table 4.2** compares several commonly used FP-based pH indicators with pH-mIFP. The criteria used for comparison are pK_a, Hill coefficient (n_H), fluorescence fold change (pH 5.5 – 7.5), and excitation (λ_{exi}) and emission (λ_{emi}) maxima. Although pH-mIFP uniquely exhibits a NIR fluorescence, and an intensiometric fluorescence decrease with increasing pH, its pH-dependent fluorescence fold change and n_H are relatively low, compared with other pH indicators.

Table 4.2.

Comparison of FP-based pH indicators.

Protein	pK_a	n_H	Fluorescence fold change (pH 5.5–7.5)	λ_{exi} (nm)	λ_{emi} (nm)	Ref.
Superecliptic pHluorin	7.2	1.90	50	495	512	[335,346]
mNectarine	6.9	0.78	6	558	578	[344,346]
pHtomato	7.8	0.51	3	562	578	[346,347]
pHuji	7.7	1.10	22	566	598	[346]
pH-mIFP	7.0	-0.61	0.4	680	706	This work

The pH-mIFP described in this work represents a prototype of this technology. We believe further directed evolution could generate mIFP variants with increased pH sensitivity, while maintaining high brightness. However, for a phytochrome-based FP, the brightness in mammalian cells does not necessarily correspond with its brightness in *E. coli* or *in vitro*. It is also related to the ability to bind endogenous biliverdin and the protein's expression level. To take these factors into consideration for future directed evolution efforts, we suggest introducing a secondary screen in mammalian cells after the high-throughput primary screen in bacterial colonies and *in vitro* characterization. To simplify the screening procedure, one could use a plasmid that contains both mammalian and bacterial promoters, allowing gene expression in both types of cells. The usage of such kind of plasmid has previously been demonstrated in our lab.

In this work, we demonstrated the functionality of pH-mIFP expressed in mammalian cells. However, this simple and preliminary application does not specifically illustrate the strengths of pH-mIFP, including the inverse pH response and NIR fluorescence spectra. Assuming that pH-mIFP can be improved upon, we suggest it could ultimately prove useful for the labeling of acidic intracellular vesicles like endosomes, exosomes and mature autophagosomes, as pH-mIFP in these compartments would be brightly fluorescent. In contrast, any protein that is not properly targeted to an acidic vesicle would exhibit a low background fluorescence. Another promising application of pH-mIFP is deep-tissue imaging to report tissue acidification [358,359]. Since pH-mIFP has its excitation and emission spectra falling in the NIR optical window, it is particularly suitable for tissue imaging with depth

ranging from ~0.1 to 1 cm [267,352]. Finally, we envision the utility of pH-mIFP for multicolour optogenetics in combination with other shorter wavelength tools, such as green and red FP-based indicators [256], and most actuators, with the exception of phytochrome-based based systems like PhyB-PIF [272] and BphP1-PpsR2 [293,294].

4.4 Concluding remarks

In summary, in this thesis I have presented research efforts aimed at developing novel optogenetic tools by protein engineering. First, we exploited circular permutation to design a photocleavable protein (PhoCl) derived from a green-to-red photoconvertible FP. Although the following directed evolution did not lead to a PhoCl variant that has optimal photophysical properties for all purposes, the fast maturation and monomeric structure of PhoCl contribute to its usefulness as a generalizable photosensory domain that can be genetically fused with POIs to exert optogenetic control. Strategies that are suitable for PhoCl-mediated optogenetic control, including covalent trapping and caging of a protein, have been explored. Second, using semi-rational design and extensive directed evolution, we successfully engineered a NIR fluorescent pH indicator pH-mIFP. We validated the functionality of pH-mIFP *in vitro* and on the surface of mammalian cells. Although the characterizations do not yet illustrate the key strengths of pH-mIFP, we propose that it has great potential for vesicle labeling, deep tissue imaging, and multicolour optogenetics. PhoCl and pH-mIFP represent significant additions to the current optogenetic toolbox and will facilitate the design of new optogenetic tools.

Bibliography

1. Deisseroth, K.; Feng, G.; Majewska, A. K.; Miesenbock, G.; Ting, A.; Schnitzer, M. J. Next-Generation Optical Technologies for Illuminating Genetically Targeted Brain Circuits. *J. Neurosci.* **2006**, *26*, 10380–10386.

2. Deisseroth, K. Optogenetics. *Nat. Methods* **2011**, *8*, 26–29.

3. Pastrana, E. Optogenetics: controlling cell function with light. *Nat. Methods* **2011**, *8*, 24–25.

4. van der Horst, M. A.; Hellingwerf, K. J. Photoreceptor Proteins, "Star Actors of Modern Times": A Review of the Functional Dynamics in the Structure of Representative Members of Six Different Photoreceptor Families. *Acc. Chem. Res.* **2004**, *37*, 13–20.

5. Tischer, D.; Weiner, O. D. Illuminating cell signalling with optogenetic tools. *Nat. Rev. Mol. Cell Biol.* **2014**, *15*, 551–558.

6. Davidson, M. W.; Campbell, R. E. Engineered fluorescent proteins: innovations and applications. *Nat. Methods* **2009**, *6*, 713–717.

7. Rodriguez, E. A.; Campbell, R. E.; Lin, J. Y.; Lin, M. Z.; Miyawaki, A.; Palmer, A. E.; Shu, X.; Zhang, J.; Tsien, R. Y. The Growing and Glowing Toolbox of Fluorescent and Photoactive Proteins. *Trends Biochem. Sci.* **2017**, *42*, 111–129.

8. Scanziani, M.; Häusser, M. Electrophysiology in the age of light. *Nature* **2009**, *461*, 930–939.

9. Packer, A. M.; Russell, L. E.; Dalgleish, H. W. P.; Häusser, M. Simultaneous all-optical manipulation and recording of neural circuit activity with cellular resolution *in vivo*. *Nat. Methods* **2014**, *12*, 140–146.

10. Emiliani, V.; Cohen, A. E.; Deisseroth, K.; Häusser, M. All-Optical Interrogation of Neural Circuits. *J. Neurosci. Off. J. Soc. Neurosci.* **2015**, *35*, 13917–13926.

11. Hegemann, P.; Möglich, A. Channelrhodopsin engineering and exploration of new optogenetic tools. *Nat. Methods* **2011**, *8*, 39–42.

12. Strickland, D.; Yao, X.; Gawlak, G.; Rosen, M. K.; Gardner, K. H.; Sosnick, T. R. Rationally improving LOV domain–based photoswitches. *Nat. Methods* **2010**, *7*, 623–626.

13. Taslimi, A.; Zoltowski, B.; Miranda, J. G.; Pathak, G. P.; Hughes, R. M.; Tucker, C. L. Optimized second-generation CRY2−CIB dimerizers and photoactivatable Cre recombinase. *Nat. Chem. Biol.* **2016**, *12*, 425–430.

14. Boyden, E. S.; Zhang, F.; Bamberg, E.; Nagel, G.; Deisseroth, K. Millisecond-timescale, genetically targeted optical control of neural activity. *Nat. Neurosci.* **2005**, *8*, 1263–1268.

15. Miesenböck, G.; De Angelis, D. A.; Rothman, J. E. Visualizing secretion and synaptic transmission with pH-sensitive green fluorescent proteins. *Nature* **1998**, *394*, 192–195.

16. Wu, Y. I.; Frey, D.; Lungu, O. I.; Jaehrig, A.; Schlichting, I.; Kuhlman, B.; Hahn, K. M. A genetically encoded photoactivatable Rac controls the motility of living cells. *Nature* **2009**, *461*, 104–108.

17. Nakai, J.; Ohkura, M.; Imoto, K. A high signal-to-noise Ca^{2+} probe composed of a single green fluorescent protein. *Nat. Biotechnol.* **2001**, *19*, 137–141.

18. Miesenbock, G. The Optogenetic Catechism. *Science* **2009**, *326*, 395–399.

19. Toettcher, J. E.; Voigt, C. A.; Weiner, O. D.; Lim, W. A. The promise of optogenetics in cell biology: interrogating molecular circuits in space and time. *Nat. Methods* **2011**, *8*, 35–38.

20. Shichida, Y.; Matsuyama, T. Evolution of opsins and phototransduction. *Philos. Trans. R. Soc. B Biol. Sci.* **2009**, *364*, 2881–2895.

21. Luecke, H.; Schobert, B.; Richter, H.-T.; Cartailler, J.-P.; Lanyi, J. K. Structure of bacteriorhodopsin at 1.55 Å resolution. *J. Mol. Biol.* **1999**, *291*, 899–911.

22. Palczewski, K.; Kumasaka, T.; Hori, T.; Behnke, C. A.; Motoshima, H.; Fox, B. A.; Le Trong, I.; Teller, D. C.; Okada, T.; Stenkamp, R. E.; Yamamoto, M.; Miyano, M. Crystal structure of rhodopsin: A G protein-coupled receptor. *Science* **2000**, *289*, 739–745.

23. Koyanagi, M.; Terakita, A. Diversity of animal opsin-based pigments and their optogenetic potential. *Biochim. Biophys. Acta* **2014**, *1837*, 710–716.

24. Zhang, F.; Vierock, J.; Yizhar, O.; Fenno, L. E.; Tsunoda, S.; Kianianmomeni, A.; Prigge, M.; Berndt, A.; Cushman, J.; Polle, J.; Magnuson, J.; Hegemann, P.; Deisseroth, K. The Microbial Opsin Family of Optogenetic Tools. *Cell* **2011**, *147*, 1446–1457.

25. Nickle, B.; Robinson, P. R. The opsins of the vertebrate retina: insights from structural, biochemical, and evolutionary studies. *Cell. Mol. Life Sci. CMLS* **2007**, *64*, 2917–2932.

26. Hardie, R. C.; Raghu, P. Visual transduction in Drosophila. *Nature* **2001**, *413*, 186–193.

27. Haupts, U.; Tittor, J.; Bamberg, E.; Oesterhelt, D. General Concept for Ion Translocation by Halobacterial Retinal Proteins: The Isomerization/Switch/Transfer (IST) Model. *Biochemistry (Mosc.)* **1997**, *36*, 2–7.

28. Deisseroth, K. Optogenetics: 10 years of microbial opsins in neuroscience. *Nat. Neurosci.* **2015**, *18*, 1213–1225.

29. Zemelman, B. V.; Lee, G. A.; Ng, M.; Miesenböck, G. Selective Photostimulation of Genetically ChARGed Neurons. *Neuron* **2002**, *33*, 15–22.

30. Montell, C. Drosophila visual transduction. *Trends Neurosci.* **2012**, *35*, 356–363.

31. Kim, J.-M.; Hwa, J.; Garriga, P.; Reeves, P. J.; RajBhandary, U. L.; Khorana, H. G. Light-Driven Activation of β_2 -Adrenergic Receptor Signaling by a Chimeric Rhodopsin Containing the β_2 -Adrenergic Receptor Cytoplasmic Loops. *Biochemistry (Mosc.)* **2005**, *44*, 2284–2292.

32. Airan, R. D.; Thompson, K. R.; Fenno, L. E.; Bernstein, H.; Deisseroth, K. Temporally precise *in vivo* control of intracellular signalling. *Nature* **2009**, *458*, 1025–1029.

33. Oh, E.; Maejima, T.; Liu, C.; Deneris, E.; Herlitze, S. Substitution of 5-HT1A Receptor Signaling by a Light-activated G Protein-coupled Receptor. *J. Biol. Chem.* **2010**, *285*, 30825–30836.

34. Spoida, K.; Masseck, O. A.; Deneris, E. S.; Herlitze, S. Gq/5-HT2c receptor signals activate a local GABAergic inhibitory feedback circuit to modulate serotonergic firing and anxiety in mice. *Proc. Natl. Acad. Sci. U. S. A.* **2014**, *111*, 6479–6484.

35. Siuda, E. R.; Copits, B. A.; Schmidt, M. J.; Baird, M. A.; Al-Hasani, R.; Planer, W. J.; Funderburk, S. C.; McCall, J. G.; Gereau, R. W.; Bruchas, M. R. Spatiotemporal Control of Opioid Signaling and Behavior. *Neuron* **2015**, *86*, 923–935.

36. Kato, H. E.; Zhang, F.; Yizhar, O.; Ramakrishnan, C.; Nishizawa, T.; Hirata, K.; Ito, J.; Aita, Y.; Tsukazaki, T.; Hayashi, S.; Hegemann, P.; Maturana, A. D.; Ishitani, R.; Deisseroth, K.; Nureki, O. Crystal structure of the channelrhodopsin light-gated cation channel. *Nature* **2012**, *482*, 369–374.

37. Nagel, G.; Szellas, T.; Huhn, W.; Kateriya, S.; Adeishvili, N.; Berthold, P.; Ollig, D.; Hegemann, P.; Bamberg, E. Channelrhodopsin-2, a directly light-gated cation-selective membrane channel. *Proc. Natl. Acad. Sci. U. S. A.* **2003**, *100*, 13940–13945.

38. Adamantidis, A. R.; Zhang, F.; Aravanis, A. M.; Deisseroth, K.; de Lecea, L. Neural substrates of awakening probed with optogenetic control of hypocretin neurons. *Nature* **2007**, *450*, 420–424.

39. Tsai, H.-C.; Zhang, F.; Adamantidis, A.; Stuber, G. D.; Bonci, A.; de Lecea, L.; Deisseroth, K. Phasic Firing in Dopaminergic Neurons Is Sufficient for Behavioral Conditioning. *Science* **2009**, *324*, 1080–1084.

40. Gunaydin, L. A.; Yizhar, O.; Berndt, A.; Sohal, V. S.; Deisseroth, K.; Hegemann, P. Ultrafast optogenetic control. *Nat. Neurosci.* **2010**, *13*, 387–392.

41. Berndt, A.; Yizhar, O.; Gunaydin, L. A.; Hegemann, P.; Deisseroth, K. Bi-stable neural state switches. *Nat. Neurosci.* **2009**, *12*, 229–234.

42. Yizhar, O.; Fenno, L. E.; Prigge, M.; Schneider, F.; Davidson, T. J.; O'Shea, D. J.; Sohal, V. S.; Goshen, I.; Finkelstein, J.; Paz, J. T.; Stehfest, K.; Fudim, R.; Ramakrishnan, C.; Huguenard, J. R.; Hegemann, P.; Deisseroth, K. Neocortical excitation/inhibition balance in information processing and social dysfunction. *Nature* **2011**, *477*, 171–178.

43. Berndt, A.; Schoenenberger, P.; Mattis, J.; Tye, K. M.; Deisseroth, K.; Hegemann, P.; Oertner, T. G. High-efficiency channelrhodopsins for fast neuronal stimulation at low light levels. *Proc. Natl. Acad. Sci. U. S. A.* **2011**, *108*, 7595–7600.

44. Lin, J. Y.; Lin, M. Z.; Steinbach, P.; Tsien, R. Y. Characterization of engineered channelrhodopsin variants with improved properties and kinetics. *Biophys. J.* **2009**, *96*, 1803–1814.

45. Lin, J. Y. A user's guide to channelrhodopsin variants: features, limitations and future developments. *Exp. Physiol.* **2011**, *96*, 19–25.

46. Zhang, F.; Prigge, M.; Beyrière, F.; Tsunoda, S. P.; Mattis, J.; Yizhar, O.; Hegemann, P.; Deisseroth, K. Red-shifted optogenetic excitation: a tool for fast neural control derived from Volvox carteri. *Nat. Neurosci.* **2008**, *11*, 631–633.

47. Lin, J. Y.; Knutsen, P. M.; Muller, A.; Kleinfeld, D.; Tsien, R. Y. ReaChR: a red-shifted variant of channelrhodopsin enables deep transcranial optogenetic excitation. *Nat. Neurosci.* **2013**, *16*, 1499–1508.

48. Klapoetke, N. C.; Murata, Y.; Kim, S. S.; Pulver, S. R.; Birdsey-Benson, A.; Cho, Y. K.; Morimoto, T. K.; Chuong, A. S.; Carpenter, E. J.; Tian, Z.; Wang, J.; Xie, Y.; Yan, Z.; Zhang, Y.; Chow, B. Y.; Surek, B.; Melkonian, M.; Jayaraman, V.; Constantine-Paton, M.; Wong, G. K.-S.; Boyden, E. S. Independent optical excitation of distinct neural populations. *Nat. Methods* **2014**, *11*, 338–346.

49. Kleinlogel, S.; Feldbauer, K.; Dempski, R. E.; Fotis, H.; Wood, P. G.; Bamann, C.; Bamberg, E. Ultra light-sensitive and fast neuronal activation with the Ca^{2+}-permeable channelrhodopsin CatCh. *Nat. Neurosci.* **2011**, *14*, 513–518.

50. Dunn, R. J.; Hackett, N. R.; McCoy, J. M.; Chao, B. H.; Kimura, K.; Khorana, H. G. Structure-function studies on bacteriorhodopsin. I. Expression

of the bacterio-opsin gene in Escherichia coli. *J. Biol. Chem.* **1987**, *262*, 9246–9254.

51. Kolbe, M. Structure of the Light-Driven Chloride Pump Halorhodopsin at 1.8 Å Resolution. *Science* **2000**, *288*, 1390–1396.

52. Zhang, F.; Wang, L.-P.; Brauner, M.; Liewald, J. F.; Kay, K.; Watzke, N.; Wood, P. G.; Bamberg, E.; Nagel, G.; Gottschalk, A.; Deisseroth, K. Multimodal fast optical interrogation of neural circuitry. *Nature* **2007**, *446*, 633–639.

53. Mattis, J.; Tye, K. M.; Ferenczi, E. A.; Ramakrishnan, C.; O'Shea, D. J.; Prakash, R.; Gunaydin, L. A.; Hyun, M.; Fenno, L. E.; Gradinaru, V.; Yizhar, O.; Deisseroth, K. Principles for applying optogenetic tools derived from direct comparative analysis of microbial opsins. *Nat. Methods* **2011**, *9*, 159–172.

54. Wietek, J.; Wiegert, J. S.; Adeishvili, N.; Schneider, F.; Watanabe, H.; Tsunoda, S. P.; Vogt, A.; Elstner, M.; Oertner, T. G.; Hegemann, P. Conversion of Channelrhodopsin into a Light-Gated Chloride Channel. *Science* **2014**, *344*, 409–412.

55. Berndt, A.; Lee, S. Y.; Ramakrishnan, C.; Deisseroth, K. Structure-Guided Transformation of Channelrhodopsin into a Light-Activated Chloride Channel. *Science* **2014**, *344*, 420–424.

56. Govorunova, E. G.; Sineshchekov, O. A.; Janz, R.; Liu, X.; Spudich, J. L. Natural light-gated anion channels: A family of microbial rhodopsins for advanced optogenetics. *Science* **2015**, *349*, 647–650.

57. Wietek, J.; Broser, M.; Krause, B. S.; Hegemann, P. Identification of a Natural Green Light Absorbing Chloride Conducting Channelrhodopsin from *Proteomonas sulcata*. *J. Biol. Chem.* **2016**, *291*, 4121–4127.

58. Mohammad, F.; Stewart, J. C.; Ott, S.; Chlebikova, K.; Chua, J. Y.; Koh, T.-W.; Ho, J.; Claridge-Chang, A. Optogenetic inhibition of behavior with anion channelrhodopsins. *Nat. Methods* **2017**, *14*, 271–274.

59. Rost, B. R.; Schneider, F.; Grauel, M. K.; Wozny, C.; G Bentz, C.; Blessing, A.; Rosenmund, T.; Jentsch, T. J.; Schmitz, D.; Hegemann, P.; Rosenmund, C. Optogenetic acidification of synaptic vesicles and lysosomes. *Nat. Neurosci.* **2015**, *18*, 1845–1852.

60. Kralj, J. M.; Douglass, A. D.; Hochbaum, D. R.; Maclaurin, D.; Cohen, A. E. Optical recording of action potentials in mammalian neurons using a microbial rhodopsin. *Nat. Methods* **2011**, *9*, 90–95.

61. Hochbaum, D. R.; Zhao, Y.; Farhi, S. L.; Klapoetke, N.; Werley, C. A.; Kapoor, V.; Zou, P.; Kralj, J. M.; Maclaurin, D.; Smedemark-Margulies, N.; Saulnier, J. L.; Boulting, G. L.; Straub, C.; Cho, Y. K.; Melkonian, M.; Wong,

G. K.-S.; Harrison, D. J.; Murthy, V. N.; Sabatini, B. L.; Boyden, E. S.; Campbell, R. E.; Cohen, A. E. All-optical electrophysiology in mammalian neurons using engineered microbial rhodopsins. *Nat. Methods* **2014**, *11*, 825–833.

62. Avelar, G. M.; Schumacher, R. I.; Zaini, P. A.; Leonard, G.; Richards, T. A.; Gomes, S. L. A Rhodopsin-Guanylyl Cyclase Gene Fusion Functions in Visual Perception in a Fungus. *Curr. Biol.* **2014**, *24*, 1234–1240.

63. Gao, S.; Nagpal, J.; Schneider, M. W.; Kozjak-Pavlovic, V.; Nagel, G.; Gottschalk, A. Optogenetic manipulation of cGMP in cells and animals by the tightly light-regulated guanylyl-cyclase opsin CyclOp. *Nat. Commun.* **2015**, *6*, 8046.

64. Massey, V. The chemical and biological versatility of riboflavin. *Biochem. Soc. Trans.* **2000**, *28*, 283–296.

65. Losi, A.; Gärtner, W. Old Chromophores, New Photoactivation Paradigms, Trendy Applications: Flavins in Blue Light-Sensing Photoreceptors†. *Photochem. Photobiol.* **2011**, *87*, 491–510.

66. Losi, A.; Gärtner, W. The evolution of flavin-binding photoreceptors: an ancient chromophore serving trendy blue-light sensors. *Annu. Rev. Plant Biol.* **2012**, *63*, 49–72.

67. Conrad, K. S.; Manahan, C. C.; Crane, B. R. Photochemistry of flavoprotein light sensors. *Nat. Chem. Biol.* **2014**, *10*, 801–809.

68. Christie, J. M. Arabidopsis NPH1: A Flavoprotein with the Properties of a Photoreceptor for Phototropism. *Science* **1998**, *282*, 1698–1701.

69. Glantz, S. T.; Carpenter, E. J.; Melkonian, M.; Gardner, K. H.; Boyden, E. S.; Wong, G. K.-S.; Chow, B. Y. Functional and topological diversity of LOV domain photoreceptors. *Proc. Natl. Acad. Sci. U. S. A.* **2016**, *113*, E1442–E1451.

70. Herrou, J.; Crosson, S. Function, structure and mechanism of bacterial photosensory LOV proteins. *Nat. Rev. Microbiol.* **2011**, *9*, 713–723.

71. Schleicher, E.; Kowalczyk, R. M.; Kay, C. W. M.; Hegemann, P.; Bacher, A.; Fischer, M.; Bittl, R.; Richter, G.; Weber, S. On the Reaction Mechanism of Adduct Formation in LOV Domains of the Plant Blue-Light Receptor Phototropin. *J. Am. Chem. Soc.* **2004**, *126*, 11067–11076.

72. Harper, S. M. Structural Basis of a Phototropin Light Switch. *Science* **2003**, *301*, 1541–1544.

73. Möglich, A.; Yang, X.; Ayers, R. A.; Moffat, K. Structure and Function of Plant Photoreceptors. *Annu. Rev. Plant Biol.* **2010**, *61*, 21–47.

74. Mukherjee, A.; Schroeder, C. M. Flavin-based fluorescent proteins: emerging paradigms in biological imaging. *Curr. Opin. Biotechnol.* **2015**, *31*, 16–23.

75. Drepper, T.; Eggert, T.; Circolone, F.; Heck, A.; Krauß, U.; Guterl, J.-K.; Wendorff, M.; Losi, A.; Gärtner, W.; Jaeger, K.-E. Reporter proteins for *in vivo* fluorescence without oxygen. *Nat. Biotechnol.* **2007**, *25*, 443–445.

76. Chapman, S.; Faulkner, C.; Kaiserli, E.; Garcia-Mata, C.; Savenkov, E. I.; Roberts, A. G.; Oparka, K. J.; Christie, J. M. The photoreversible fluorescent protein iLOV outperforms GFP as a reporter of plant virus infection. *Proc. Natl. Acad. Sci. U. S. A.* **2008**, *105*, 20038–20043.

77. Ruiz-González, R.; Cortajarena, A. L.; Mejias, S. H.; Agut, M.; Nonell, S.; Flors, C. Singlet Oxygen Generation by the Genetically Encoded Tag miniSOG. *J. Am. Chem. Soc.* **2013**, *135*, 9564–9567.

78. Qi, Y. B.; Garren, E. J.; Shu, X.; Tsien, R. Y.; Jin, Y. Photo-inducible cell ablation in Caenorhabditis elegans using the genetically encoded singlet oxygen generating protein miniSOG. *Proc. Natl. Acad. Sci. U. S. A.* **2012**, *109*, 7499–7504.

79. Shu, X.; Lev-Ram, V.; Deerinck, T. J.; Qi, Y.; Ramko, E. B.; Davidson, M. W.; Jin, Y.; Ellisman, M. H.; Tsien, R. Y. A Genetically Encoded Tag for Correlated Light and Electron Microscopy of Intact Cells, Tissues, and Organisms. *PLoS Biol.* **2011**, *9*, e1001041.

80. Motta-Mena, L. B.; Reade, A.; Mallory, M. J.; Glantz, S.; Weiner, O. D.; Lynch, K. W.; Gardner, K. H. An optogenetic gene expression system with rapid activation and deactivation kinetics. *Nat. Chem. Biol.* **2014**, *10*, 196–202.

81. Yazawa, M.; Sadaghiani, A. M.; Hsueh, B.; Dolmetsch, R. E. Induction of protein-protein interactions in live cells using light. *Nat. Biotechnol.* **2009**, *27*, 941–945.

82. Harper, S. M.; Christie, J. M.; Gardner, K. H. Disruption of the LOV−Jα Helix Interaction Activates Phototropin Kinase Activity. *Biochemistry (Mosc.)* **2004**, *43*, 16184–16192.

83. Schmidt, D.; Tillberg, P. W.; Chen, F.; Boyden, E. S. A fully genetically encoded protein architecture for optical control of peptide ligand concentration. *Nat. Commun.* **2014**, *5*.

84. Lee, J.; Natarajan, M.; Nashine, V. C.; Socolich, M.; Vo, T.; Russ, W. P.; Benkovic, S. J.; Ranganathan, R. Surface Sites for Engineering Allosteric Control in Proteins. *Science* **2008**, *322*, 438–442.

85. Strickland, D.; Moffat, K.; Sosnick, T. R. Light-activated DNA binding in a designed allosteric protein. *Proc. Natl. Acad. Sci. U. S. A.* **2008**, *105*, 10709–10714.

86. Cosentino, C.; Alberio, L.; Gazzarrini, S.; Aquila, M.; Romano, E.; Cermenati, S.; Zuccolini, P.; Petersen, J.; Beltrame, M.; Van Etten, J. L.; Christie, J. M.; Thiel, G.; Moroni, A. Engineering of a light-gated potassium channel. *Science* **2015**, *348*, 707–710.

87. Strickland, D.; Lin, Y.; Wagner, E.; Hope, C. M.; Zayner, J.; Antoniou, C.; Sosnick, T. R.; Weiss, E. L.; Glotzer, M. TULIPs: tunable, light-controlled interacting protein tags for cell biology. *Nat. Methods* **2012**, *9*, 379–384.

88. Niopek, D.; Benzinger, D.; Roensch, J.; Draebing, T.; Wehler, P.; Eils, R.; Di Ventura, B. Engineering light-inducible nuclear localization signals for precise spatiotemporal control of protein dynamics in living cells. *Nat. Commun.* **2014**, *5*.

89. Niopek, D.; Wehler, P.; Roensch, J.; Eils, R.; Di Ventura, B. Optogenetic control of nuclear protein export. *Nat. Commun.* **2016**, *7*, 10624.

90. Fukuda, N.; Matsuda, T.; Nagai, T. Optical Control of the Ca^{2+} Concentration in a Live Specimen with a Genetically Encoded Ca^{2+} -Releasing Molecular Tool. *ACS Chem. Biol.* **2014**, *9*, 1197–1203.

91. Nakamura, M.; Chen, L.; Howes, S. C.; Schindler, T. D.; Nogales, E.; Bryant, Z. Remote control of myosin and kinesin motors using light-activated gearshifting. *Nat. Nanotechnol.* **2014**, *9*, 693–697.

92. Dagliyan, O.; Tarnawski, M.; Chu, P.-H.; Shirvanyants, D.; Schlichting, I.; Dokholyan, N. V.; Hahn, K. M. Engineering extrinsic disorder to control protein activity in living cells. *Science* **2016**, *354*, 1441–1444.

93. Wang, H.; Vilela, M.; Winkler, A.; Tarnawski, M.; Schlichting, I.; Yumerefendi, H.; Kuhlman, B.; Liu, R.; Danuser, G.; Hahn, K. M. LOVTRAP: an optogenetic system for photoinduced protein dissociation. *Nat. Methods* **2016**, *13*, 755–758.

94. Yao, X.; Rosen, M. K.; Gardner, K. H. Estimation of the available free energy in a LOV2-Jα photoswitch. *Nat. Chem. Biol.* **2008**, *4*, 491–497.

95. Lungu, O. I.; Hallett, R. A.; Choi, E. J.; Aiken, M. J.; Hahn, K. M.; Kuhlman, B. Designing Photoswitchable Peptides Using the AsLOV2 Domain. *Chem. Biol.* **2012**, *19*, 507–517.

96. Zoltowski, B. D.; Crane, B. R. Light Activation of the LOV Protein Vivid Generates a Rapidly Exchanging Dimer. *Biochemistry (Mosc.)* **2008**, *47*, 7012–7019.

97. Wang, X.; Chen, X.; Yang, Y. Spatiotemporal control of gene expression by a light-switchable transgene system. *Nat. Methods* **2012**, *9*, 266–269.

98. Han, T.; Chen, Q.; Liu, H. Engineered Photoactivatable Genetic Switches Based on the Bacterium Phage T7 RNA Polymerase. *ACS Synth. Biol.* **2017**, *6*, 357–366.

99. Kawano, F.; Suzuki, H.; Furuya, A.; Sato, M. Engineered pairs of distinct photoswitches for optogenetic control of cellular proteins. *Nat. Commun.* **2015**, *6*, 6256.

100. Yu, G.; Onodera, H.; Aono, Y.; Kawano, F.; Ueda, Y.; Furuya, A.; Suzuki, H.; Sato, M. Optical manipulation of the alpha subunits of heterotrimeric G proteins using photoswitchable dimerization systems. *Sci. Rep.* **2016**, *6*, 35777.

101. Nihongaki, Y.; Kawano, F.; Nakajima, T.; Sato, M. Photoactivatable CRISPR-Cas9 for optogenetic genome editing. *Nat. Biotechnol.* **2015**, *33*, 755–760.

102. Kawano, F.; Okazaki, R.; Yazawa, M.; Sato, M. A photoactivatable Cre–loxP recombination system for optogenetic genome engineering. *Nat. Chem. Biol.* **2016**.

103. Nooren, I. M. A. NEW EMBO MEMBER'S REVIEW: Diversity of protein-protein interactions. *EMBO J.* **2003**, *22*, 3486–3492.

104. Michnick, S. W.; Landry, C. R.; Levy, E. D.; Diss, G.; Ear, P. H.; Kowarzyk, J.; Malleshaiah, M. K.; Messier, V.; Tchekanda, E. Protein-Fragment Complementation Assays for Large-Scale Analysis, Functional Dissection, and Spatiotemporal Dynamic Studies of Protein–Protein Interactions in Living Cells. *Cold Spring Harb. Protoc.* **2016**, *2016*, pdb.top083543.

105. Sternberg, N. Bacteriophage P1 site-specific recombination. III. Strand exchange during recombination at lox sites. *J. Mol. Biol.* **1981**, *150*, 603–608.

106. Van Duyne, G. D. Cre Recombinase. *Microbiol. Spectr.* **2015**, *3*, MDNA3-0014-2014.

107. Feil, R.; Wagner, J.; Metzger, D.; Chambon, P. Regulation of Cre Recombinase Activity by Mutated Estrogen Receptor Ligand-Binding Domains. *Biochem. Biophys. Res. Commun.* **1997**, *237*, 752–757.

108. Casanova, E.; Fehsenfeld, S.; Lemberger, T.; Shimshek, D. R.; Sprengel, R.; Mantamadiotis, T. ER-based double icre fusion protein allows partial recombination in forebrain. *genesis* **2002**, *34*, 208–214.

109. Jullien, N. Regulation of Cre recombinase by ligand-induced complementation of inactive fragments. *Nucleic Acids Res.* **2003**, *31*, 131e–131.

110. Sando, R.; Baumgaertel, K.; Pieraut, S.; Torabi-Rander, N.; Wandless, T. J.; Mayford, M.; Maximov, A. Inducible control of gene expression with destabilized Cre. *Nat. Methods* **2013**, *10*, 1085–1088.

111. Schindler, S. E.; McCall, J. G.; Yan, P.; Hyrc, K. L.; Li, M.; Tucker, C. L.; Lee, J.-M.; Bruchas, M. R.; Diamond, M. I. Photo-activatable Cre recombinase regulates gene expression *in vivo*. *Sci. Rep.* **2015**, *5*, 13627.

112. Jinek, M.; Chylinski, K.; Fonfara, I.; Hauer, M.; Doudna, J. A.; Charpentier, E. A Programmable Dual-RNA-Guided DNA Endonuclease in Adaptive Bacterial Immunity. *Science* **2012**, *337*, 816–821.

113. Cong, L.; Ran, F. A.; Cox, D.; Lin, S.; Barretto, R.; Habib, N.; Hsu, P. D.; Wu, X.; Jiang, W.; Marraffini, L. A.; Zhang, F. Multiplex Genome Engineering Using CRISPR/Cas Systems. *Science* **2013**, *339*, 819–823.

114. Mali, P.; Yang, L.; Esvelt, K. M.; Aach, J.; Guell, M.; DiCarlo, J. E.; Norville, J. E.; Church, G. M. RNA-Guided Human Genome Engineering via Cas9. *Science* **2013**, *339*, 823–826.

115. Hsu, P. D.; Lander, E. S.; Zhang, F. Development and Applications of CRISPR-Cas9 for Genome Engineering. *Cell* **2014**, *157*, 1262–1278.

116. Zetsche, B.; Volz, S. E.; Zhang, F. A split-Cas9 architecture for inducible genome editing and transcription modulation. *Nat. Biotechnol.* **2015**, *33*, 139–142.

117. Wright, A. V.; Sternberg, S. H.; Taylor, D. W.; Staahl, B. T.; Bardales, J. A.; Kornfeld, J. E.; Doudna, J. A. Rational design of a split-Cas9 enzyme complex. *Proc. Natl. Acad. Sci. U. S. A.* **2015**, *112*, 2984–2989.

118. Wah, D. A.; Hirsch, J. A.; Dorner, L. F.; Schildkraut, I.; Aggarwal, A. K. Structure of the multimodular endonuclease FokI bound to DNA. *Nature* **1997**, *388*, 97–100.

119. Liu, H.; Yu, X.; Li, K.; Klejnot, J.; Yang, H.; Lisiero, D.; Lin, C. Photoexcited CRY2 Interacts with CIB1 to Regulate Transcription and Floral Initiation in Arabidopsis. *Science* **2008**, *322*, 1535–1539.

120. Más, P.; Devlin, P. F.; Panda, S.; Kay, S. A. Functional interaction of phytochrome B and cryptochrome 2. *Nature* **2000**, *408*, 207–211.

121. Che, D. L.; Duan, L.; Zhang, K.; Cui, B. The Dual Characteristics of Light-Induced Cryptochrome 2, Homo-oligomerization and Heterodimerization, for Optogenetic Manipulation in Mammalian Cells. *ACS Synth. Biol.* **2015**, *4*, 1124–1135.

122. Kennedy, M. J.; Hughes, R. M.; Peteya, L. A.; Schwartz, J. W.; Ehlers, M. D.; Tucker, C. L. Rapid blue-light–mediated induction of protein interactions in living cells. *Nat. Methods* **2010**, *7*, 973–975.

123. Valon, L.; Marín-Llauradó, A.; Wyatt, T.; Charras, G.; Trepat, X. Optogenetic control of cellular forces and mechanotransduction. *Nat. Commun.* **2017**, *8*, 14396.

124. Zhang, K.; Duan, L.; Ong, Q.; Lin, Z.; Varman, P. M.; Sung, K.; Cui, B. Light-Mediated Kinetic Control Reveals the Temporal Effect of the Raf/MEK/ERK Pathway in PC12 Cell Neurite Outgrowth. *PLoS ONE* **2014**, *9*, e92917.

125. Katsura, Y.; Kubota, H.; Kunida, K.; Kanno, A.; Kuroda, S.; Ozawa, T. An optogenetic system for interrogating the temporal dynamics of Akt. *Sci. Rep.* **2015**, *5*, 14589.

126. Xu, Y.; Nan, D.; Fan, J.; Bogan, J. S.; Toomre, D. Optogenetic activation reveals distinct roles of PI P_3 and Akt in adipocyte insulin action. *J. Cell Sci.* **2016**, *129*, 2085–2095.

127. O'Neill, P. R.; Gautam, N. Subcellular optogenetic inhibition of G proteins generates signaling gradients and cell migration. *Mol. Biol. Cell* **2014**, *25*, 2305–2314.

128. Kotýnková, K.; Su, K.-C.; West, S. C.; Petronczki, M. Plasma Membrane Association but Not Midzone Recruitment of RhoGEF ECT2 Is Essential for Cytokinesis. *Cell Rep.* **2016**, *17*, 2672–2686.

129. Maiuri, P.; Rupprecht, J.-F.; Wieser, S.; Ruprecht, V.; Bénichou, O.; Carpi, N.; Coppey, M.; De Beco, S.; Gov, N.; Heisenberg, C.-P.; Lage Crespo, C.; Lautenschlaeger, F.; Le Berre, M.; Lennon-Dumenil, A.-M.; Raab, M.; Thiam, H.-R.; Piel, M.; Sixt, M.; Voituriez, R. Actin Flows Mediate a Universal Coupling between Cell Speed and Cell Persistence. *Cell* **2015**, *161*, 374–386.

130. Duan, L.; Che, D.; Zhang, K.; Ong, Q.; Guo, S.; Cui, B. Optogenetic Control of Molecular Motors and Organelle Distributions in Cells. *Chem. Biol.* **2015**, *22*, 671–682.

131. Konermann, S.; Brigham, M. D.; Trevino, A.; Hsu, P. D.; Heidenreich, M.; Le Cong; Platt, R. J.; Scott, D. A.; Church, G. M.; Zhang, F. Optical control of mammalian endogenous transcription and epigenetic states. *Nature* **2013**.

132. Nihongaki, Y.; Yamamoto, S.; Kawano, F.; Suzuki, H.; Sato, M. CRISPR-Cas9-based Photoactivatable Transcription System. *Chem. Biol.* **2015**, *22*, 169–174.

133. Polstein, L. R.; Gersbach, C. A. A light-inducible CRISPR-Cas9 system for control of endogenous gene activation. *Nat. Chem. Biol.* **2015**, *11*, 198–200.

134. Kim, J. M.; Lee, M.; Kim, N.; Heo, W. D. Optogenetic toolkit reveals the role of Ca^{2+} sparklets in coordinated cell migration. *Proc. Natl. Acad. Sci. U. S. A.* **2016**, *113*, 5952–5957.

135. Idevall-Hagren, O.; Dickson, E. J.; Hille, B.; Toomre, D. K.; De Camilli, P. Optogenetic control of phosphoinositide metabolism. *Proc. Natl. Acad. Sci. U. S. A.* **2012**, *109*, E2316–E2323.

136. Xiong, D.; Xiao, S.; Guo, S.; Lin, Q.; Nakatsu, F.; Wu, M. Frequency and amplitude control of cortical oscillations by phosphoinositide waves. *Nat. Chem. Biol.* **2016**, *12*, 159–166.

137. Yim, N.; Ryu, S.-W.; Choi, K.; Lee, K. R.; Lee, S.; Choi, H.; Kim, J.; Shaker, M. R.; Sun, W.; Park, J.-H.; Kim, D.; Do Heo, W.; Choi, C. Exosome engineering for efficient intracellular delivery of soluble proteins using optically reversible protein–protein interaction module. *Nat. Commun.* **2016**, *7*, 12277.

138. Bugaj, L. J.; Choksi, A. T.; Mesuda, C. K.; Kane, R. S.; Schaffer, D. V. Optogenetic protein clustering and signaling activation in mammalian cells. *Nat. Methods* **2013**, *10*, 249–252.

139. Taslimi, A.; Vrana, J. D.; Chen, D.; Borinskaya, S.; Mayer, B. J.; Kennedy, M. J.; Tucker, C. L. An optimized optogenetic clustering tool for probing protein interaction and function. *Nat. Commun.* **2014**, *5*, 4925.

140. Nguyen, M. K.; Kim, C. Y.; Kim, J. M.; Park, B. O.; Lee, S.; Park, H.; Heo, W. D. Optogenetic oligomerization of Rab GTPases regulates intracellular membrane trafficking. *Nat. Chem. Biol.* **2016**, *12*, 431–436.

141. Chang, K.-Y.; Woo, D.; Jung, H.; Lee, S.; Kim, S.; Won, J.; Kyung, T.; Park, H.; Kim, N.; Yang, H. W.; Park, J.-Y.; Hwang, E. M.; Kim, D.; Do Heo, W. Light-inducible receptor tyrosine kinases that regulate neurotrophin signalling. *Nat. Commun.* **2014**, *5*.

142. Bugaj, L. J.; Spelke, D. P.; Mesuda, C. K.; Varedi, M.; Kane, R. S.; Schaffer, D. V. Regulation of endogenous transmembrane receptors through optogenetic Cry2 clustering. *Nat. Commun.* **2015**, *6*, 6898.

143. Kim, N.; Kim, J. M.; Lee, M.; Kim, C. Y.; Chang, K.-Y.; Heo, W. D. Spatiotemporal Control of Fibroblast Growth Factor Receptor Signals by Blue Light. *Chem. Biol.* **2014**, *21*, 903–912.

144. Fischer, A.; Warscheid, B.; Weber, W.; Radziwill, G. Optogenetic clustering of CNK1 reveals mechanistic insights in RAF and AKT signalling controlling cell fate decisions. *Sci. Rep.* **2016**, *6*.

145. Kyung, T.; Lee, S.; Kim, J. E.; Cho, T.; Park, H.; Jeong, Y.-M.; Kim, D.; Shin, A.; Kim, S.; Baek, J.; Kim, J.; Kim, N. Y.; Woo, D.; Chae, S.; Kim, C.-H.; Shin, H.-S.; Han, Y.-M.; Kim, D.; Heo, W. D. Optogenetic control of endogenous Ca^{2+} channels *in vivo*. *Nat. Biotechnol.* **2015**, *33*, 1092–1096.

146. Wend, S.; Wagner, H. J.; Müller, K.; Zurbriggen, M. D.; Weber, W.; Radziwill, G. Optogenetic Control of Protein Kinase Activity in Mammalian Cells. *ACS Synth. Biol.* **2014**, *3*, 280–285.

147. Shin, Y.; Berry, J.; Pannucci, N.; Haataja, M. P.; Toettcher, J. E.; Brangwynne, C. P. Spatiotemporal Control of Intracellular Phase Transitions Using Light-Activated optoDroplets. *Cell* **2017**, *168*, 159–171.e14.

148. Lee, S.; Park, H.; Kyung, T.; Kim, N. Y.; Kim, S.; Kim, J.; Heo, W. D. Reversible protein inactivation by optogenetic trapping in cells. *Nat. Methods* **2014**, *11*, 633–636.

149. Anderson, S.; Dragnea, V.; Masuda, S.; Ybe, J.; Moffat, K.; Bauer, C. Structure of a Novel Photoreceptor, the BLUF Domain of AppA from *Rhodobacter sphaeroides*. *Biochemistry (Mosc.)* **2005**, *44*, 7998–8005.

150. Gauden, M.; van Stokkum, I. H. M.; Key, J. M.; Luhrs, D. C.; van Grondelle, R.; Hegemann, P.; Kennis, J. T. M. Hydrogen-bond switching through a radical pair mechanism in a flavin-binding photoreceptor. *Proc. Natl. Acad. Sci. U. S. A.* **2006**, *103*, 10895–10900.

151. Domratcheva, T.; Grigorenko, B. L.; Schlichting, I.; Nemukhin, A. V. Molecular Models Predict Light-Induced Glutamine Tautomerization in BLUF Photoreceptors. *Biophys. J.* **2008**, *94*, 3872–3879.

152. Barends, T. R. M.; Hartmann, E.; Griese, J. J.; Beitlich, T.; Kirienko, N. V.; Ryjenkov, D. A.; Reinstein, J.; Shoeman, R. L.; Gomelsky, M.; Schlichting, I. Structure and mechanism of a bacterial light-regulated cyclic nucleotide phosphodiesterase. *Nature* **2009**, *459*, 1015–1018.

153. Ito, S.; Murakami, A.; Sato, K.; Nishina, Y.; Shiga, K.; Takahashi, T.; Higashi, S.; Iseki, M.; Watanabe, M. Photocycle features of heterologously expressed and assembled eukaryotic flavin-binding BLUF domains of photoactivated adenylyl cyclase (PAC), a blue-light receptor in Euglena gracilis. *Photochem. Photobiol. Sci.* **2005**, *4*, 762.

154. Gomelsky, M.; Klug, G. BLUF: a novel FAD-binding domain involved in sensory transduction in microorganisms. *Trends Biochem. Sci.* **2002**, *27*, 497–500.

155. Schröder-Lang, S.; Schwärzel, M.; Seifert, R.; Strünker, T.; Kateriya, S.; Looser, J.; Watanabe, M.; Kaupp, U. B.; Hegemann, P.; Nagel, G. Fast manipulation of cellular cAMP level by light *in vivo*. *Nat. Methods* **2007**, *4*, 39–42.

156. Stierl, M.; Stumpf, P.; Udwari, D.; Gueta, R.; Hagedorn, R.; Losi, A.; Gartner, W.; Petereit, L.; Efetova, M.; Schwarzel, M.; Oertner, T. G.; Nagel, G.; Hegemann, P. Light Modulation of Cellular cAMP by a Small Bacterial Photoactivated Adenylyl Cyclase, bPAC, of the Soil Bacterium Beggiatoa. *J. Biol. Chem.* **2011**, *286*, 1181–1188.

157. Bellmann, D. Optogenetically induced olfactory stimulation in Drosophila larvae reveales the neuronal basis of odor-aversion behavior. *Front. Behav. Neurosci.* **2010**, *4*.

158. De Marco, R. J.; Groneberg, A. H.; Yeh, C.-M.; Castillo Ramírez, L. A.; Ryu, S. Optogenetic elevation of endogenous glucocorticoid level in larval zebrafish. *Front. Neural Circuits* **2013**, *7*.

159. Weissenberger, S.; Schultheis, C.; Liewald, J. F.; Erbguth, K.; Nagel, G.; Gottschalk, A. PACα- an optogenetic tool for *in vivo* manipulation of cellular cAMP levels, neurotransmitter release, and behavior in Caenorhabditis elegans: Optogenetic manipulation of cAMP levels using PACα. *J. Neurochem.* **2011**, *116*, 616–625.

160. Ryu, M.-H.; Moskvin, O. V.; Siltberg-Liberles, J.; Gomelsky, M. Natural and Engineered Photoactivated Nucleotidyl Cyclases for Optogenetic Applications. *J. Biol. Chem.* **2010**, *285*, 41501–41508.

161. Kim, T.; Folcher, M.; Baba, M. D.-E.; Fussenegger, M. A Synthetic Erectile Optogenetic Stimulator Enabling Blue-Light-Inducible Penile Erection. *Angew. Chem. Int. Ed.* **2015**, *54*, 5933–5938.

162. Jenkins, G. I. Signal transduction in responses to UV-B radiation. *Annu. Rev. Plant Biol.* **2009**, *60*, 407–431.

163. Tilbrook, K.; Arongaus, A. B.; Binkert, M.; Heijde, M.; Yin, R.; Ulm, R. The UVR8 UV-B Photoreceptor: Perception, Signaling and Response. *Arab. Book* **2013**, *11*, e0164.

164. Di Wu; Hu, Q.; Yan, Z.; Chen, W.; Yan, C.; Huang, X.; Zhang, J.; Yang, P.; Deng, H.; Wang, J.; Deng, X.; Shi, Y. Structural basis of ultraviolet-B perception by UVR8. *Nature* **2012**, *484*, 214–219.

165. Rizzini, L.; Favory, J.-J.; Cloix, C.; Faggionato, D.; O'Hara, A.; Kaiserli, E.; Baumeister, R.; Schafer, E.; Nagy, F.; Jenkins, G. I.; Ulm, R. Perception of UV-B by the Arabidopsis UVR8 Protein. *Science* **2011**, *332*, 103–106.

166. Christie, J. M.; Arvai, A. S.; Baxter, K. J.; Heilmann, M.; Pratt, A. J.; O'Hara, A.; Kelly, S. M.; Hothorn, M.; Smith, B. O.; Hitomi, K.; Jenkins, G. I.; Getzoff, E. D. Plant UVR8 Photoreceptor Senses UV-B by Tryptophan-Mediated Disruption of Cross-Dimer Salt Bridges. *Science* **2012**, *335*, 1492–1496.

167. Crefcoeur, R. P.; Yin, R.; Ulm, R.; Halazonetis, T. D. Ultraviolet-B-mediated induction of protein–protein interactions in mammalian cells. *Nat. Commun.* **2013**, *4*, 1779.

168. Müller, K.; Engesser, R.; Timmer, J.; Zurbriggen, M. D.; Weber, W. Orthogonal Optogenetic Triple-Gene Control in Mammalian Cells. *ACS Synth. Biol.* **2014**, *3*, 796–801.

169. Chen, D.; Gibson, E. S.; Kennedy, M. J. A light-triggered protein secretion system. *J. Cell Biol.* **2013**, *201*, 631–640.

170. Kumauchi, M.; Hara, M. T.; Stalcup, P.; Xie, A.; Hoff, W. D. Identification of Six New Photoactive Yellow Proteins—Diversity and Structure-Function Relationships in a Bacterial Blue Light Photoreceptor. *Photochem. Photobiol.* **2008**, *84*, 956–969.

171. Imamoto, Y.; Kataoka, M. Structure and Photoreaction of Photoactive Yellow Protein, a Structural Prototype of the PAS Domain Superfamily†. *Photochem. Photobiol.* **2007**, *83*, 40–49.

172. Harigai, M.; Imamoto, Y.; Kamikubo, H.; Yamazaki, Y.; Kataoka, M. Role of an N-Terminal Loop in the Secondary Structural Change of Photoactive Yellow Protein. *Biochemistry (Mosc.)* **2003**, *42*, 13893–13900.

173. van der Horst, M. A.; van Stokkum, I. H.; Crielaard, W.; Hellingwerf, K. J. The role of the N-terminal domain of photoactive yellow protein in the transient partial unfolding during signalling state formation. *FEBS Lett.* **2001**, *497*, 26–30.

174. Hendriks, J.; Gensch, T.; Hviid, L.; van der Horst, M. A.; Hellingwerf, K. J.; van Thor, J. J. Transient Exposure of Hydrophobic Surface in the Photoactive Yellow Protein Monitored with Nile Red. *Biophys. J.* **2002**, *82*, 1632–1643.

175. Pande, K.; Hutchison, C. D. M.; Groenhof, G.; Aquila, A.; Robinson, J. S.; Tenboer, J.; Basu, S.; Boutet, S.; DePonte, D. P.; Liang, M.; White, T. A.; Zatsepin, N. A.; Yefanov, O.; Morozov, D.; Oberthuer, D.; Gati, C.; Subramanian, G.; James, D.; Zhao, Y.; Koralek, J.; Brayshaw, J.; Kupitz, C.; Conrad, C.; Roy-Chowdhury, S.; Coe, J. D.; Metz, M.; Xavier, P. L.; Grant, T. D.; Koglin, J. E.; Ketawala, G.; Fromme, R.; rajer, V.; Henning, R.; Spence, J. C. H.; Ourmazd, A.; Schwander, P.; Weierstall, U.; Frank, M.; Fromme, P.; Barty, A.; Chapman, H. N.; Moffat, K.; van Thor, J. J.; Schmidt, M. Femtosecond structural dynamics drives the trans/cis isomerization in photoactive yellow protein. *Science* **2016**, *352*, 725–729.

176. Schotte, F.; Cho, H. S.; Kaila, V. R. I.; Kamikubo, H.; Dashdorj, N.; Henry, E. R.; Graber, T. J.; Henning, R.; Wulff, M.; Hummer, G.; Kataoka, M.; Anfinrud, P. A. Watching a signaling protein function in real time via 100-ps time-resolved Laue crystallography. *Proc. Natl. Acad. Sci. U. S. A.* **2012**, *109*, 19256–19261.

177. Morgan, S.-A.; Woolley, G. A. A photoswitchable DNA-binding protein based on a truncated GCN4-photoactive yellow protein chimera. *Photochem. Photobiol. Sci.* **2010**, *9*, 1320.

178. Fan, H. Y.; Morgan, S.-A.; Brechun, K. E.; Chen, Y.-Y.; Jaikaran, A. S. I.; Woolley, G. A. Improving a Designed Photocontrolled DNA-Binding Protein. *Biochemistry (Mosc.)* **2011**, *50*, 1226–1237.

179. Morgan, S.-A.; Al-Abdul-Wahid, S.; Woolley, G. A. Structure-Based Design of a Photocontrolled DNA Binding Protein. *J. Mol. Biol.* **2010**, *399*, 94–112.

180. Ali, A. M.; Reis, J. M.; Xia, Y.; Rashid, A. J.; Mercaldo, V.; Walters, B. J.; Brechun, K. E.; Borisenko, V.; Josselyn, S. A.; Karanicolas, J.; Woolley, G. A. Optogenetic Inhibitor of the Transcription Factor CREB. *Chem. Biol.* **2015**, *22*, 1531–1539.

181. Kyndt, J. A.; Hurley, J. K.; Devreese, B.; Meyer, T. E.; Cusanovich, M. A.; Tollin, G.; Van Beeumen, J. J. *Rhodobacter capsulatus* Photoactive Yellow Protein: Genetic Context, Spectral and Kinetics Characterization, and Mutagenesis. *Biochemistry (Mosc.)* **2004**, *43*, 1809–1820.

182. Haker, A.; Hendriks, J.; Gensch, T.; Hellingwerf, K.; Crielaard, W. Isolation, reconstitution and functional characterisation of the Rhodobacter sphaeroides photoactive yellow protein. *FEBS Lett.* **2000**, *486*, 52–56.

183. Haker, A. The Two Photocycles of Photoactive Yellow Protein from Rhodobacter sphaeroides. *J. Biol. Chem.* **2003**, *278*, 8442–8451.

184. Shimomura, O.; Johnson, F. H.; Saiga, Y. Extraction, Purification and Properties of Aequorin, a Bioluminescent Protein from the Luminous Hydromedusan, Aequorea. *J. Cell. Comp. Physiol.* **1962**, *59*, 223–239.

185. Morise, H.; Shimomura, O.; Johnson, F. H.; Winant, J. Intermolecular energy transfer in the bioluminescent system of Aequorea. *Biochemistry (Mosc.)* **1974**, *13*, 2656–2662.

186. Shimomura, O. Structure of the chromophore of *Aequorea* green fluorescent protein. *FEBS Lett.* **1979**, *104*, 220–222.

187. Cody, C. W.; Prasher, D. C.; Westler, W. M.; Prendergast, F. G.; Ward, W. W. Chemical structure of the hexapeptide chromophore of the Aequorea green-fluorescent protein. *Biochemistry (Mosc.)* **1993**, *32*, 1212–1218.

188. Prasher, D. C.; Eckenrode, V. K.; Ward, W. W.; Prendergast, F. G.; Cormier, M. J. Primary structure of the Aequorea victoria green-fluorescent protein. *Gene* **1992**, *111*, 229–233.

189. Barondeau, D. P.; Putnam, C. D.; Kassmann, C. J.; Tainer, J. A.; Getzoff, E. D. Mechanism and energetics of green fluorescent protein chromophore synthesis revealed by trapped intermediate structures. *Proc. Natl. Acad. Sci. U. S. A.* **2003**, *100*, 12111–12116.

190. Barondeau, D. P.; Tainer, J. A.; Getzoff, E. D. Structural Evidence for an Enolate Intermediate in GFP Fluorophore Biosynthesis. *J. Am. Chem. Soc.* **2006**, *128*, 3166–3168.

191. Zhang, L.; Patel, H. N.; Lappe, J. W.; Wachter, R. M. Reaction Progress of Chromophore Biogenesis in Green Fluorescent Protein. *J. Am. Chem. Soc.* **2006**, *128*, 4766–4772.

192. Rosenow, M. A.; Patel, H. N.; Wachter, R. M. Oxidative Chemistry in the GFP Active Site Leads to Covalent Cross-Linking of a Modified Leucine Side Chain with a Histidine Imidazole: Implications for the Mechanism of Chromophore Formation. *Biochemistry (Mosc.)* **2005**, *44*, 8303–8311.

193. Rosenow, M. A.; Huffman, H. A.; Phail, M. E.; Wachter, R. M. The Crystal Structure of the Y66L Variant of Green Fluorescent Protein Supports a Cyclization−Oxidation−Dehydration Mechanism for Chromophore Maturation. *Biochemistry (Mosc.)* **2004**, *43*, 4464–4472.

194. Chalfie, M.; Tu, Y.; Euskirchen, G.; Ward, W.; Prasher, D. Green fluorescent protein as a marker for gene expression. *Science* **1994**, *263*, 802–805.

195. Heim, R.; Prasher, D. C.; Tsien, R. Y. Wavelength mutations and posttranslational autoxidation of green fluorescent protein. *Proc. Natl. Acad. Sci. U. S. A.* **1994**, *91*, 12501–12504.

196. Eales, K. L.; Hollinshead, K. E. R.; Tennant, D. A. Hypoxia and metabolic adaptation of cancer cells. *Oncogenesis* **2016**, *5*, e190.

197. Hall-Stoodley, L.; Costerton, J. W.; Stoodley, P. Bacterial biofilms: from the Natural environment to infectious diseases. *Nat. Rev. Microbiol.* **2004**, *2*, 95–108.

198. Heim, R.; Cubitt, A. B.; Tsien, R. Y. Improved green fluorescence. *Nature* **1995**, *373*, 663–664.

199. Cubitt, A. B.; Heim, R.; Adams, S. R.; Boyd, A. E.; Gross, L. A.; Tsien, R. Y. Understanding, improving and using green fluorescent proteins. *Trends Biochem. Sci.* **1995**, *20*, 448–455.

200. Cormack, B. P.; Valdivia, R. H.; Falkow, S. FACS-optimized mutants of the green fluorescent protein (GFP). *Gene* **1996**, *173*, 33–38.

201. Heim, R.; Tsien, R. Y. Engineering green fluorescent protein for improved brightness, longer wavelengths and fluorescence resonance energy transfer. *Curr. Biol. CB* **1996**, *6*, 178–182.

202. Ormö, M.; Cubitt, A. B.; Kallio, K.; Gross, L. A.; Tsien, R. Y.; Remington, S. J. Crystal structure of the Aequorea victoria green fluorescent protein. *Science* **1996**, *273*, 1392–1395.

203. Alieva, N. O.; Konzen, K. A.; Field, S. F.; Meleshkevitch, E. A.; Hunt, M. E.; Beltran-Ramirez, V.; Miller, D. J.; Wiedenmann, J.; Salih, A.; Matz, M. V. Diversity and Evolution of Coral Fluorescent Proteins. *PLoS ONE* **2008**, *3*, e2680.

204. Yang, F.; Moss, L. G.; Phillips, G. N. The molecular structure of green fluorescent protein. *Nat. Biotechnol.* **1996**, *14*, 1246–1251.

205. Phillips, G. N. Structure and dynamics of green fluorescent protein. *Curr. Opin. Struct. Biol.* **1997**, *7*, 821–827.

206. Mizuno, H.; Sawano, A.; Eli, P.; Hama, H.; Miyawaki, A. Red Fluorescent Protein from *Discosoma* as a Fusion Tag and a Partner for Fluorescence Resonance Energy Transfer. *Biochemistry (Mosc.)* **2001**, *40*, 2502–2510.

207. Lauf, U.; Lopez, P.; Falk, M. M. Expression of fluorescently tagged connexins: a novel approach to rescue function of oligomeric DsRed-tagged proteins. *FEBS Lett.* **2001**, *498*, 11–15.

208. Campbell, R. E.; Tour, O.; Palmer, A. E.; Steinbach, P. A.; Baird, G. S.; Zacharias, D. A.; Tsien, R. Y. A monomeric red fluorescent protein. *Proc. Natl. Acad. Sci. U. S. A.* **2002**, *99*, 7877–7882.

209. Baird, G. S.; Zacharias, D. A.; Tsien, R. Y. Biochemistry, mutagenesis, and oligomerization of DsRed, a red fluorescent protein from coral. *Proc. Natl. Acad. Sci. U. S. A.* **2000**, *97*, 11984–11989.

210. Shaner, N. C.; Steinbach, P. A.; Tsien, R. Y. A guide to choosing fluorescent proteins. *Nat. Methods* **2005**, *2*, 905–909.

211. Shaner, N. C.; Patterson, G. H.; Davidson, M. W. Advances in fluorescent protein technology. *J. Cell Sci.* **2007**, *120*, 4247–4260.

212. Ai, H.; Baird, M. A.; Shen, Y.; Davidson, M. W.; Campbell, R. E. Engineering and characterizing monomeric fluorescent proteins for live-cell imaging applications. *Nat. Protoc.* **2014**, *9*, 910–928.

213. Adam, V.; Berardozzi, R.; Byrdin, M.; Bourgeois, D. Phototransformable fluorescent proteins: Future challenges. *Curr. Opin. Chem. Biol.* **2014**, *20*, 92–102.

214. van Thor, J. J.; Gensch, T.; Hellingwerf, K. J.; Johnson, L. N. Phototransformation of green fluorescent protein with UV and visible light leads to decarboxylation of glutamate 222. *Nat. Struct. Biol.* **2002**, *9*, 37–41.

215. Bell, A. F.; Stoner-Ma, D.; Wachter, R. M.; Tonge, P. J. Light-driven decarboxylation of wild-type green fluorescent protein. *J. Am. Chem. Soc.* **2003**, *125*, 6919–6926.

216. Mizuno, H.; Mal, T. K.; Tong, K. I.; Ando, R.; Furuta, T.; Ikura, M.; Miyawaki, A. Photo-Induced Peptide Cleavage in the Green-to-Red Conversion of a Fluorescent Protein. *Mol. Cell* **2003**, *12*, 1051–1058.

217. Tsutsui, H.; Shimizu, H.; Mizuno, H.; Nukina, N.; Furuta, T.; Miyawaki, A. The E1 Mechanism in Photo-Induced β-Elimination Reactions for Green-to-Red Conversion of Fluorescent Proteins. *Chem. Biol.* **2009**, *16*, 1140–1147.

218. Andresen, M.; Wahl, M. C.; Stiel, A. C.; Grater, F.; Schafer, L. V.; Trowitzsch, S.; Weber, G.; Eggeling, C.; Grubmuller, H.; Hell, S. W.; Jakobs, S. Structure and mechanism of the reversible photoswitch of a fluorescent protein. *Proc. Natl. Acad. Sci. U. S. A.* **2005**, *102*, 13070–13074.

219. Andresen, M.; Stiel, A. C.; Trowitzsch, S.; Weber, G.; Eggeling, C.; Wahl, M. C.; Hell, S. W.; Jakobs, S. Structural basis for reversible photoswitching in Dronpa. *Proc. Natl. Acad. Sci. U. S. A.* **2007**, *104*, 13005–13009.

220. Ando, R. Regulated Fast Nucleocytoplasmic Shuttling Observed by Reversible Protein Highlighting. *Science* **2004**, *306*, 1370–1373.

221. Ando, R.; Hama, H.; Yamamoto-Hino, M.; Mizuno, H.; Miyawaki, A. An optical marker based on the UV-induced green-to-red photoconversion of a fluorescent protein. *Proc. Natl. Acad. Sci. U. S. A.* **2002**, *99*, 12651–12656.

222. Lippincott-Schwartz, J. Development and Use of Fluorescent Protein Markers in Living Cells. *Science* **2003**, *300*, 87–91.

223. Betzig, E.; Patterson, G. H.; Sougrat, R.; Lindwasser, O. W.; Olenych, S.; Bonifacino, J. S.; Davidson, M. W.; Lippincott-Schwartz, J.; Hess, H. F. Imaging Intracellular Fluorescent Proteins at Nanometer Resolution. *Science* **2006**, *313*, 1642–1645.

224. Hess, S. T.; Girirajan, T. P. K.; Mason, M. D. Ultra-High Resolution Imaging by Fluorescence Photoactivation Localization Microscopy. *Biophys. J.* **2006**, *91*, 4258–4272.

225. Henderson, J. N.; Ai, H. -w.; Campbell, R. E.; Remington, S. J. Structural basis for reversible photobleaching of a green fluorescent protein homologue. *Proc. Natl. Acad. Sci. U. S. A.* **2007**, *104*, 6672–6677.

226. Adam, V.; Lelimousin, M.; Boehme, S.; Desfonds, G.; Nienhaus, K.; Field, M. J.; Wiedenmann, J.; McSweeney, S.; Nienhaus, G. U.; Bourgeois, D. Structural characterization of IrisFP, an optical highlighter undergoing multiple photo-induced transformations. *Proc. Natl. Acad. Sci. U. S. A.* **2008**, *105*, 18343–18348.

227. Mizuno, H.; Mal, T. K.; Walchli, M.; Kikuchi, A.; Fukano, T.; Ando, R.; Jeyakanthan, J.; Taka, J.; Shiro, Y.; Ikura, M.; Miyawaki, A. Light-dependent regulation of structural flexibility in a photochromic fluorescent protein. *Proc. Natl. Acad. Sci. U. S. A.* **2008**, *105*, 9227–9232.

228. Zhou, X. X.; Chung, H. K.; Lam, A. J.; Lin, M. Z. Optical Control of Protein Activity by Fluorescent Protein Domains. *Science* **2012**, *338*, 810–814.

229. Zhou, X. X.; Fan, L. Z.; Li, P.; Shen, K.; Lin, M. Z. Optical control of cell signaling by single-chain photoswitchable kinases. *Science* **2017**, *355*, 836–842.

230. Llopis, J.; McCaffery, J. M.; Miyawaki, A.; Farquhar, M. G.; Tsien, R. Y. Measurement of cytosolic, mitochondrial, and Golgi pH in single living cells with green fluorescent proteins. *Proc. Natl. Acad. Sci. U. S. A.* **1998**, *95*, 6803–6808.

231. Wachter, R. M.; Yarbrough, D.; Kallio, K.; Remington, S. J. Crystallographic and energetic analysis of binding of selected anions to the yellow variants of green fluorescent protein. *J. Mol. Biol.* **2000**, *301*, 157–171.

232. Jayaraman, S. Mechanism and Cellular Applications of a Green Fluorescent Protein-based Halide Sensor. *J. Biol. Chem.* **2000**, *275*, 6047–6050.

233. Pelletier, J. N.; Campbell-Valois, F. X.; Michnick, S. W. Oligomerization domain-directed reassembly of active dihydrofolate reductase from rationally designed fragments. *Proc. Natl. Acad. Sci. U. S. A.* **1998**, *95*, 12141–12146.

234. Galarneau, A.; Primeau, M.; Trudeau, L.-E.; Michnick, S. W. β-Lactamase protein fragment complementation assays as *in vivo* and *in vitro* sensors of protein–protein interactions. *Nat. Biotechnol.* **2002**, *20*, 619–622.

235. Rossi, F.; Charlton, C. A.; Blau, H. M. Monitoring protein-protein interactions in intact eukaryotic cells by beta-galactosidase complementation. *Proc. Natl. Acad. Sci. U. S. A.* **1997**, *94*, 8405–8410.

236. Martell, J. D.; Yamagata, M.; Deerinck, T. J.; Phan, S.; Kwa, C. G.; Ellisman, M. H.; Sanes, J. R.; Ting, A. Y. A split horseradish peroxidase for the detection of intercellular protein–protein interactions and sensitive visualization of synapses. *Nat. Biotechnol.* **2016**, *34*, 774–780.

237. Ozawa, T.; Kaihara, A.; Sato, M.; Tachihara, K.; Umezawa, Y. Split Luciferase as an Optical Probe for Detecting Protein−Protein Interactions in Mammalian Cells Based on Protein Splicing. *Anal. Chem.* **2001**, *73*, 2516–2521.

238. Paulmurugan, R.; Gambhir, S. S. Monitoring Protein−Protein Interactions Using Split Synthetic Renilla Luciferase Protein-Fragment-Assisted Complementation. *Anal. Chem.* **2003**, *75*, 1584–1589.

239. Remy, I.; Michnick, S. W. A highly sensitive protein-protein interaction assay based on Gaussia luciferase. *Nat. Methods* **2006**, *3*, 977–979.

240. Dixon, A. S.; Schwinn, M. K.; Hall, M. P.; Zimmerman, K.; Otto, P.; Lubben, T. H.; Butler, B. L.; Binkowski, B. F.; Machleidt, T.; Kirkland, T. A.; Wood, M. G.; Eggers, C. T.; Encell, L. P.; Wood, K. V. NanoLuc Complementation Reporter Optimized for Accurate Measurement of Protein Interactions in Cells. *ACS Chem. Biol.* **2016**, *11*, 400–408.

241. Fields, S.; Song, O. A novel genetic system to detect protein﷿protein interactions. *Nature* **1989**, *340*, 245–246.

242. Ghosh, I.; Hamilton, A. D.; Regan, L. Antiparallel Leucine Zipper-Directed Protein Reassembly: Application to the Green Fluorescent Protein. *J. Am. Chem. Soc.* **2000**, *122*, 5658–5659.

243. Kerppola, T. K. Bimolecular Fluorescence Complementation (BiFC) Analysis as a Probe of Protein Interactions in Living Cells. *Annu. Rev. Biophys.* **2008**, *37*, 465–487.

244. Kerppola, T. K. Visualization of molecular interactions by fluorescence complementation. *Nat. Rev. Mol. Cell Biol.* **2006**, *7*, 449–456.

245. Morell, M.; Espargaro, A.; Aviles, F. X.; Ventura, S. Study and selection of *in vivo* protein interactions by coupling bimolecular fluorescence complementation and flow cytometry. *Nat. Protoc.* **2008**, *3*, 22–33.

246. Shyu, Y. J.; Liu, H.; Deng, X.; Hu, C.-D. Identification of new fluorescent protein fragments for bimolecular fluorescence complementation analysis under physiological conditions. *BioTechniques* **2006**, *40*, 61–66.

247. Ohashi, K.; Kiuchi, T.; Shoji, K.; Sampei, K.; Mizuno, K. Visualization of cofilin-actin and Ras-Raf interactions by bimolecular fluorescence complementation assays using a new pair of split Venus fragments. *BioTechniques* **2012**, *52*.

248. Jach, G.; Pesch, M.; Richter, K.; Frings, S.; Uhrig, J. F. An improved mRFP1 adds red to bimolecular fluorescence complementation. *Nat. Methods* **2006**, *3*, 597–600.

249. Fan, J.-Y.; Cui, Z.-Q.; Wei, H.-P.; Zhang, Z.-P.; Zhou, Y.-F.; Wang, Y.-P.; Zhang, X.-E. Split mCherry as a new red bimolecular fluorescence complementation system for visualizing protein–protein interactions in living cells. *Biochem. Biophys. Res. Commun.* **2008**, *367*, 47–53.

250. Chu, J.; Zhang, Z.; Zheng, Y.; Yang, J.; Qin, L.; Lu, J.; Huang, Z.-L.; Zeng, S.; Luo, Q. A novel far-red bimolecular fluorescence complementation system that allows for efficient visualization of protein interactions under physiological conditions. *Biosens. Bioelectron.* **2009**, *25*, 234–239.

251. Alford, S. C.; Abdelfattah, A. S.; Ding, Y.; Campbell, R. E. A Fluorogenic Red Fluorescent Protein Heterodimer. *Chem. Biol.* **2012**, *19*, 353–360.

252. Alford, S. C.; Ding, Y.; Simmen, T.; Campbell, R. E. Dimerization-Dependent Green and Yellow Fluorescent Proteins. *ACS Synth. Biol.* **2012**, *1*, 569–575.

253. Ding, Y.; Li, J.; Enterina, J. R.; Shen, Y.; Zhang, I.; Tewson, P. H.; Mo, G. C. H.; Zhang, J.; Quinn, A. M.; Hughes, T. E.; Maysinger, D.; Alford, S. C.; Zhang, Y.; Campbell, R. E. Ratiometric biosensors based on dimerization-dependent fluorescent protein exchange. *Nat. Methods* **2015**, *12*, 195–198.

254. Campbell, R. E. Fluorescent-Protein-Based Biosensors: Modulation of Energy Transfer as a Design Principle. *Anal. Chem.* **2009**, *81*, 5972–5979.

255. Lam, A. J.; St-Pierre, F.; Gong, Y.; Marshall, J. D.; Cranfill, P. J.; Baird, M. A.; McKeown, M. R.; Wiedenmann, J.; Davidson, M. W.; Schnitzer, M. J.; Tsien, R. Y.; Lin, M. Z. Improving FRET dynamic range with bright green and red fluorescent proteins. *Nat. Methods* **2012**, *9*, 1005–1012.

256. Alford, S. C.; Wu, J.; Zhao, Y.; Campbell, R. E.; Knöpfel, T. Optogenetic reporters. *Biol. Cell* **2013**, *105*, 14–29.

257. Topell, S.; Hennecke, J.; Glockshuber, R. Circularly permuted variants of the green fluorescent protein. *FEBS Lett.* **1999**, *457*, 283–289.

258. Nagai, T.; Sawano, A.; Park, E. S.; Miyawaki, A. Circularly permuted green fluorescent proteins engineered to sense Ca^{2+}. *Proc. Natl. Acad. Sci. U. S. A.* **2001**, *98*, 3197–3202.

259. Carlson, H. J.; Cotton, D. W.; Campbell, R. E. Circularly permuted monomeric red fluorescent proteins with new termini in the β-sheet. *Protein Sci.* **2010**, *19*, 1490–1499.

260. Chen, T.-W.; Wardill, T. J.; Sun, Y.; Pulver, S. R.; Renninger, S. L.; Baohan, A.; Schreiter, E. R.; Kerr, R. A.; Orger, M. B.; Jayaraman, V.; Looger, L. L.; Svoboda, K.; Kim, D. S. Ultrasensitive fluorescent proteins for imaging neuronal activity. *Nature* **2013**, *499*, 295–300.

261. Zhao, Y.; Araki, S.; Wu, J.; Teramoto, T.; Chang, Y.-F.; Nakano, M.; Abdelfattah, A. S.; Fujiwara, M.; Ishihara, T.; Nagai, T.; Campbell, R. E. An Expanded Palette of Genetically Encoded Ca^{2+} Indicators. *Science* **2011**, *333*, 1888–1891.

262. St-Pierre, F.; Marshall, J. D.; Yang, Y.; Gong, Y.; Schnitzer, M. J.; Lin, M. Z. High-fidelity optical reporting of neuronal electrical activity with an ultrafast fluorescent voltage sensor. *Nat. Neurosci.* **2014**, *17*, 884–889.

263. Berg, J.; Hung, Y. P.; Yellen, G. A genetically encoded fluorescent reporter of ATP:ADP ratio. *Nat. Methods* **2009**, *6*, 161–166.

264. Tantama, M.; Martínez-François, J. R.; Mongeon, R.; Yellen, G. Imaging energy status in live cells with a fluorescent biosensor of the intracellular ATP-to-ADP ratio. *Nat. Commun.* **2013**, *4*.

265. Marvin, J. S.; Borghuis, B. G.; Tian, L.; Cichon, J.; Harnett, M. T.; Akerboom, J.; Gordus, A.; Renninger, S. L.; Chen, T.-W.; Bargmann, C. I.; Orger, M. B.; Schreiter, E. R.; Demb, J. B.; Gan, W.-B.; Hires, S. A.; Looger, L. L. An optimized fluorescent probe for visualizing glutamate neurotransmission. *Nat. Methods* **2013**, *10*, 162–170.

266. Rockwell, N. C.; Su, Y.-S.; Lagarias, J. C. Phytochrome structure and signaling mechanisms. *Annu. Rev. Plant Biol.* **2006**, *57*, 837–858.

267. Weissleder, R. A clearer vision for *in vivo* imaging. *Nat. Biotechnol.* **2001**, *19*, 316–317.

268. Sharrock, R. A. The phytochrome red/far-red photoreceptor superfamily. *Genome Biol.* **2008**, *9*, 230.

269. Ulijasz, A. T.; Vierstra, R. D. Phytochrome structure and photochemistry: recent advances toward a complete molecular picture. *Curr. Opin. Plant Biol.* **2011**, *14*, 498–506.

270. Li, J.; Li, G.; Wang, H.; Wang Deng, X. Phytochrome Signaling Mechanisms. *Arab. Book* **2011**, *9*, e0148.

271. Levskaya, A.; Chevalier, A. A.; Tabor, J. J.; Simpson, Z. B.; Lavery, L. A.; Levy, M.; Davidson, E. A.; Scouras, A.; Ellington, A. D.; Marcotte, E. M.; Voigt, C. A. Synthetic biology: Engineering Escherichia coli to see light. *Nature* **2005**, *438*, 441–442.

272. Levskaya, A.; Weiner, O. D.; Lim, W. A.; Voigt, C. A. Spatiotemporal control of cell signalling using a light-switchable protein interaction. *Nature* **2009**, *461*, 997–1001.

273. Tabor, J. J.; Levskaya, A.; Voigt, C. A. Multichromatic Control of Gene Expression in Escherichia coli. *J. Mol. Biol.* **2011**, *405*, 315–324.

274. Olson, E. J.; Hartsough, L. A.; Landry, B. P.; Shroff, R.; Tabor, J. J. Characterizing bacterial gene circuit dynamics with optically programmed gene expression signals. *Nat. Methods* **2014**, *11*, 449–455.

275. Muller, K.; Engesser, R.; Metzger, S.; Schulz, S.; Kampf, M. M.; Busacker, M.; Steinberg, T.; Tomakidi, P.; Ehrbar, M.; Nagy, F.; Timmer, J.; Zubriggen, M. D.; Weber, W. A red/far-red light-responsive bi-stable toggle switch to control gene expression in mammalian cells. *Nucleic Acids Res.* **2013**, *41*, e77–e77.

276. Milias-Argeitis, A.; Summers, S.; Stewart-Ornstein, J.; Zuleta, I.; Pincus, D.; El-Samad, H.; Khammash, M.; Lygeros, J. In silico feedback for *in vivo* regulation of a gene expression circuit. *Nat. Biotechnol.* **2011**, *29*, 1114–1116.

277. Shimizu-Sato, S.; Huq, E.; Tepperman, J. M.; Quail, P. H. A light-switchable gene promoter system. *Nat. Biotechnol.* **2002**, *20*, 1041–1044.

278. Tyszkiewicz, A. B.; Muir, T. W. Activation of protein splicing with light in yeast. *Nat. Methods* **2008**.

279. Buckley, C. E.; Moore, R. E.; Reade, A.; Goldberg, A. R.; Weiner, O. D.; Clarke, J. D. W. Reversible Optogenetic Control of Subcellular Protein Localization in a Live Vertebrate Embryo. *Dev. Cell* **2016**, *36*, 117–126.

280. Beyer, H. M.; Juillot, S.; Herbst, K.; Samodelov, S. L.; Müller, K.; Schamel, W. W.; Römer, W.; Schäfer, E.; Nagy, F.; Strähle, U.; Weber, W.; Zurbriggen, M. D. Red Light-Regulated Reversible Nuclear Localization of Proteins in Mammalian Cells and Zebrafish. *ACS Synth. Biol.* **2015**, *4*, 951–958.

281. Gomez, E. J.; Gerhardt, K.; Judd, J.; Tabor, J. J.; Suh, J. Light-Activated Nuclear Translocation of Adeno-Associated Virus Nanoparticles Using Phytochrome B for Enhanced, Tunable, and Spatially Programmable Gene Delivery. *ACS Nano* **2016**, *10*, 225–237.

282. Yang, X.; Jost, A. P.-T.; Weiner, O. D.; Tang, C. A light-inducible organelle-targeting system for dynamically activating and inactivating signaling in budding yeast. *Mol. Biol. Cell* **2013**, *24*, 2419–2430.

283. Leung, D. W.; Otomo, C.; Chory, J.; Rosen, M. K. Genetically encoded photoswitching of actin assembly through the Cdc42-WASP-Arp2/3 complex pathway. *Proc. Natl. Acad. Sci. U. S. A.* **2008**, *105*, 12797–12802.

284. Toettcher, J. E.; Weiner, O. D.; Lim, W. A. Using Optogenetics to Interrogate the Dynamic Control of Signal Transmission by the Ras/Erk Module. *Cell* **2013**, *155*, 1422–1434.

285. Toettcher, J. E.; Gong, D.; Lim, W. A.; Weiner, O. D. Light-based feedback for controlling intracellular signaling dynamics. *Nat. Methods* **2011**, *8*, 837–839.

286. Miura, G. Optogenetics: Follow the PIF. *Nat. Chem. Biol.* **2016**, *12*, 125–125.

287. Bhoo, S.-H.; Davis, S. J.; Walker, J.; Karniol, B.; Vierstra, R. D. Bacteriophytochromes are photochromic histidine kinases using a biliverdin chromophore. *Nature* **2001**, *414*, 776–779.

288. Shu, X.; Royant, A.; Lin, M. Z.; Aguilera, T. A.; Lev-Ram, V.; Steinbach, P. A.; Tsien, R. Y. Mammalian Expression of Infrared Fluorescent Proteins Engineered from a Bacterial Phytochrome. *Science* **2009**, *324*, 804–807.

289. Shcherbakova, D. M.; Baloban, M.; Verkhusha, V. V. Near-infrared fluorescent proteins engineered from bacterial phytochromes. *Curr. Opin. Chem. Biol.* **2015**, *27*, 52–63.

290. Yu, D.; Baird, M. A.; Allen, J. R.; Howe, E. S.; Klassen, M. P.; Reade, A.; Makhijani, K.; Song, Y.; Liu, S.; Murthy, Z.; Zhang, S.-Q.; Weiner, O. D.; Kornberg, T. B.; Jan, Y.-N.; Davidson, M. W.; Shu, X. A naturally monomeric infrared fluorescent protein for protein labeling *in vivo*. *Nat. Methods* **2015**, *12*, 763–765.

291. Shcherbakova, D. M.; Baloban, M.; Emelyanov, A. V.; Brenowitz, M.; Guo, P.; Verkhusha, V. V. Bright monomeric near-infrared fluorescent proteins as tags and biosensors for multiscale imaging. *Nat. Commun.* **2016**, *7*, 12405.

292. Bellini, D.; Papiz, M. Z. Structure of a Bacteriophytochrome and Light-Stimulated Protomer Swapping with a Gene Repressor. *Structure* **2012**, *20*, 1436–1446.

293. Kaberniuk, A. A.; Shemetov, A. A.; Verkhusha, V. V. A bacterial phytochrome-based optogenetic system controllable with near-infrared light. *Nat. Methods* **2016**, *13*, 591–597.

294. Redchuk, T. A.; Omelina, E. S.; Chernov, K. G.; Verkhusha, V. V. Near-infrared optogenetic pair for protein regulation and spectral multiplexing. *Nat. Chem. Biol.* **2017**.

295. McEvoy, A. L.; Hoi, H.; Bates, M.; Platonova, E.; Cranfill, P. J.; Baird, M. A.; Davidson, M. W.; Ewers, H.; Liphardt, J.; Campbell, R. E. mMaple: A Photoconvertible Fluorescent Protein for Use in Multiple Imaging Modalities. *PLoS ONE* **2012**, *7*, e51314.

296. Ai, H.; Henderson, J. N.; Remington, S. J.; Campbell, R. E. Directed evolution of a monomeric, bright and photostable version of *Clavularia* cyan fluorescent protein: structural characterization and applications in fluorescence imaging. *Biochem. J.* **2006**, *400*, 531–540.

297. Hoi, H.; Matsuda, T.; Nagai, T.; Campbell, R. E. Highlightable Ca^{2+} Indicators for Live Cell Imaging. *J. Am. Chem. Soc.* **2013**, *135*, 46–49.

298. Fritz, R. D.; Letzelter, M.; Reimann, A.; Martin, K.; Fusco, L.; Ritsma, L.; Ponsioen, B.; Fluri, E.; Schulte-Merker, S.; van Rheenen, J.; Pertz, O. A versatile toolkit to produce sensitive FRET biosensors to visualize signaling in time and space. *Sci. Signal.* **2013**, *6*, rs12.

299. Kent, K. P.; Oltrogge, L. M.; Boxer, S. G. Synthetic Control of Green Fluorescent Protein. *J. Am. Chem. Soc.* **2009**, *131*, 15988–15989.

300. Hoi, H.; Shaner, N. C.; Davidson, M. W.; Cairo, C. W.; Wang, J.; Campbell, R. E. A Monomeric Photoconvertible Fluorescent Protein for Imaging of Dynamic Protein Localization. *J. Mol. Biol.* **2010**, *401*, 776–791.

301. Sadowski, I.; Ma, J.; Triezenberg, S.; Ptashne, M. GAL4-VP16 is an unusually potent transcriptional activator. *Nature* **1988**, *335*, 563–564.

302. Sunaguchi, M.; Nishi, M.; Mizobe, T.; Kawata, M. Real-time imaging of green fluorescent protein-tagged beta 2-adrenergic receptor distribution in living cells. *Brain Res.* **2003**, *984*, 21–32.

303. Southall, T. D.; Elliott, D. A.; Brand, A. H. The GAL4 System: A Versatile Toolkit for Gene Expression in Drosophila. *Cold Spring Harb. Protoc.* **2008**, *2008*, pdb.top49-pdb.top49.

304. Picard, D. Posttranslational regulation of proteins by fusions to steroid-binding domains. *Methods Enzymol.* **2000**, *327*, 385–401.

305. Scherrer, L. C.; Picard, D.; Massa, E.; Harmon, J. M.; Simons, S. S.; Yamamoto, K. R.; Pratt, W. B. Evidence that the hormone binding domain of steroid receptors confers hormonal control on chimeric proteins by determining their hormone-regulated binding to heat-shock protein 90. *Biochemistry (Mosc.)* **1993**, *32*, 5381–5386.

306. Matsuda, T.; Cepko, C. L. Controlled expression of transgenes introduced by *in vivo* electroporation. *Proc. Natl. Acad. Sci. U. S. A.* **2007**, *104*, 1027–1032.

307. Dempsey, W. P.; Georgieva, L.; Helbling, P. M.; Sonay, A. Y.; Truong, T. V.; Haffner, M.; Pantazis, P. *In vivo* single-cell labeling by confined primed conversion. *Nat. Methods* **2015**, *12*, 645–648.

308. Mohr, M. A.; Pantazis, P. Single neuron morphology *in vivo* with confined primed conversion. In *Methods in Cell Biology*; Elsevier, 2016; Vol. 133, pp. 125–138.

309. Mohr, M. A.; Argast, P.; Pantazis, P. Labeling cellular structures *in vivo* using confined primed conversion of photoconvertible fluorescent proteins. *Nat. Protoc.* **2016**, *11*, 2419–2431.

310. Kugler, J.; Schmelz, S.; Gentzsch, J.; Haid, S.; Pollmann, E.; van den Heuvel, J.; Franke, R.; Pietschmann, T.; Heinz, D. W.; Collins, J. High Affinity Peptide Inhibitors of the Hepatitis C Virus NS3-4A Protease Refractory to Common Resistant Mutants. *J. Biol. Chem.* **2012**, *287*, 39224–39232.

311. Kim, J. H.; Lee, S.-R.; Li, L.-H.; Park, H.-J.; Park, J.-H.; Lee, K. Y.; Kim, M.-K.; Shin, B. A.; Choi, S.-Y. High Cleavage Efficiency of a 2A Peptide Derived from Porcine Teschovirus-1 in Human Cell Lines, Zebrafish and Mice. *PLoS ONE* **2011**, *6*, e18556.

312. Sandilos, J. K.; Chiu, Y.-H.; Chekeni, F. B.; Armstrong, A. J.; Walk, S. F.; Ravichandran, K. S.; Bayliss, D. A. Pannexin 1, an ATP Release Channel, Is Activated by Caspase Cleavage of Its Pore-associated C-terminal Autoinhibitory Region. *J. Biol. Chem.* **2012**, *287*, 11303–11311.

313. Tachibana-Konwalski, K.; Godwin, J.; van der Weyden, L.; Champion, L.; Kudo, N. R.; Adams, D. J.; Nasmyth, K. Rec8-containing cohesin maintains bivalents without turnover during the growing phase of mouse oocytes. *Genes Dev.* **2010**, *24*, 2505–2516.

314. Gray, D. C.; Mahrus, S.; Wells, J. A. Activation of Specific Apoptotic Caspases with an Engineered Small-Molecule-Activated Protease. *Cell* **2010**, *142*, 637–646.

315. Wehr, M. C.; Laage, R.; Bolz, U.; Fischer, T. M.; Grünewald, S.; Scheek, S.; Bach, A.; Nave, K.-A.; Rossner, M. J. Monitoring regulated protein-protein interactions using split TEV. *Nat. Methods* **2006**, *3*, 985–993.

316. Shapira, A.; Shapira, S.; Gal-Tanamy, M.; Zemel, R.; Tur-Kaspa, R.; Benhar, I. Removal of Hepatitis C Virus-Infected Cells by a Zymogenized Bacterial Toxin. *PLoS ONE* **2012**, *7*, e32320.

317. Penuela, S.; Gehi, R.; Laird, D. W. The biochemistry and function of pannexin channels. *Biochim. Biophys. Acta BBA - Biomembr.* **2013**, *1828*, 15–22.

318. Lohman, A. W.; Isakson, B. E. Differentiating connexin hemichannels and pannexin channels in cellular ATP release. *FEBS Lett.* **2014**, *588*, 1379–1388.

319. Chekeni, F. B.; Elliott, M. R.; Sandilos, J. K.; Walk, S. F.; Kinchen, J. M.; Lazarowski, E. R.; Armstrong, A. J.; Penuela, S.; Laird, D. W.; Salvesen, G. S.; Isakson, B. E.; Bayliss, D. A.; Ravichandran, K. S. Pannexin 1 channels mediate "find-me" signal release and membrane permeability during apoptosis. *Nature* **2010**, *467*, 863–867.

320. Weilinger, N. L.; Lohman, A. W.; Rakai, B. D.; Ma, E. M. M.; Bialecki, J.; Maslieieva, V.; Rilea, T.; Bandet, M. V.; Ikuta, N. T.; Scott, L.; Colicos, M. A.; Teskey, G. C.; Winship, I. R.; Thompson, R. J. Metabotropic NMDA receptor signaling couples Src family kinases to pannexin-1 during excitotoxicity. *Nat. Neurosci.* **2016**, *19*, 432–442.

321. Cheng, Z.; Campbell, R. E. Assessing the Structural Stability of Designed β-Hairpin Peptides in the Cytoplasm of Live Cells. *ChemBioChem* **2006**, *7*, 1147–1150.

322. Henderson, B. R.; Eleftheriou, A. A Comparison of the Activity, Sequence Specificity, and CRM1-Dependence of Different Nuclear Export Signals. *Exp. Cell Res.* **2000**, *256*, 213–224.

323. Kalderon, D.; Roberts, B. L.; Richardson, W. D.; Smith, A. E. A short amino acid sequence able to specify nuclear location. *Cell* **1984**, *39*, 499–509.

324. Hathaway, N. A.; Bell, O.; Hodges, C.; Miller, E. L.; Neel, D. S.; Crabtree, G. R. Dynamics and Memory of Heterochromatin in Living Cells. *Cell* **2012**, *149*, 1447–1460.

325. Potter, C. J.; Tasic, B.; Russler, E. V.; Liang, L.; Luo, L. The Q System: A Repressible Binary System for Transgene Expression, Lineage Tracing, and Mosaic Analysis. *Cell* **2010**, *141*, 536–548.

326. Campeau, E.; Ruhl, V. E.; Rodier, F.; Smith, C. L.; Rahmberg, B. L.; Fuss, J. O.; Campisi, J.; Yaswen, P.; Cooper, P. K.; Kaufman, P. D. A Versatile Viral System for Expression and Depletion of Proteins in Mammalian Cells. *PLoS ONE* **2009**, *4*, e6529.

327. Budhu, A.; Chen, Y.; Kim, J. W.; Forgues, M.; Valerie, K.; Harris, C. C.; Wang, X. W. Induction of a unique gene expression profile in primary human hepatocytes by hepatitis C virus core, NS3 and NS5A proteins. *Carcinogenesis* **2007**, *28*, 1552–1560.

328. Hwang, D.-R.; Lai, H.-Y.; Chang, M.-L.; Hsu, J. T. A.; Yeh, C.-T. Emergence of mutation clusters in the HCV genome during sequential viral passages in Sip-L expressing cells. *J. Virol. Methods* **2005**, *129*, 170–177.

329. Taremi, S. S.; Beyer, B.; Maher, M.; Yao, N.; Prosise, W.; Weber, P. C.; Malcolm, B. A. Construction, expression, and characterization of a novel fully activated recombinant single-chain hepatitis C virus protease. *Protein Sci.* **1998**, *7*, 2143–2149.

330. Urbani, A.; Bianchi, E.; Narjes, F.; Tramontano, A.; De Francesco, R.; Steinkühler, C.; Pessi, A. Substrate specificity of the hepatitis C virus serine protease NS3. *J. Biol. Chem.* **1997**, *272*, 9204–9209.

331. Roberts, P. J.; Mitin, N.; Keller, P. J.; Chenette, E. J.; Madigan, J. P.; Currin, R. O.; Cox, A. D.; Wilson, O.; Kirschmeier, P.; Der, C. J. Rho Family GTPase Modification and Dependence on CAAX Motif-signaled Posttranslational Modification. *J. Biol. Chem.* **2008**, *283*, 25150–25163.

332. Edelstein, A. D.; Tsuchida, M. A.; Amodaj, N.; Pinkard, H.; Vale, R. D.; Stuurman, N. Advanced methods of microscope control using μManager software. *J. Biol. Methods* **2014**, *1*, 10.

333. Shao, Q.; Lindstrom, K.; Shi, R.; Kelly, J.; Schroeder, A.; Juusola, J.; Levine, K. L.; Esseltine, J. L.; Penuela, S.; Jackson, M. F.; Laird, D. W. A Germline Variant in the *PANX1* Gene Has Reduced Channel Function and Is Associated with Multisystem Dysfunction. *J. Biol. Chem.* **2016**, *291*, 12432–12443.

334. Ward, W. W.; Prentice, H. J.; Roth, A. F.; Cody, C. W.; Reeves, S. C. Spectral perturbations of the *Aequorea* green fluorescent protein. *Photochem. Photobiol.* **1982**, *35*, 803–808.

335. Sankaranarayanan, S.; De Angelis, D.; Rothman, J. E.; Ryan, T. A. The Use of pHluorins for Optical Measurements of Presynaptic Activity. *Biophys. J.* **2000**, *79*, 2199–2208.

336. Tsuboi, T.; Rutter, G. A. Multiple Forms of "Kiss-and-Run" Exocytosis Revealed by Evanescent Wave Microscopy. *Curr. Biol.* **2003**, *13*, 563–567.

337. An, S. J.; Grabner, C. P.; Zenisek, D. Real-time visualization of complexin during single exocytic events. *Nat. Neurosci.* **2010**, *13*, 577–583.

338. Balaji, J.; Ryan, T. A. Single-vesicle imaging reveals that synaptic vesicle exocytosis and endocytosis are coupled by a single stochastic mode. *Proc. Natl. Acad. Sci. U. S. A.* **2007**, *104*, 20576–20581.

339. Jullie, D.; Choquet, D.; Perrais, D. Recycling Endosomes Undergo Rapid Closure of a Fusion Pore on Exocytosis in Neuronal Dendrites. *J. Neurosci.* **2014**, *34*, 11106–11118.

340. Merrifield, C. J.; Perrais, D.; Zenisek, D. Coupling between Clathrin-Coated-Pit Invagination, Cortactin Recruitment, and Membrane Scission Observed in Live Cells. *Cell* **2005**, *121*, 593–606.

341. Taylor, M. J.; Perrais, D.; Merrifield, C. J. A High Precision Survey of the Molecular Dynamics of Mammalian Clathrin-Mediated Endocytosis. *PLoS Biol.* **2011**, *9*, e1000604.

342. Yudowski, G. A.; Puthenveedu, M. A.; von Zastrow, M. Distinct modes of regulated receptor insertion to the somatodendritic plasma membrane. *Nat. Neurosci.* **2006**, *9*, 622–627.

343. Tanida, I.; Ueno, T.; Uchiyama, Y. A Super-Ecliptic, pHluorin-mKate2, Tandem Fluorescent Protein-Tagged Human LC3 for the Monitoring of Mammalian Autophagy. *PLoS ONE* **2014**, *9*, e110600.

344. Johnson, D. E.; Ai, H. -w.; Wong, P.; Young, J. D.; Campbell, R. E.; Casey, J. R. Red Fluorescent Protein pH Biosensor to Detect Concentrative Nucleoside Transport. *J. Biol. Chem.* **2009**, *284*, 20499–20511.

345. Tantama, M.; Hung, Y. P.; Yellen, G. Imaging Intracellular pH in Live Cells with a Genetically Encoded Red Fluorescent Protein Sensor. *J. Am. Chem. Soc.* **2011**, *133*, 10034–10037.

346. Shen, Y.; Rosendale, M.; Campbell, R. E.; Perrais, D. pHuji, a pH-sensitive red fluorescent protein for imaging of exo- and endocytosis. *J. Cell Biol.* **2014**, *207*, 419–432.

347. Li, Y.; Tsien, R. W. pHTomato, a red, genetically encoded indicator that enables multiplex interrogation of synaptic activity. *Nat. Neurosci.* **2012**, *15*, 1047–1053.

348. Chu, J.; Haynes, R. D.; Corbel, S. Y.; Li, P.; González-González, E.; Burg, J. S.; Ataie, N. J.; Lam, A. J.; Cranfill, P. J.; Baird, M. A.; Davidson, M. W.; Ng, H.-L.; Garcia, K. C.; Contag, C. H.; Shen, K.; Blau, H. M.; Lin, M. Z. Non-invasive intravital imaging of cellular differentiation with a bright red-excitable fluorescent protein. *Nat. Methods* **2014**, *11*, 572–578.

349. Filonov, G. S.; Krumholz, A.; Xia, J.; Yao, J.; Wang, L. V.; Verkhusha, V. V. Deep-Tissue Photoacoustic Tomography of a Genetically Encoded Near-Infrared Fluorescent Probe. *Angew. Chem. Int. Ed.* **2012**, *51*, 1448–1451.

350. Krumholz, A.; Shcherbakova, D. M.; Xia, J.; Wang, L. V.; Verkhusha, V. V. Multicontrast photoacoustic *in vivo* imaging using near-infrared fluorescent proteins. *Sci. Rep.* **2015**, *4*.

351. Yao, J.; Kaberniuk, A. A.; Li, L.; Shcherbakova, D. M.; Zhang, R.; Wang, L.; Li, G.; Verkhusha, V. V.; Wang, L. V. Multiscale photoacoustic tomography using reversibly switchable bacterial phytochrome as a near-infrared photochromic probe. *Nat. Methods* **2015**.

352. Wang, L. V.; Hu, S. Photoacoustic Tomography: *In Vivo* Imaging from Organelles to Organs. *Science* **2012**, *335*, 1458–1462.

353. Filonov, G. S.; Verkhusha, V. V. A Near-Infrared BiFC Reporter for *In Vivo* Imaging of Protein-Protein Interactions. *Chem. Biol.* **2013**, *20*, 1078–1086.

354. Tchekanda, E.; Sivanesan, D.; Michnick, S. W. An infrared reporter to detect spatiotemporal dynamics of protein-protein interactions. *Nat. Methods* **2014**, *11*, 641–644.

355. Yu, D.; Gustafson, W. C.; Han, C.; Lafaye, C.; Noirclerc-Savoye, M.; Ge, W.-P.; Thayer, D. A.; Huang, H.; Kornberg, T. B.; Royant, A.; Jan, L. Y.; Jan, Y. N.; Weiss, W. A.; Shu, X. An improved monomeric infrared fluorescent protein for neuronal and tumour brain imaging. *Nat. Commun.* **2014**, *5*.

356. Shcherbakova, D. M.; Verkhusha, V. V. Near-infrared fluorescent proteins for multicolor *in vivo* imaging. *Nat. Methods* **2013**, *10*, 751–754.

357. Filonov, G. S.; Piatkevich, K. D.; Ting, L.-M.; Zhang, J.; Kim, K.; Verkhusha, V. V. Bright and stable near-infrared fluorescent protein for *in vivo* imaging. *Nat. Biotechnol.* **2011**, *29*, 757–761.

358. Guo, Y.; Zhou, I. Y.; Chan, S.-T.; Wang, Y.; Mandeville, E. T.; Igarashi, T.; Lo, E. H.; Ji, X.; Sun, P. Z. pH-sensitive MRI demarcates graded tissue acidification during acute stroke — pH specificity enhancement with magnetization transfer and relaxation-normalized amide proton transfer (APT) MRI. *NeuroImage* **2016**, *141*, 242–249.

359. Estrella, V.; Chen, T.; Lloyd, M.; Wojtkowiak, J.; Cornnell, H. H.; Ibrahim-Hashim, A.; Bailey, K.; Balagurunathan, Y.; Rothberg, J. M.; Sloane, B. F.; Johnson, J.; Gatenby, R. A.; Gillies, R. J. Acidity Generated by the Tumor Microenvironment Drives Local Invasion. *Cancer Res.* **2013**, *73*, 1524–1535.

360. von Stetten, D.; Seibeck, S.; Michael, N.; Scheerer, P.; Mroginski, M. A.; Murgida, D. H.; Krauss, N.; Heyn, M. P.; Hildebrandt, P.; Borucki, B.; Lamparter, T. Highly Conserved Residues Asp-197 and His-250 in Agp1

Phytochrome Control the Proton Affinity of the Chromophore and Pfr Formation. *J. Biol. Chem.* **2007**, *282*, 2116–2123.

361. Zienicke, B.; Molina, I.; Glenz, R.; Singer, P.; Ehmer, D.; Escobar, F. V.; Hildebrandt, P.; Diller, R.; Lamparter, T. Unusual Spectral Properties of Bacteriophytochrome Agp2 Result from a Deprotonation of the Chromophore in the Red-absorbing Form Pr. *J. Biol. Chem.* **2013**, *288*, 31738–31751.

362. Bhattacharya, S.; Auldridge, M. E.; Lehtivuori, H.; Ihalainen, J. A.; Forest, K. T. Origins of Fluorescence in Evolved Bacteriophytochromes. *J. Biol. Chem.* **2014**, *289*, 32144–32152.

363. Wilks, J. C.; Slonczewski, J. L. pH of the Cytoplasm and Periplasm of Escherichia coli: Rapid Measurement by Green Fluorescent Protein Fluorimetry. *J. Bacteriol.* **2007**, *189*, 5601–5607.

364. Rodriguez, E. A.; Tran, G. N.; Gross, L. A.; Crisp, J. L.; Shu, X.; Lin, J. Y.; Tsien, R. Y. A far-red fluorescent protein evolved from a cyanobacterial phycobiliprotein. *Nat. Methods* **2016**, *13*, 763–769.

365. Forns, X.; Emerson, S. U.; Tobin, G. J.; Mushahwar, I. K.; Purcell, R. H.; Bukh, J. DNA immunization of mice and macaques with plasmids encoding hepatitis C virus envelope E2 protein expressed intracellularly and on the cell surface. *Vaccine* **1999**, *17*, 1992–2002.

366. Carmody, W. R. Easily prepared wide range buffer series. *J. Chem. Educ.* **1961**, *38*, 559.

367. Wäldchen, S.; Lehmann, J.; Klein, T.; van de Linde, S.; Sauer, M. Light-induced cell damage in live-cell super-resolution microscopy. *Sci. Rep.* **2015**, *5*, 15348.

368. Wang, S.; Moffitt, J. R.; Dempsey, G. T.; Xie, X. S.; Zhuang, X. Characterization and development of photoactivatable fluorescent proteins for single-molecule-based superresolution imaging. *Proc. Natl. Acad. Sci. U. S. A.* **2014**, *111*, 8452–8457.

369. Zhang, M.; Chang, H.; Zhang, Y.; Yu, J.; Wu, L.; Ji, W.; Chen, J.; Liu, B.; Lu, J.; Liu, Y.; Zhang, J.; Xu, P.; Xu, T. Rational design of true monomeric and bright photoactivatable fluorescent proteins. *Nat. Methods* **2012**, *9*, 727–729.

370. Christie, J. M.; Corchnoy, S. B.; Swartz, T. E.; Hokenson, M.; Han, I.-S.; Briggs, W. R.; Bogomolni, R. A. Steric Interactions Stabilize the Signaling State of the LOV2 Domain of Phototropin 1 †. *Biochemistry (Mosc.)* **2007**, *46*, 9310–9319.

371. Zoltowski, B. D.; Vaccaro, B.; Crane, B. R. Mechanism-based tuning of a LOV domain photoreceptor. *Nat. Chem. Biol.* **2009**, *5*, 827–834.

372. Kawano, F.; Aono, Y.; Suzuki, H.; Sato, M. Fluorescence Imaging-Based High-Throughput Screening of Fast- and Slow-Cycling LOV Proteins. *PLoS ONE* **2013**, *8*, e82693.

373. Zoltowski, B. D.; Schwerdtfeger, C.; Widom, J.; Loros, J. J.; Bilwes, A. M.; Dunlap, J. C.; Crane, B. R. Conformational Switching in the Fungal Light Sensor Vivid. *Science* **2007**, *316*, 1054–1057.

374. Heijde, M.; Ulm, R. Reversion of the Arabidopsis UV-B photoreceptor UVR8 to the homodimeric ground state. *Proc. Natl. Acad. Sci. U. S. A.* **2013**, *110*, 1113–1118.

375. Ni, M.; Tepperman, J. M.; Quail, P. H. Binding of phytochrome B to its nuclear signalling partner PIF3 is reversibly induced by light. *Nature* **1999**, *400*, 781–784.

376. Zhang, W.; Lohman, A. W.; Zhuravlova, Y.; Lu, X.; Wiens, M. D.; Hoi, H.; Yaganoglu, S.; Mohr, M. A.; Kitova, E. N.; Klassen, J. S.; Pantazis, P.; Thompson, R. J.; Campbell, R. E. Optogenetic control with a photocleavable protein, PhoCl. *Nat. Methods* **2017**, *14*, 391–394.

377. To, T.-L.; Zhang, Q.; Shu, X. Structure-guided design of a reversible fluorogenic reporter of protein-protein interactions: Design of a Reversible Fluorogenic Reporter of PPIs. *Protein Sci.* **2016**, *25*, 748–753.

378. Kumagai, A.; Ando, R.; Miyatake, H.; Greimel, P.; Kobayashi, T.; Hirabayashi, Y.; Shimogori, T.; Miyawaki, A. A Bilirubin-Inducible Fluorescent Protein from Eel Muscle. *Cell* **2013**, *153*, 1602–1611.

379. Ozawa, T.; Kaihara, A.; Sato, M.; Tachihara, K.; Umezawa, Y. Split Luciferase as an Optical Probe for Detecting Protein−Protein Interactions in Mammalian Cells Based on Protein Splicing. *Anal. Chem.* **2001**, *73*, 2516–2521.

380. Paulmurugan, R.; Gambhir, S. S. Monitoring Protein−Protein Interactions Using Split Synthetic Renilla Luciferase Protein-Fragment-Assisted Complementation. *Anal. Chem.* **2003**, *75*, 1584–1589.

381. Remy, I.; Michnick, S. W. A highly sensitive protein-protein interaction assay based on Gaussia luciferase. *Nat. Methods* **2006**, *3*, 977–979.

382. Zhao, J.; Nelson, T. J.; Vu, Q.; Truong, T.; Stains, C. I. Self-Assembling NanoLuc Luciferase Fragments as Probes for Protein Aggregation in Living Cells. *ACS Chem. Biol.* **2016**, *11*, 132–138.

383. Huang, W.; Zhang, Z.; Palzkill, T. Design of Potent β-Lactamase Inhibitors by Phage Display of β-Lactamase Inhibitory Protein. *J. Biol. Chem.* **2000**, *275*, 14964–14968.

384. Rudgers, G. W.; Huang, W.; Palzkill, T. Binding Properties of a Peptide Derived from beta-Lactamase Inhibitory Protein. *Antimicrob. Agents Chemother.* **2001**, *45*, 3279–3286.

385. Huang, W.; Beharry, Z.; Zhang, Z.; Palzkill, T. A broad-spectrum peptide inhibitor of beta-lactamase identified using phage display and peptide arrays. *Protein Eng.* **2003**, *16*, 853–860.

386. O'Callaghan, C. H.; Morris, A.; Kirby, S. M.; Shingler, A. H. Novel method for detection of beta-lactamases by using a chromogenic cephalosporin substrate. *Antimicrob. Agents Chemother.* **1972**, *1*, 283–288.

387. Gao, W.; Xing, B.; Tsien, R. Y.; Rao, J. Novel fluorogenic substrates for imaging beta-lactamase gene expression. *J. Am. Chem. Soc.* **2003**, *125*, 11146–11147.